Design and Dynamic Modeling of an Unmanned Underwater Vehicle for Submerged Surface Inspection Exploiting Hydrodynamic Ground Effect

by

Sampriti Bhattacharyya

B.S., St. Thomas College of Engineering (2009)
S.M., The Ohio State University (2012)

Submitted to the Department of Mechanical Engineering
in partial fulfillment of the requirements for the degree of

Doctor of Philosophy

at the

MASSACHUSETTS INSTITUTE OF TECHNOLOGY

June 2017

Signature redacted

Author .....
Department of Mechanical Engineering
Signature redacted May 12, 2017

Certified by .....
Harry Asada
Ford Professor of Engineering
Thesis Supervisor

Accepted by ..... Signature redacted
Rohan Abeyaratne
Chairman, Department Committee on Graduate Theses

Design and Dynamic Modeling of an Unmanned Underwater Vehicle for Submerged Surface Inspection Exploiting Hydrodynamic Ground Effect

by

Sampriti Bhattacharyya

Submitted to the Department of Mechanical Engineering
on May 12, 2017, in partial fulfillment of the
requirements for the degree of
Doctor of Philosophy

Abstract

ANTICIPATED growth of sub-sea technologies for security, infrastructure inspection, and exploration, motivates a deeper understanding of underwater navigation in proximity to a submerged target surface. Common examples range from water tanks in nuclear reactors, submerged oil rig infrastructure, to ship hulls with hidden compartments and threats. We propose EVIE (Ellipsoidal Vehicle for Inspection and Exploration): a water jet propelled, football sized ellipsoidal Unmanned Underwater Vehicle (UUV) with a flattened base to house necessary sensors needed for surface inspections. The UUV is designed – both in terms of its shape and propulsion – for gliding on submerged surfaces for volumetric inspection, in addition to motion in free stream motion for visual inspections. This thesis research explores the ground effect hydrodynamics due to the motion of a body near a surface. We demonstrate the formation of a thin fluid bed layer between the surfaces which enables smooth motion even on rough surfaces. The proposed robot eliminates the need for wheels or suction. Use of ground effect fluid dynamics is common in aerial and land vehicles but is almost unexplored for underwater applications. We focus exploiting this phenomenon in real world applications, developing a prototype model to maintain precise distances with reduced actuator control. We explore both parasitic (induced by lateral motion) and explicitly induced (adding a impinging bottom jet) hydrodynamic effects.

We find the force is not only non linear, it is not monotonic and has multiple equilibria. As

the body approaches the surface it first experiences repulsion (enhanced thrust) due to an upwash effect – similar to vertical take off and landing (VTOL) vehicles which can hover at reduced thrust. This transitions to a suction force at small distances from a Venturi effect. At still smaller distances there is again a repulsion due to choking flow between the body and the surface.

Given the complexity of the force, and considering the hydrodynamic drag is non linear as well, traditional linearization fails to capture the system behavior and is at best constrained to a small region around the equilibrium. Instead, we use a higher dimensional, data driven approach for modeling. The underlying hypothesis is that dynamical systems behave linearly when recast in a suitable higher dimensional space. State variables are augmented by adding auxiliary variables that sufficiently inform the nonlinear dynamics of the system. We demonstrate a novel and a powerful method of individual estimation of each of the state dependent non linearities by integrating a state estimator into the augmented system. The estimator only uses measured, original states to estimate the non linear forces. The method is extremely robust: even though the approximated state transition model has significant inaccuracies, we prove guaranteed convergence of the unobserved states.

This doctoral thesis encompasses three unique contribution: design and development of a prototype micro UUV platform for testing surface inspection methods; invention and application of a unique underwater phenomenon to the UUV; and establishing a novel mathematical approach for robust estimation of complex non linear elements using a linearized, high dimensional data driven model. The research presented opens a whole new door of opportunities and provides a new perspective for the design of next generation subsea vehicles and technology.

Thesis Supervisor: Harry Asada, PhD
Title: Ford Professor of Engineering, Department of Mechanical Engineering, MIT

Acknowledgments

The exact time right now is 3 AM, π day 2017 as I start writing this acknowledgement section. I just wrapped up my first review of what a couple months ago seemed like an impossible mission. As I am almost at the finish line of a milestone of my life, a dream which a decade ago could have only happened in a parallel universe, it is pretty amusing to think that there is a fairly long list of people and strings incoherent incidents that I must and should acknowledge, that took a merely curious, ordinary college girl somewhere in India to completing this doctoral thesis - on robots- at MIT.

First acknowledgement is to MIT for granting that admission. For a bum like me, home is where I find my passion. And this place is what I have called home for last four and half years. This place has inspired me, challenged me, supported me in the roughest times and found me friends that I will keep for life. Every time I take a quiet walk around the campus at random hours of night, I stare at the names of those who changed the world – that transistor, that computer I carry, that internet we take for granted. I've loved this place everyday, even the days I didn't want to be here; it has motivated me to not be scared of solving big complex problems, and instilling faith that we all can learn what we need to, if we choose to. The late evenings when I would work alone in my back bay apartment, juggling my life between a startup and a PhD and all the other unwanted hassles life throws at you, sometimes every bone of my body wanted to give up. Nights like those I would run the Harvard Bridge while looking ahead at the lit up dome of MIT. I would think of my life back in India. And standing at the Killian court, I would remember the 18 year old me who was told the best she could be was perhaps a housewife or work on a trivial job. I wasn't smart enough for math and I wasn't good enough for way too many things. I have come to realize we humans are more powerful and capable than we realize, and I knew there's always a fight left before you give up. The doctoral thesis was one of the most challenging things I've ever worked on and I hope that this is only the start. Thank you MIT for taking a chance in me, one who didn't fit the norm – and I won't let you down.

Next, my advisor, Professor Harry Asada. I admire your patience with me over these four years! I might have had many fits, and we may be different in our work approach, but as I am wrapping up the thesis, I would truly like to thank you for challenging me and putting me through the rigor. I had my doubts when I started out as the only girl in that basement lab with 15 guys, never having worked in mechanical engineering and wondering if I will ever make it through! Thank you for this opportunity and letting me work in such an amazing lab with all the tools I never had access before, and on a research that I caught my imagination enough to bet my life goals on it.

I would like to thank my committee members Professor Triantafyllou and Professor Del Vecchio who have taken time out from their schedule to review my work and provide valuable feedback during our research meetings. I would also like to thank Professor Triantafyllou's students, especially Jacob Izraelevitz for helping me have access to the tow tank for several months of experiments.

I would also like to thank EPRI and NSF for funding this research and for my graduate stipend.

Now, I'd like to acknowledge those who helped me one way or other, reach the finish line.

To my labmates, thank you guys for the support and putting up with my chaos! Especially Federico Parietti – thank you for being an amazing friend, support and inspiration from those rough all nighters to our startup struggles. To Faye, Michaelle, Alex – for the endless PCA, PLSR discussions! Lie algebra is certainly next on my list, haha. Yvette, thank you for the amazing food and for always being so helpful.

My students who I mentor and my UROPs. Particularly, Arlette, Danielle, Sammy, Isabella, Kyubin, Sneha, Priya – it has been such a rewarding experience to share my knowledge, and I hope you all know there is nothing that you are not capable of. Sammy, Arlette and Danielle, I am so incredibly proud of you three, and I hope you will always continue to challenge yourselves to put your skills into creating something amazing. Very few things in life makes me as happy as to see all you guys succeed in what you are passionate about.

My mentors, advisors – both in research (at Fermilab, NASA, OSU) and in my entrepreneurial journey – thank you for having the guidance. Ellie, Emma, Mia and Rajni, Linda – thank you for being the incredible women I look up to and being there for advice and love. To my friends in US and elsewhere, to the "original group" – you know who you are! And Faith Njokou, my soul sister; all of you added a lot of value to my life.

To President Rafael Reif. We have never met in person, but your thoughtful emails to the community have given me hope in the dark times. As an foreigner myself, I see you as a amazing role role model. Thank you for making MIT so incredible and a place for people with such diversity.

To family back in India. I am sorry, I haven't been there for you much, but I will try to be better. I always wish you happiness, and thank you for the years of support to making sure I got through college. Thank you for not stopping the rebel in me.

To Mateusz M of You Tube Motivation videos and the Piano Guys – thank you for helping me write the 300 pages. To the 24 Hours Star Market downstairs (Prudential Tower) for ensuring easy food access!

A big acknowledgement to the naysayers, the road blocks and the struggles of life. You are who you are because of them, and not despite of them.

I am thankful to my MIT PhD educated American ex boyfriend who taught me we (both men and women) have a long way to go when it comes to gender equality even in this country (this is 2017!). In my journey with you, I was told "Ambitious women end up lonely- why would you ever want that", that I was "obsessed with success" and "too independent". I was told that I was not emotionally strong enough, organized enough, meticulous enough, disciplined enough, patient enough or perfect enough to live my very own dreams. I didn't fit in the norm and I broke rules. Last two years was very rough, and I lost a lot of time and health going through this turmoil, lost my self confidence even though I was winning awards and recognitions. There were moments I thought of giving up. When I hit a roadblock, I was terrified all the criticisms are true. But I didn't give up- cause among many things, I also didn't want your opinion to define who I am and can be in life and how things should be done in order to succeed. There are women who in this institution broke the norm starting many decades ago and paved the path for women like us today. I hope I can do my bit in that regard- mostly in the part letting any girl reading this in future know that your gender role shouldn't define what you can be passionate about, and who you can be and should

be in life. In the words of Vince Lombardi, life's battles don't always go to the stronger or faster person. But sooner or later, the one who wins is the one who thinks he/she can. Don't try to fit in. You won't be happy. Create your own space, if you have to.

Now last but not the least, few very important ones to end this with ...

Jay... thanking is a word too small. You had faith in me, when the world didn't and when I didn't. My thank to you should only be in action, i.e. through what I will build and create.

Dr. Rheinila Fernandes. For over last 4 years, you've been one of my biggest cheerleaders. Thank you for always finding the best in me, seeing me through the toughest times and keeping me in good health.You taught me again and again to forgive myself when I had faltered and had been too hard on myself. I couldn't have done it without you. I hope all the students at MIT know of the wonderful resource we have on campus, the people we can turn to. You are incredible, and these few lines are not enough to express my gratitude.

My dear Jane. I wish I could have given more time to us through these crazy years. But, I hope you always know you're family to me, in this country where we once started our journey together. And when you need me, I will be there.

My best friend Natasha Wright. You are one of the best things that have ever happened to me, you are an incredible human being and I am extremely fortunate to have you in my life. Thanks to MIT for helping me find you! The unconditional love and support, from the best to the worst times that you have shared with me – the things I have achieved in my time here, you are an important part of everything. You inspire me with your kindness, your constant effort to help others beyond yourselves, and your ever positive attitude. When I see so many things that are not so right in the world, it are people like you who make me realize there is a lot of good things that are worth believing. You make the world a much better place.

Tony Stark. Ironman. Coming to America eight years ago and hanging out in a national lab with Marvel Comics and movies to watch- I didn't realize I'd find my role model in a fiction book. I came to MIT to build the nuclear reactor, and ended up building crazy cool robots.

To NASA/Mars mission on Discovery Channel - that was the start and life was never the same again! To hardware related PhD, thank you for teaching me that everything in life takes 3 times more time and money than what we plan for. That perseverance skill just got a huge boost after my life with you. Now lets hope I can somehow gather the patience to sit down for the second round revision of this thesis.

Last but not the least, final acknowledgement is to life. Lot of things happened that never made sense. Some even seemed unfair. And yet, the dots connect when we look back. I am not stopping, and I will go for what's mine in this universe. With no regrets.

Contents

List of Figures

List of Tables

Chapter 1

Introduction

1.1 Inspection of Submerged Structures

Anticipated growth in subsea operations and water based infrastructures[1] demands a thorough understanding of operations in such environments, in particular for remote inspection and maintenance. At present inspection mostly relies on human divers or tethered equipments, including Remotely Operated Vehicles (ROVs)[2],[3]. Considerable work is being done to develop autonomous underwater vehicles (AUVs) for subsea inspections[4] and mostly to minimize human involvement in these tasks. However, as a literature search reveals, most of these robots are large, expensive, often tethered, and made for operation in unobstructed environment such as in the free ocean. There is a need for inspection of cluttered or enclosed environment. Examples include: boiling water reactor (BWR) of nuclear power plants, a cluttered environment with strict inspection protocols and schedules; ship propellors, which need to be viewed from many angles; and inland aquaculture farms, where large or tethered equipment disrupt the operation. In many cases the currently standard visual inspection is insufficient, and more sophisticated methods are required to reveal internal defects [5]. For example, internal hairline cracks on weld seams of a BWR tank [6] in a nuclear power plant facility can lead to radiation leakages. Ship hull inspection

[7] is another task which requires more than just visual inspection. For port security, a combination of methods for inspecting ship hulls using visual, sonar or on contact scanning equipments (ultrasound, electromagnetic etc) are areas of immense interest to prevent smuggling of contrabands including weapons (biological, chemical, or nuclear)[8], [9] in hidden cavities along the body or around the propeller [10]. For instance the US Navy's anti-terrorism Marine mammal program [11] deployed dolphins for stealth, with biological ultrasound, to find hidden threats in ship hulls or mines. But such a program is not easily scalable across all the nation's harbors and sea ports.

Cavities, as well as internal cracks and other defects, can be detected with a variety of high fidelity Non Destructive Testing (NDT) techniques: ultrasonic testing (UT)[12], eddy current testing (EDT)[13], and laser based imaging [14]. UT is commonly used by placing the sensor in direct contact with the target surface for higher resolution and power efficiency. But deployment for usage of these on submerged infrastructure involve expensive AUVs or bulky tethered ROVs or tethered sensors which can get snagged, are cost prohibitive, and non-optimal for a complex environment. Therefore new areas of innovation in cost effective and scalable technologies for underwater infrastructure monitoring, maintenance and security is gaining momentum.

1.2 Challenges and Functional Requirements

Having provided many instances of submerged infrastructure inspection, we narrow down to some the challenges common to many of them. The work we present is a continuation of research started at the d'Arbeloff Robotics Lab, Department of Mechanical Engineering at MIT [15]. Our focus is to develop inspection robots for cluttered environment, with a BWR being our specific test case.

Key requirements are:

1. Maneuver in cluttered, complex environments
2. Robust to collisions
3. Access areas – nozzles, weld seams, or narrow channels – that are unreachable by towed sensors or tethered ROVs
4. High fidelity subsurface internal structure inspection in addition to visual, implying the ability to move in close proximity to a submerged surface
5. Overcome surface roughness and maintain controlled distance for steady mapping of target areas
6. Quick and efficient method since inspection downtime is expensive

The last requirement calls for an automated or robotic solution with minimal human interference.

A big challenge of on-contact scan of a submerged surface is that, in most cases, the surface is rough and motion on the surface is impeded by friction. This can by addressed by maintaining a small, controlled fluid gap. For UT inspection, efficient signal transfer is achieved by placing the sensor at an odd multiple of quarter wavelength, where reflection from the surface adds in phase at the transducer [16]. However, the thickness of this fluid layer is crucial. Figure (1-1) illustrates the resonance for a non-contact sensor. For a 300KHz UT transducer, wavelength 4mm in water ($c_w = 1500\text{m/s}$), the transducer needs to stay at $n \times 1$ mm from the surface, where n is an odd integer. Shifting the sensor from quarter to half wavelength cancels the pressure building up process, leading to weak subsurface transmission (Figure 1-1b). This affect motivated investigating an inspection

vehicle that can glide across a surface using a intermediate fluid buffer to overcome the roughness. We explored how to transition from a multi-DOF, free stream robot to one that can also scan a surface maintaining a steady and precisely controlled gap. An obvious solution is a tight feedback loop to regulate the gap. However, such a brute force method requires fast, powerful actuators. This may not be feasible; at best it is a power-hungry solution. Therefore we explore an alternative approach that exploits natural hydrodynamic effects of the fluid flow between the vehicle and the inspection surface, i.e. we exploit the so-called "ground effects" to create a self stabilization mechanism. A thin fluid film between solid surfaces – lubrication – is widely studied in tribology to facilitate smooth motion[17]. However, a deeper understanding is necessary if the goal is to not just smooth the motion but maintain stable thickness fluid layer at all times. In the subsequent chapters of the thesis we will explore the ground effect phenomenon in the context of underwater surfaces [18] .

1.3 Literature Review

Different type of robots are being used for underwater structure inspection[19]. At present submerged surface inspection robots are large and complex, mostly tethered, and use visual inspection methods. For volumetric inspections, similarly complex tethered robots with various combinations of wheels, magnets, and suction are used [20] [21]. The control effort required in such configurations is high, and lack of autonomy makes the process tedious. Most are tethered and have propellers or other appendages which can lead to snagging in a cluttered environment. Other robots involved in ship hull [22]or weld seam inspection or maintenance are usually wheeled crawlers, often using magnets to ensure contact. Based on the challenges of the application and the functional requirements a novel design of a underwater robot – the Omni Submersible [15] – was developed at d'Arbeloff

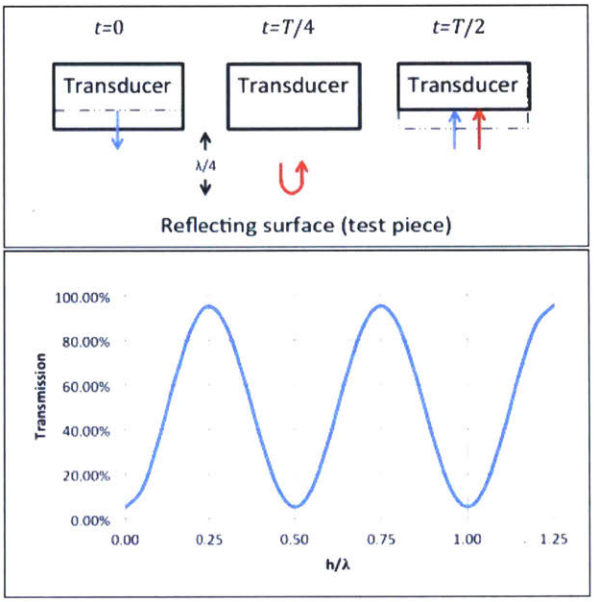

Figure 1-1: Top: Schematic illustration coherent wave behavior at quarter wave gap. Bottom: Transmission efficiency vs distance assuming 90% reflection (10% transmission) at the test surface, and 100% re-absorption at the transducer when placed at quarter wavelength distance

Lab, MIT. It is completely smooth, spheroidal in shape, and jet propelled via multiple exit ports for multi DOF motion, high maneuverability, and robustness to collisions. However, for thorough volumetric inspection, in particular for internal cracks and damages, we need a design that is appropriate for motion on, or at very close proximity to submerged target surfaces. The dynamical and quantitative modeling involved for such a system is quite complex. Motion near submerged surface gives rise to non linear hydrodynamic forces which can be either stabilizing or destabilizing. Very little work has been done in this regard. Particularly hydrodynamic ground effect force [18] which is in some respect similar to aerodynamic ground effect utilized by race cars, can be exploited for near surface motion benefits. Though a fair amount of work has been done in land [23] and little literature is available for underwater effects except that for modeling certain fishes [24] [26] focussing on oscillatory motion of the non rigid bodies.

1.4 Novel Invention: A Micro UUV and Associated Dynamical Modeling for Utilizing Hydrodynamic Ground Effect

To develop efficient surface scanning robots, a thorough understanding of motion in close proximity to submerged surfaces in necessary. This would enable us to get insights to the unique surface effects and hydrodynamic properties that can be taken into consideration for a goal oriented design.

To address high fidelity sub surface imaging, we developed EVIE (Ellipsoidal Vehicle for Inspection and Exploration)[27] : a spheroidal, multiple jet robot like the Omni Submersibles, but with a flat bottom to enable gliding on surfaces. Figure (1-2) shows Omni(right) and EVIE (right). To allow extra payload capacity for NDT sensors such as an UT array, EVIE is larger than it's predecessor, about the size of a football. Jet configuration has been

modified to optimize multi-DOF motion. A bottom outlet has been added to allow forming a fluid bed layer for smooth gliding on rough surfaces. To isolate and study the properties of the fluid bed, our research prototype focussed on movement on a horizontal surfaces in a turbulence free environment. The system exploits hydrodynamic ground effect to actively or passively maintain a stable equilibrium in it's distance from the ground. . Longitudinal motion along the surfaces induces natural hydrodynamic surface effects that causes the body to have a fluid layer below it. When pushed upward it experiences a strong downward (suction) force, referred to as the Venturi effect, which brings it back to the equilibrium. When it is pushed downwards it experiences an upward (repulsive) force, again pushing it back to the equilibrium. The equilibrium thickness of the fluid bed layer caused by longitudinal motion depends on the design parameters as well as velocity of motion. However for practical applications we want direct control on the size of the fluid bed layer. The bottom, center jet outlet provides an active method of controlling the fluid bed. The interaction of the bottom jet with the submerged ground surface demonstrated a stronger suction force (Venturi) as well as a positive force or additional thrust at larger distance (upwash) – an effect also observed in vertical take off and landing (VTOL) vehicles. This jet induced additional thrust force can be used for reduced power motions over submerged surfaces, including sea floors. Motion in proximity of submerged surfaces, is severely under explored. The use of active or induced ground effect hydrodynamics in underwater vehicles in this way has never been done previously and opens up a whole new area of research and innovation for the next generation of subsea technologies.

The hydrodynamic forces in the vicinity of a surface are highly nonlinear, with multiple extrema. In order to exploit this phenomenon we have to integrate it with the system's dynamical model. For system analysis and control purposes linear state space models are usually preferred. However, traditional linearization fails to capture most of the system's

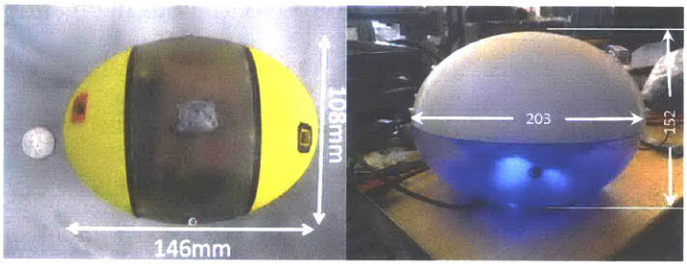

Figure 1-2: Left: Omni Submersible [15] Right: EVIE

non linear behavior and is localized to a small region around the equilibrium. So, we propose an alternative method of modeling: we establish a mathematical basis for data driven estimation of multiple state dependent nonlinear elements. The starting point is the augmentation the non linear elements as additional or 'auxiliary states' to convert the problem to a linear model in a higher dimensional space. A large sample of data is collected covering the anticipated range of operation of the robot. We use Principal Component Analysis (PCA) [28] to form a linearized model in the higher dimensional space. We then implement a state observer to estimate the auxiliary variables (i.e. the non linear elements) and compensate for them using a simple controller. We also analyze the stability and robustness of the data driven model which has the potential to be extended to other complex non linear systems. Among the advantages of this approach is that an analytic description of the system dynamics is not required: the model can be built exclusively from the collected data, whether CFD simulation or real experimental data.

1.5 Key Contributions

The research described in this thesis has three unique areas of contribution:

1. *Concept Vehicle Design.* An spheroidal underwater surface scanning robot was developed with a flat bottom that uses hydrodynamic ground effect for motion on

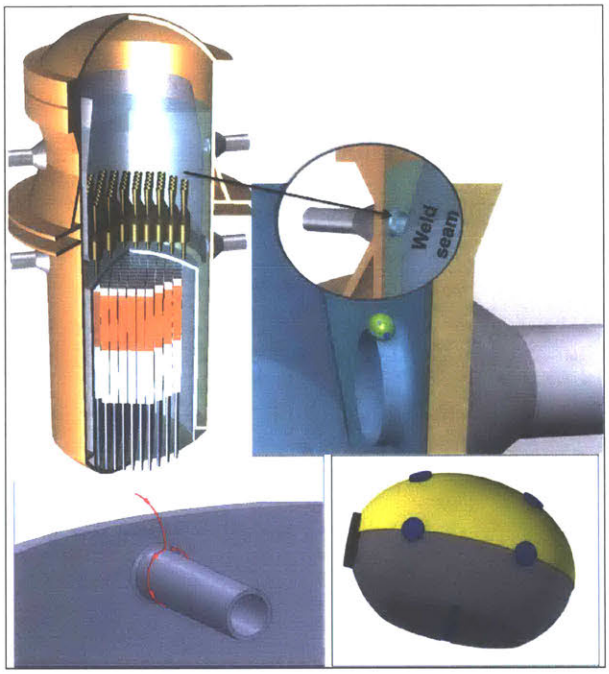

Figure 1-3: A picture demonstrating a concept case of weld seam inspection of a BWR tank with a micro UUV moving on the submerged surface

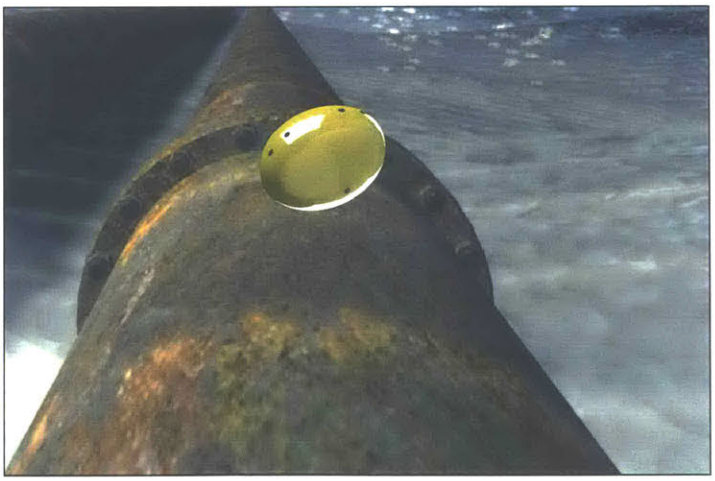

Figure 1-4: Subsea pipeline inspection by a micro UUV

submerged surfaces.

2. *Demonstration of Underwater Ground Effect Hydrodynamics* Demonstrated the occurrence and application of natural (from lateral motion) and jet induced hydrodynamic ground effect. Validated via computational fluid dynamics (CFD) simulation as well as experiments

3. *Data Driven Dynamical Modeling and Estimation.* Developed a novel data driven approach of representing the highly non linear system as a linear model in a higher dimensional space and a method for estimating the individual non linear elements. This linear model enables us to capture a wider range of operational region.

1.6 Thesis Overview

The research presented in the thesis will focus on the above three contributions within the scope of the application. We will present the vehicle design and use it as an example for a submerged infrastructure monitoring vehicle using ground effect hydrodynamics. We discuss natural and jet induced ground effect hydrodynamics. The focus of the work is in the application of the phenomenon in regard to design and control of a robotic vehicle; therefore we refrain from scientific analysis at molecular or material science level. We restrict ourselves to observation and application in a tangible engineering system.

In *Chapter 2* we will discuss the design transition from the Omni Submersible to a prototype with a flat bottom and a bottom center jet to enable fluid bed formation. We will explain the choice of key design parameters particularly with respect to vehicle control and specific task. We will also talk about different components onboard and general performance and how such a concept vehicle may be used in real world applications.

We then move to discuss an overview on the vehicle dynamics. This will be done in two parts. In *Chapter 3*, we talk about the different forces that comes into play during motion on a submerged surface, including the hydrodynamic ground effect. This is quite different from free stream motion. We demonstrate some simplified closed loop vehicle control on a smooth 2D plane. This chapter forms the foundation for understanding how we will later integrate the non linear forces into the system model.

In *Chapter 4*, we elaborate on the observation of the natural Hydrodynamic Ground Effect and how it could be exploited for smooth vehicle control. We demonstrate it both through CFD simulations as well as experiments.

Chapter 5 We show jet induced hydrodynamic ground effect for active control of the fluid bed to enable smooth motion on the submerged structures. We also demonstrate the same with both simulations and experiments.

In *Chapter 6* we return to dynamical modeling and discuss a new data driven approach for developing linear models which enables us to capture more of the non linear behaviors of the system.

Chapter 7 We explain how estimation of the individual non linear forces can be done based on the data driven model to simplify the feedback control applied for precise distance maintenance.

Chapter 8 is summarizes our work and lays down the foundation for further work in this area.

Chapter 2

Robot Design

2.1 Introduction

The chapter focuses on the control configured design of EVIE: Ellipsoidal Vehicle for Inspection and Exploration. EVIE is a compact ellipsoidal underwater robot that uses hydrodynamic ground effect for smooth motion on submerged surfaces. As discussed in Chapter 1, this robot is inspired by its predecessor, the Omni Submersible [15], in its spheroidal shape. Both differ in shape, size and propulsion method from what is commercially available for industrial use. They are smooth, ellipsoidal, streamlined, and appendage free, with EVIE having a flat bottom to house sensors that need to be in contact with target surfaces. The flat bottom is well suited to compact NDT sensors like linear array UT modules.

Motion on a submerged surface is very different from free stream or a practically boundless fluid. We start with a review of comparable underwater robots for volumetric inspection and point out the deficits that are being addressed by our research. Some of these have been already addressed in Chapter 1. Next we discuss the choice of various design parameters based on the challenges of motion on a submerged surface. Finally we present the final prototype robot design with onboard electronics and computer that is capable of moving

on a horizontal submerged surface.

2.2 Literature Review

A variety of underwater robots have been developed for submerged infrastructure monitoring [31], but there remains a need for advanced research to enable thorough inspection of underwater structures for defects undetectable by just visual inspection. Volumetric inspection in places like a BWR vessel is extremely challenging due to the complexity of internal structures. We divide these inspection robots into two groups: those which do only visual non-contact inspection; and those which also do on contact or other volumetric inspection, i.e. sub-surface scanning [5] [32]. Vessel examinations – at least in case of power plants – are scheduled during normal refueling shutdowns. It is essential to use fast, efficient methods to avoid unplanned outages costing millions of dollars.

In terms of small compact spherical robots ODIN [33] robot from University of Hawaii is an example that uses several external propellers. The BFFAUV [34] design developed by Licht and Triantafyllou is untethered, capable of multi DOF motions, and highly maneuverable using flapping foils. Although this robot is very agile and capable of multi-DOF motion, it is mostly meant for visual inspection in free stream water and is not ideal for a surface scanning design. Some of the advanced robotic solutions for volumetric inspection are as follows. The AIRIS 21 [20] with a maximum dimension of 21 in. is an example of a tethered underwater robot for on contact, subsurface ultrasonic inspection for cracks in reactors. It uses propeller based propulsion to reach the surface, and vacuum to remain on the surface while it moves with wheels. This method of movement is advanced and unique; but the system is not agile, while the tether and external appendages increases chances of snagging, collisions, and breaking. There are other robots equipped with manipulators. For example URSULA [35] is an underwater robotic system to inspect the welds in the

reactor of a nuclear power plant weighing about 900 lbs. URSULA uses suction cups to latch itself on the wall and then use it's scanning head to go around weld seams.

For surface inspection we developed EVIE, retaining Omni's smooth ellipsoidal shape but with flat bottom. Both use jet propulsion instead of propellers which protrude out of the body, are non ideal for high precision maneuvering through non linearities like dead zones, and suffer from variable time response and asymmetric performances. More discussion can be found in [36].

Assuming UT research would progress alongside, EVIE [27] would be capable of housing a compact linear phased array as shown in the vehicle concept design. This would allow line contact, as shown in Figure (2-2), around a pipe for example. Submerged surfaces – even in such enclosed facilities – may have various rough patches that causes friction in an on contact scanning motion. Since our robot is not equipped with wheels, we needed a method of smooth gliding motion over surfaces. Such motion is enabled by a natural fluid bed, i.e. a thin layer of water between the surface and the bottom of the robot, formed UUV the relative motion along the surface. We found active control of the fluid bed thickness helps move on a rough surface. So in our second iteration, we form a fluid bed layer by pushing water through a center bottom outlet. This water buffer layer smoothens out the roughness but also instills a natural hydrodynamic stability on the top of the fluid bed layer due to the relative flow caused by this active jet. Our robot exploits this hydrodynamic ground effect phenomenon for inspection of submerged surfaces. Use of this ground effect to maintain a precise gap without using complex actuators or active suction is explored extensively in the upcoming chapters. Exploiting near surface hydrodynamics to facilitate motion has never before been done for UUVs and, except for studies of fish locomotion, is an under explored concept.

2.3 Conceptual Vehicle Design

The vehicle was designed based on the functional requirements and challenges presented in Chapter 1. The D' Arbeloff Lab at MIT developed a 5 DOF hydrodynamically unstable, highly maneuverable ellipsoidal robot called the Omni Submersible. The key focus of this robot was its unique propulsion system. The robot used Coanda Valves [36] to function with an under actuated water jet propulsion system, Omni was meant primarily for visual inspection.

The next prototype is the center of this work. The requirement was to transition the design to enable volumetric inspection. Since cracks are often internal, surface examination becomes indispensable. Therefore, the goal was to extend the research to an underwater robot that, besides visual inspection, could carry out surface examination by being in contact with the surface. Of course this required design and functional changes which in turn changed the dynamical modeling for the new system for the new task. Figure (1) shows the Omni Submersible and EVIE.

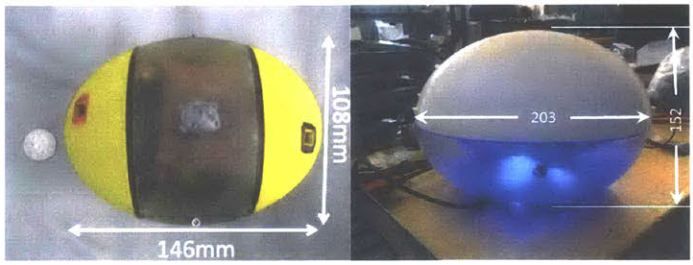

Figure 2-1: Omni Submersible [15] (left) and EVIE (right)

The new robot, EVIE (Ellipsoidal Vehicle for Inspection and Exploration), has a flat base and can house ultrasonic phased array sensors as well as carry localization sensors for positioning the defects. The task requires the electronics move to the bottom of the robot,

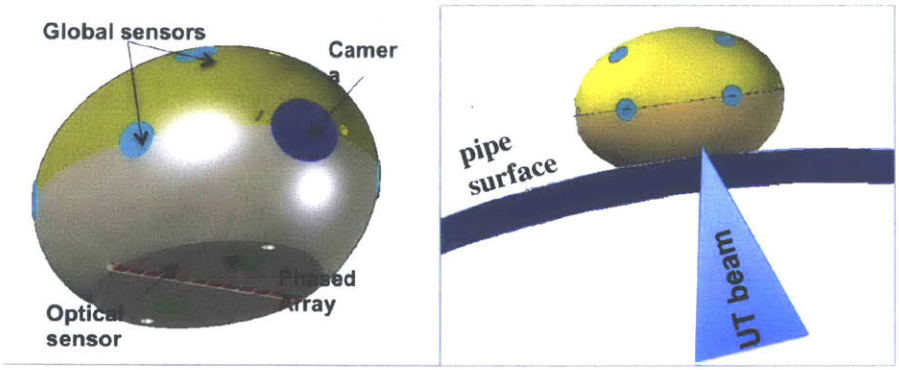

Figure 2-2: Left: Concept design with a phased array sensor (bottom), localization sensors and a camera mounted Right: Movement on a curved surface. Flat bottom housing a linear phased array ensured a line contact even on the curved surface

and the various propulsion jets of EVIE are angled to render stability. The prototype is substantially larger to house different electronics. The propulsion is still done with jets. Ports could share pumps via Coanda valves, as in Omni. But since propulsion and multi-DOF motion are no longer the focus for this work, for simplicity we assume each jet is controlled independently. For the most efficient design, we will be integrating the features of the two prototypes. A center bottom jet allows formation of fluid bed layer for movement on rough surfaces or for hovering near target surface at reduced thrust. A conceptual design in Figure (2-2) shows the robot having acoustic sensors for localization and a phased array sensor on it's base which ensures a line contact for crack inspection.
Our current EVIE is a 7x8 inch ellipsoid. Size can be adjusted to accommodate electronics and sensors, though smaller has better maneuverability. The design can have as many as 8 jets (J1 – J8) as shown in Figure (2-3) for motion purpose. Figure (2-3) shows the propulsion jets are angled for control purposes. The jets are placed on the upper half of the robot which is porous and water filled and are powered by submersible centrifugal pumps. The lower portion is water sealed and houses the electronics and the ballasts. The upper shell is printed using a Stratasys Dimensions FDM 3D printer [37] and the lower

– which houses the electronics – is 3D printed using a SLA printer, since SLA parts are waterproof. A single center bottom jet forms the fluid bed.

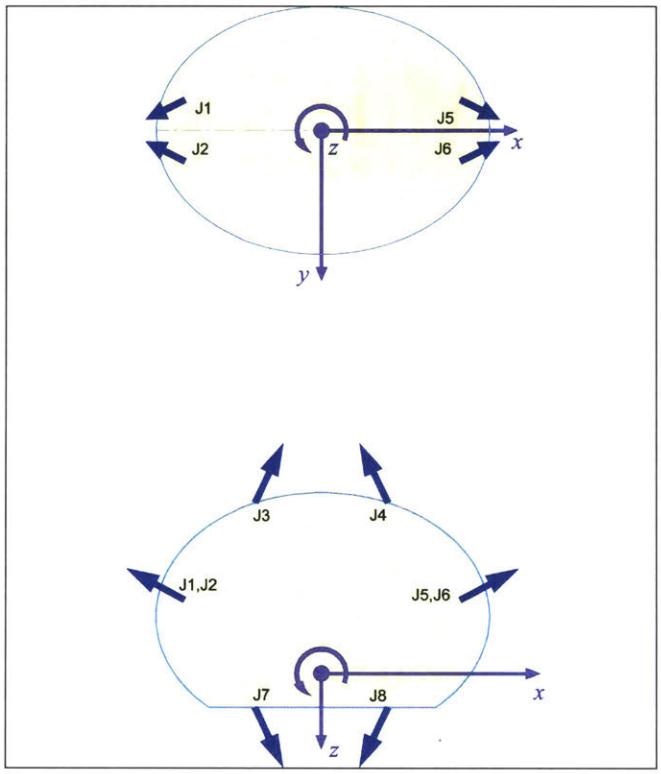

Figure 2-3: Robots with all jets

J3 and J4 are bidirectional jets that control the up-down motion of the robot. They are also angled, at an angle α. This is to allow for pitch control.

Inspection surfaces will not always be horizontal. Prior work at d'arbeloff lab has focussed on methods of shifting the center of gravity [38]; we shall not reiterate that here. For simplicity and clarity, we shall speak of the surface being inspected as horizontal with the robot on top. It is to be understood that other geometries can be accommodated using prior work from d'Arbeloff lab.

Ideally for testing the robot on a horizontal surface, we want the center of gravity of the

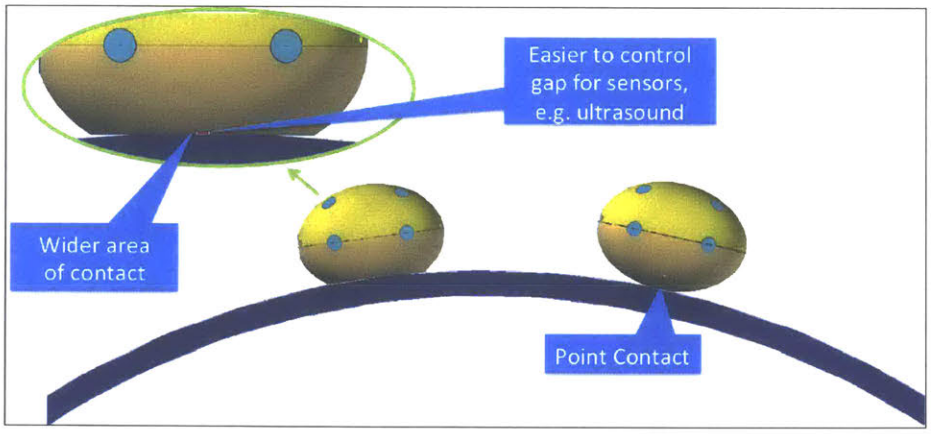

Figure 2-4: Choice of flat versus ellipsoidal base for motion on a surface

robot to be below the center of buoyancy. This was attained by ballast at the bottom of the robot. This ensured a buoyancy righting moment. However, since the jets are in the upper part, they create an undesirable thrust induced pitching moment. This is counteracted by making the propulsion outlets angled at β such that the jet vectors approximately pass through the CG of the system. The choice of jet angles is explained in more details in the next chapter where we discuss the system dynamics and the forces acting on it.

A substantial amount of work on shape analysis has been done previously, including the optimal aspect ratio for controllability. Based on that work an aspect ratio (ratio of the major and minor ellipsoid axis) of 1.4 was chosen, but with one flat surface, the rationale for which is illustrated in in Figure 2-4. [39]

2.4 Onboard components

For remote or autonomous functioning of EVIE we equip it with needed electronics, propulsion system, onboard computing, and localization sensors. For propulsion we used centrifugal pump with symmetric impellers and custom output nozzles as used in Omni Submersible.The onboard computer and other electronics are kept in the bottom chamber.

DOF	J1	J2	J3	J4	J5	J6	J7	J8
+u	✓	✓						
-u					✓	✓		
+v		✓				✓		
-v		✓			✓			
+w			✓	✓				
-w							✓	✓
+q			✓					✓
-q				✓			✓	
+r		✓			✓			
-r	✓					✓		

Table 2.1: Map of jets dominating for various degrees of freedom, i.e. the ones that would be used for movement along a specific axis.

Jet	Angles	F_x	F_y	F_z
J1	β, γ	$\cos\gamma\cos\beta$	$\sin\gamma\cos\beta$	$\sin\beta$
J2	⋮	$\cos\gamma\cos\beta$	$-\sin\gamma\cos\beta$	$\sin\beta$
J5	⋮	$-\cos\gamma\cos\beta$	$\sin\gamma\cos\beta$	$\sin\beta$
J6	⋮	$-\cos\gamma\cos\beta$	$-\sin\gamma\cos\beta$	$\sin\beta$
J3	α	$\sin\alpha$		$\cos\alpha$
J4	⋮	$-\sin\alpha$		$\cos\alpha$
J7	⋮	$\sin\alpha$		$-\cos\alpha$
J8	⋮	$-\sin\alpha$		$-\cos\alpha$

Table 2.2: Angular terms contributing to forces. Note here all forces are given, whereas table 2.1 shows only dominant contributors. For instance, J3 and J7 produce positive F_x but would be an inefficient mode of propulsion compared to J1 and J2.

This is not ideal in that the air filled side naturally flips to the top, but for the scope of the research – test and movement on the horizontal tank surface – this was the most optimal choice. Ballast near the bottom of the robot corrects the problem.
Communication is over low frequency radio that has sufficiently low attenuation in deionized water such as in BWR tanks. This gives the option for remote control or sending simple way point behavior. For localization, we used an IMU with integrated Kalman filter. Relative positioning from surfaces using pulsing lasers was also explored in our research lab [40]. The other interesting work done was development of a sensor module for measuring the thickness of fluid bed layer [41]. The different components developed in association of this micro UUV that would allow this research to transition into a practical application. However, EVIE is used here to demonstrate the novelty of exploiting non linear hydrodynamic surface (ground) effects on UUVs to benefit inspection tasks or other near surface motions. Henceforth the emphasis will be more on the application rather than the design of it.

2.5 Experimental Designs

The major portion of the thesis will focus on ground effect hydrodynamics, and for this we perform two kinds of tests. One set in a tow tank where we tow the vehicle on a flat surface to determine the effect of natural hydrodynamics due to longitudinal motion. The other using an active jet to understand the effect of single jet impinging hydrodynamic motion. For this the experimental vehicle design was fairly simple. We used the same shape, and mounted a submersible centrifugal pump inside that would create the bottom impinging jet. Height control would be done using the jets on the top. The system was restrained to perform only 1-DOF motion. The simplified vehicle design is shown in Figure (5-4). Many variation of the design for creating fluid bed and regulating the flow underbody was also performed[42]. More extensive work is to be done for design optimization for

practical application.

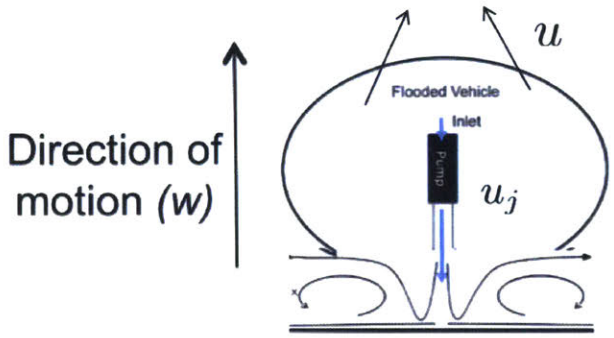

Figure 2-5: Robot with a vertical impinging jet which will be used in in the subsequent chapters to study the effect of thrust induced hydrodynamic effects and active control of fluid bed layer. Note we will use a constant set value of the bottom jet for forming the fluid bed, where as height control is done separately by the top jets (u denotes the control force)

2.6 Conclusion

We presented the design of a novel underwater robot for surface inspection. The robot slides with its shell in contact with the surface, allowing for a variety of inspection tools (optical, magnetic, acoustic). The body has no appendages and communication is wireless, making it ideal for confined spaces. The appendage-free design is hydrodynamically unstable and relies on a control system to achieve stability.

The unique geometry of EVIE along with a bottom jet creates new opportunities to use surface effects as an integral part of the control system. Subsequent work will incorporate ground effects, as well as additional states of the robot. The single bottom jet was a preliminary design to validate the use of fluid film. This can be extended to multiple bottom jets with different type of control, where jet interaction can facilitate ground effect

hydrodynamics for both stability and reduced power hovering at constant distances.

To simplify our experiments with contact forces, EVIE as presented here has a low CG; to operate on anything other than a horizontal surface, it must run the pumps continuously and at high power. Future versions of EVIE will dynamically shift the CG to minimize the power consumed by pumps.

In subsequent chapters this design will be used for study and demonstration of non linear hydrodynamic surface effects.

Chapter 3

Overview of System Dynamics and Forces on the Body

3.1 Introduction

Forces on a body moving in free stream are well known. This chapter introduces the various forces that come into play when moving in contact with, or in near proximity to, a submerged surface. We can broadly divide the forces as the **thrust forces, contact forces, hydrodynamic forces, the body forces**. Thrust is produced by the jet propulsion and allows the robot to have surge, sway and heave. The vehicle designed includes pitch control; roll dynamics is not included.

When the body lands on a submerged surface, contact forces – normal force and and the frictional force – arise. Hydrodynamic forces and moments include the Munk moment, hydrodynamic drag, and the ground effect. Body force would include the weight and inertia. These forces introduce varying degrees of complexity, so we discuss how these enter the equations of motion of this specific robot, and which of these must be taken into account.

The body shape gives rise to what is called the Munk Moment [29] where a streamlined body tends to rotate so the long axis is perpendicular to the direction of the flow. This

occurs both in free stream as well as while moving on a surface. Unique to on contact motion, asymmetric friction on the surface can also lead to torque and has to be counteracted. We introduce preliminary control techniques for a 2D plane and validate it on a horizontal submerged plane.

Highly non linear hydrodynamic ground effect forces add a new level of complexity in the system modeling. This will be introduced briefly in this chapter and explored in depth in subsequent chapters.

This chapter gives the complete overview of the dynamics of the system; hereafter we shift from that aspect to focus on investigating the non linear forces in depth. However, the simplifications in the problem statement in the upcoming chapters derive from the mathematics explained here and therefore this lays the foundation for understanding the dynamical system behavior as a whole.

3.2 Forces on the System

Forces acting on the system can be broadly classified as follows.

1. Input Forces
    - Thrust caused by propulsion jets for moving surge, sway and heave motion
    - Thrust caused by center bottom impinging jet. The main function of this jet is forming fluid layer to smooth surface; but at larger heights, this jet can be used for additional upward thrust combined with fountain upwash.
2. Contact Forces
    - Friction
    - Normal Forces

3. Hydrodynamic Forces

    - Hydrodynamic Drag (linear or non linear)
    - Munk Moment
    - Hydrodynamic Ground or Surface Effects

4. External Forces

    - External Disturbances including turbulence and sudden perturbations
    - Controlled perturbations or external inputs to study system response

We will now describe each of them and explain how they affect our design choices. We will not be taking turbulence or other external forces into account.

3.2.1 Input Forces

As explained previously, to avoid problems of snagging and directional limitations of external appendages we use jet actions for propulsion. Fluid jets exit through nozzles which are angled appropriately based on constraints discussed later in this chapter. Thrust forces are produced by the submersible micro pumps housed inside the robot.The angled jets produces two different thrust components for movement along a plane which help either in surge (longitudinal) or sway (lateral) motion.

Assume independent control over each of the jets $J1, J2, J5, J6$, with corresponding forces F_i. See figure 3-1. Jets $J3$, and $J4$ can be made bidirectional and do not need independent control. The bottom center impinging jet is controlled independently and denoted by J_j, the corresponding force as F_j. External perturbation forces can be denoted by u_{ext}.

The nozzle angle γ is a trade off between the thrust force in u versus v. In cases where surface scanning requires considerable lateral motions, like performing C-scans, the angle

should be chosen such that both components of the thrust get comparable weights. Here we mostly demonstrate longitudinal motion, u is taken as the dominant velocity, and γ is selected to be just large enough to counteract the Munk moment. Angle β is associated with a third component: the $\sin\beta$ component of the thrust helps prevent thrust induced pitching while moving on a horizontal plane.

The x, y, and $z$components of the forces and moments acting on the body are summarized as follows.

Jet forces:

$$F_x = (F4 - F3)\sin\alpha + (F1 - F5 + F2 - F6)\cos\gamma\cos\beta$$

$$F_y = (F1 + F5 - F2 - F6)\sin\gamma\cos\beta \tag{3.1}$$

$$F_z = (F3 + F4)\cos\alpha + (F1 + F2 + F5 + F6)\sin\beta + F_j$$

Jet Moments

$$M_x = (F1 + F5 - F2 - F6)\sin\beta L_{tv} + (F1 + F5 - F2 - F6)\sin\gamma\cos\beta L_{tw}$$

$$M_y = (F3 - F4)\cos\alpha L_{pu} + (F3 - F4)\sin\alpha L_{pw} + (F1 + F2 - F5 - F6)\sin\beta L_{tu} + (F1 + F2 - F5 - F6)\cos\beta\cos\gamma L_{tw}$$

$$M_z = (-F1 - F6 + F2 + F5)\cos\gamma\cos\beta L_{tv} + (-F1 - F6 + F2 + F5)\sin\gamma\cos\beta L_{tu} \tag{3.2}$$

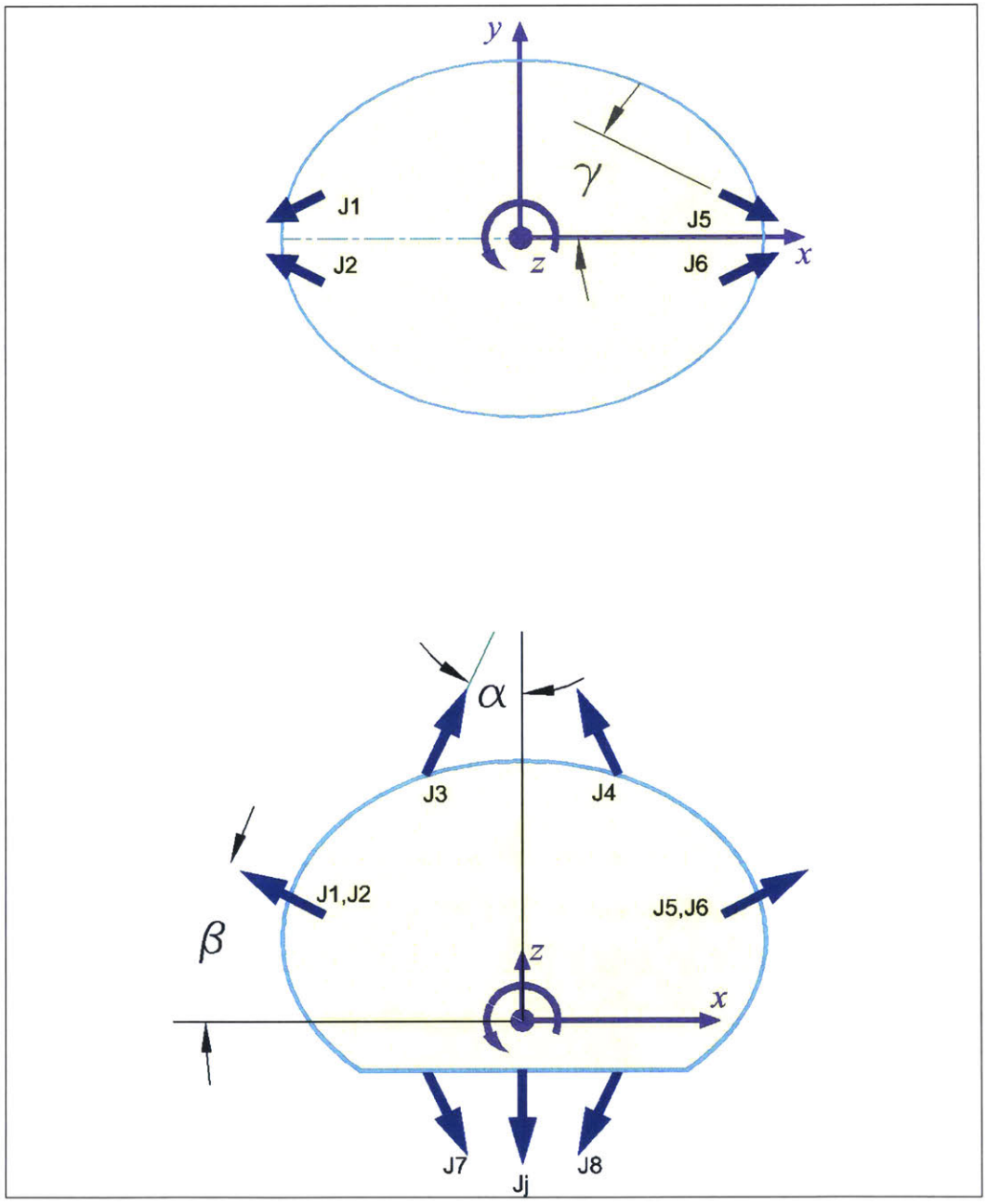

Figure 3-1: Top and Side View of EVIE-2. Arrows indicate the jet direction

For small γ, velocity u and F_x are dominant over v and F_y.

3.2.2 Contact Forces

Contact forces introduce a discrete change in vehicle dynamics as it transitions between the states shown in figure 3-2: free floating (state 0); contacting across surface (our desired condition, state 1), and point contact when pitching nose up or nose down (states 2 and 3). We develop generalized equations that are valid for all cases: setting the normal force, $N = 0$ is equivalent to placing the robot in a boundless fluid. On the surface, the normal force is not fixed. In state 1 (flat), the magnitude and location of the normal force varies with velocity; in states 2 and 3 the normal force also varies with pitch angle (due to hydrodynamic lift) as well as pitch rate (since the CG moves as pitch changes).

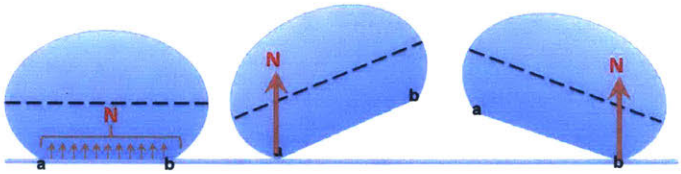

Figure 3-2: Transitional states of the Robot

The other possible states of the robot are roll, and roll and pitch combined. Neither roll nor pitch is beneficial during inspection. But the pitching moment is 10x larger than the roll moment because $|v| \ll |u|$. Furthermore, we intend a future prototype will have pitch control to climb over obstacles. Therefore, in this prototype we include pitch, but not roll. The flat bottom of the robot is sufficient to counteract small roll forces.

Friction is the other contact force that is highly non linear and coupled with the normal force. Friction models in a hydrodynamic environment can be quite complex [43],[44]. At the low speeds required for inspection, transition between static and dynamic friction, like Stribeck effect [45], need to be considered. Depending upon the velocity of the robot

and surface roughness, a thin layer of fluid between the contacting surfaces can cause viscous friction. Our robot has weight minus buoyancy of approximately 0.1N; taking the coefficient of friction as 10% friction force is on the order of 0.01N compared to jet forces of order 0.1N. Friction is large enough to merit inclusion, but not so large as to warrant detailed analysis. We assume the moving robot has a kinematic friction force of $\mu_k N$. For the research discussed here static friction is not used: we will work with a moving robot. Note, however, friction coefficient may approach 100% on rusty or concrete surfaces. The control system technically must be able to handle such cases without *a priori* knowledge of the surface.

3.2.3 Hydrodynamic Forces and Moments

The main hydrodynamic forces and moments that can influence the robot are the drag, Munk moment and the hydrodynamic ground effect [29]. Hydrodynamic drag is quadratic for high Reynolds number, as in our case; but at low velocities it is linear in nature. The other prominent highly non linear force is the hydrodynamic ground effect- that is the forces on the body due to the presence of the ground.

Munk Moment

The term $X_{u|u|}$, $Y_{v|v|}$ and $Z_{w|w|}$ are hydrodynamic coefficients that account for the different lateral and longitudinal forces acting on the body. The dominant velocity of the robot is along u; hydrodynamic moments associated with motion in u are accounted for by $M_{u|u|}$. The Munk Moment is a destabilizing moment. In the absence of pitch, the Munk moment is exclusively in the xy plane and is given by

$$M_m = \frac{1}{2}(Y_{\dot{v}} - X_{\dot{v}})U^2 \sin 2\zeta \tag{3.3}$$

where ζ is the sideslip angle. In our case, with zero pitch and still water, $u = U\cos\zeta$ and $v = U\sin\zeta$ so

$$\begin{aligned} M_m &= (Y_{\dot{v}} - X_{\dot{v}})(U\sin\zeta)(U\cos\zeta) \\ &= C_{mm}uv \end{aligned} \tag{3.4}$$

where $C_{mm} = (Y_{\dot{v}} - X_{\dot{v}})$. Therefore Munk moment enters both the pitch and the yaw equations of motions. Below are the equation of motion for the robot, which is assumed to move predominantly in x.

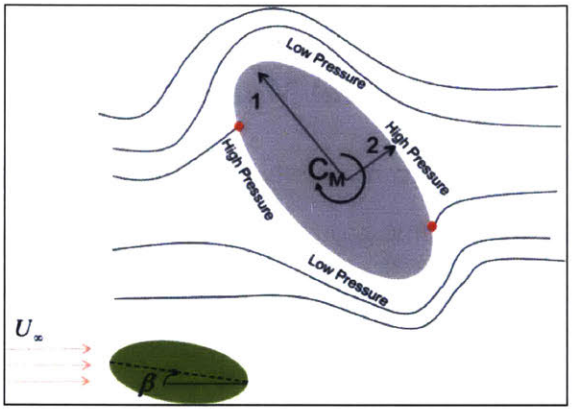

Figure 3-3: Munk Moment, Reference to figure [39]

Hydrodynamic Ground Effect

The hydrodynamic coefficients given above are constant for a body in an unbounded fluid. Near a surface the values will depend upon the distance to the ground and the angle relative to the ground. This is generally part of the ground effect: non linear forces that depend on, and affect, the motion of the body. The potential benefit of the ground was a discovery while simulating the body moving with a small fixed distance over the surface to avoid surface roughness. The simulation showed a restoring force to a fixed distance from the surface. The phenomenon was then confirmed with experiment. Subsequent chapters will

discuss how to maintain and utilize this behavior for 2D motion. But in this chapter, we assume either free-stream or true contact with the surface and show the necessity of the fluid bed.

3.2.4 Simplified Equation of Motions, neglecting roll and ground effect hydrodynamics (no bottom jet)

Below are given the generalized equations of motions for our non linear model of the robot. Note the equation for $\dot{p}$ is derived from the requirement $\dot{\phi} = 0$.

$$
\begin{aligned}
\dot{u} =& \frac{1}{(m - X_{\dot{u}})}(F_x - (mg - F_b)\sin\theta + Nsin\theta \ - X_{u|u|}u|u| - \mu_k N\frac{u}{V} - m(qw - rv)) \\
\dot{v} =& \frac{1}{(m - Y_{\dot{v}})}(F_y - Y_{v|v|}v|v| - \mu_k N\frac{v}{V} - mru) \\
\dot{w} =& \frac{1}{(m - Z_{\dot{w}})}(F_z + (mg - Fb - N)\cos\theta - Z_{w|w|}w|w| - \mu_k N\frac{w}{V} + mqu) \\
\dot{p} =& -\sec^2\theta(q\sin\phi + r\cos\phi)\dot{\theta} - \tan\theta(\dot{q}\sin\phi + \dot{r}\cos\phi) \\
\dot{q} =& \frac{1}{(I_{yy} - M_{\dot{q}})}(M_y - \mu_k N\frac{u}{V}L_{nw} + NL_{nw}\sin\theta - F_b L_b\sin\theta - M_{q|q|}q|q| + M_{u|u|}u|u| + C_{mm}uw) \\
\dot{r} =& \frac{1}{(I_{zz} - N_{\dot{r}})}(M_z - N_{r|r|}r|r| + C_{mm}uv) \\
\dot{\theta} =& q \\
\dot{\psi} =& \frac{r}{\cos\theta} \\
\dot{X} =& u\cos\theta + v(-\sin\psi) + w(\cos\theta\sin\psi\sin\theta - \cos\psi\sin\psi) \\
\dot{Y} =& u\cos\theta\sin\psi + v\cos\theta\cos\psi\sin\psi) + w(\cos\theta\sin\psi\sin\theta - \cos\psi\sin\psi) \\
\dot{Z} =& w\cos\theta
\end{aligned}
\tag{3.5}
$$

In state 1 – contact with a surface, without pitch or roll – we have $Z = \phi = \theta = 0$ and the

remaining equations simplify further.

$$\begin{aligned}
\dot{u} &= \frac{1}{(m - X_{\dot{u}})}(F_x - X_{u|u|}u|u| - \mu_k N\frac{u}{V} + mrv) \\
\dot{v} &= \frac{1}{(m - Y_{\dot{v}})}(F_y - Y_{v|v|}v|v| - \mu_k N\frac{v}{V} - mru) \\
\dot{r} &= \frac{1}{(I_{zz} - N_{\dot{r}})}(M_z - N_{r|r|}r|r| + C_{mm}uv) \\
\dot{\psi} &= r \\
\dot{X} &= u\cos\psi - v\sin\psi \\
\dot{Y} &= u\sin\psi + v\cos\psi
\end{aligned} \tag{3.6}$$

For quantitative analysis we calculate the hydrodynamic coefficients using published formulas for ellipsoids. These formulas measure moments around the geometric center, whereas we wish to do so around an off-center CG. In particular, $M_{u|u|}$ is zero if the CG is at the geometric center, but would not be so for us. We approximate the torque from as the drag force in x, $X_{u|u|}u|u|$, times the distance from the CG to the geometric center, L_{cgw}. We varied $M_{u|u|}$ as $X_{u|u|}L_{cgw}$ to $2X_{u|u|}L_{cgw}$ in our simulations, and for the desirable (non pitched case) it doesn't make a difference.

3.3 Technical Challenges of Moving on a Plane

There are many technical challenges of moving on or near a submerged surface for inspection. For a flat bottomed UUV like EVIE moving only using water jets, surface roughness is a big concern. This can hinder surface scanning, cause the robot to pitch or yaw from getting stuck on a patch of rough area. Maintaining close contact at all times is extremely necessary for thorough UT inspection.

In our research we break the study of the robot into three discrete states as shown in Figure (3-2). State 1 is the desired state: the robot moving on a horizontal plane, maintaining

contact with the ground at all times. States 2 and 3 are undesired states that the robot can enter into due to different non ideal situations. In this part of our research we will elaborate on the first case, that is the robot is moving on a horizontal surface and constrained to the XY plane. To find the necessary conditions to be satisfied to have the desirable state, we need to find the conditions that would cause the robot to enter state 2 or 3.

3.3.1 Choice of Jet Angles

Based on previous work [39] we see how the jet angles affect the controllability of the system depending upon the pole zero dynamics. For e.g straight jets would make the corresponding linearized system uncontrollable due to the pole zero cancellation, outward jet causes non minimal phase issues which makes the robot first turn in the opposite direction when control is applied, whereas inward jet renders the system controllable and is therefore the ideal choice Figure (3-4). When moving on a plane, the specific angle chosen depends on two issues. First, hydrodynamic Munk moment causing yaw torque. Second, asymmetric friction – more on one side than the other – can cause the robot to turn. We need enough leeway to allow the robot to make sufficient correction to perturbation in yaw angle.

3.3.2 Choice of Jet Angle: γ

If the robots had straight jets with no angle it would be uncontrollable in free stream, while on a plane it would only be able to correct against Munk moment for sideslip angle $\varepsilon \leq 6^\circ$. Assuming simple surface friction on stainless steel and other inspection metals, the maximum frictional (asymmetric) was assumed to be $0.5N$: 50gm net weight (underwater) and $\mu_k = 1$. Choice of γ is a trade off between the propulsion $\propto \cos\gamma$. and yawing toque $\propto \sin\gamma$. We found from the curve below that a $\gamma = 35^\circ$ suffices to stabilize against both frictional torque and Munk moment.

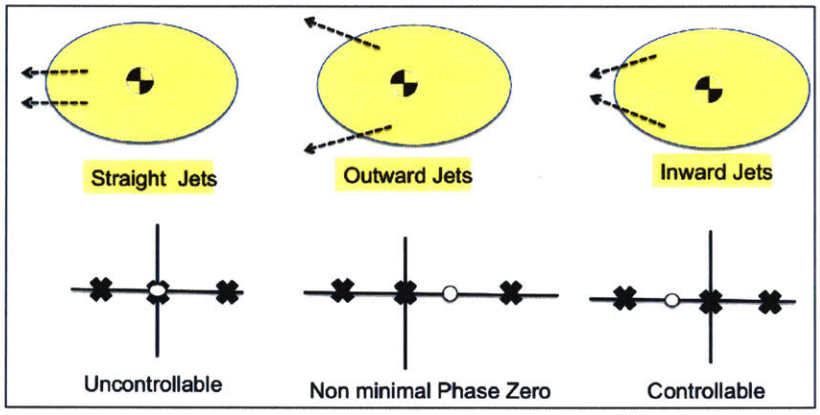

Figure 3-4: Choice of inward versus outward angles- based on the pole zero locations of the dynamical system [15]

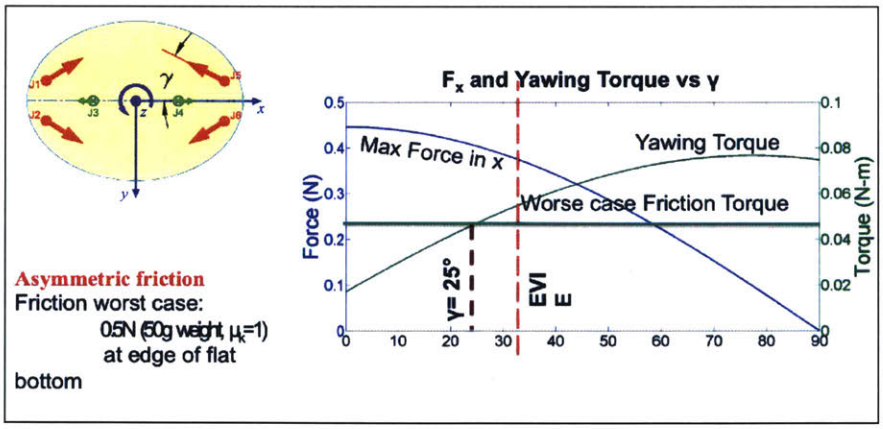

Figure 3-5: Choice of jet angle based on surface friction

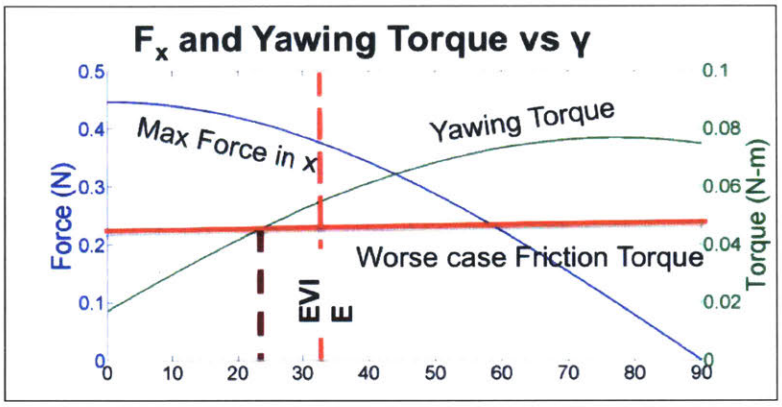

Figure 3-6: Choice of γ that satisfies both

3.4 Linearized dynamics constrained to XY plane

Assume we satisfy the constraints discussed and take the robot as moving only in the XY plane. The robot has no velocity in z, no pitch, and no roll, i.e. $\dot{Z} = \theta = \phi = 0$. We are hence looking at the states u, v, r, ψ.

Take as for our trim state the robot is on the surface and moving with a velocity $U_c = .35m/s$ in the x direction. All the other states are zero: $v = r = \psi$=0. To complete our trim state conditions we need to find the input forces at the trim state which are F1, F2, F5 and F6 that will satisfy $\dot{x} = f(x,u) = 0$.

The normal force in this case is

$$\boxed{N = mg - F_b + F_z cos(\theta) - F_x sin(\theta)} \tag{3.7}$$

Note this is valid only for a constant pitch angle.

We could have divided the system into the lateral and longitudinal states, but for a robot constrained to the ground this was not necessary. Further, we would like to control the heading angle, as well as speed. Hence we choose the 4 state variables u, v, r, ψ. The

generalized linearized state space model is given by

$$\begin{bmatrix} \Delta\dot{u} \\ \Delta\dot{v} \\ \Delta\dot{r} \\ \Delta\dot{\psi} \end{bmatrix} = \begin{bmatrix} \frac{-2X_{uu}U_c}{S_x} & 0 & 0 & 0 \\ 0 & \frac{-\mu_k N \frac{U_c}{V}}{Sy} & \frac{-mU_c}{S_y} & 0 \\ 0 & \frac{C_{mm}U_c}{S_r} & 0 & 0 \\ 0 & 0 & 1 & 0 \end{bmatrix} \begin{bmatrix} \Delta u \\ \Delta v \\ \Delta r \\ \Delta\psi \end{bmatrix} + \begin{bmatrix} 1 & 0 & 0 \\ 0 & 1 & 0 \\ 0 & 0 & 1 \\ 0 & 0 & 0 \end{bmatrix} \begin{bmatrix} F_x \\ F_y \\ M_z \end{bmatrix} \tag{3.8}$$

3.5 Control Design

The system is modeled considering predominant motion in surge. This open loop plant is inherently unstable due to the associated Munk moment which depends on the difference of the added mass in x and y. For longitudinal motion, sway yaw dynamics gives rise to a positive eigenvalue that contributes to instability of the system as seen in figure 3-7. The instability is triggered by turning jet 2 off for 50 ms. As shown in figure 3-14 the controller was successfully able to stabilize it. Data is from the on-board IMU with an integrated Kalman filter to remove noise.

To have a good control authority on a robot requires a good design. For example, the open loop behavior of EVIE-1, with $\beta = \gamma = 0$, gave rise to a pitch angle. This was investigated through our simulations and we were able to reproduce the effect. For $\beta = 0$ the propulsion jets had considerable moment arm along z, causing a nose down pitch. Further, the Munk moment caused the circular motion as seen in Figure (3-8) at a constant but small pitch angle. The robot never moved forward but stayed stuck in place.

The open loop poles of the system are shown in Figure (3-4). As $F_y \propto \sin\gamma$, if $\gamma = 0$ it

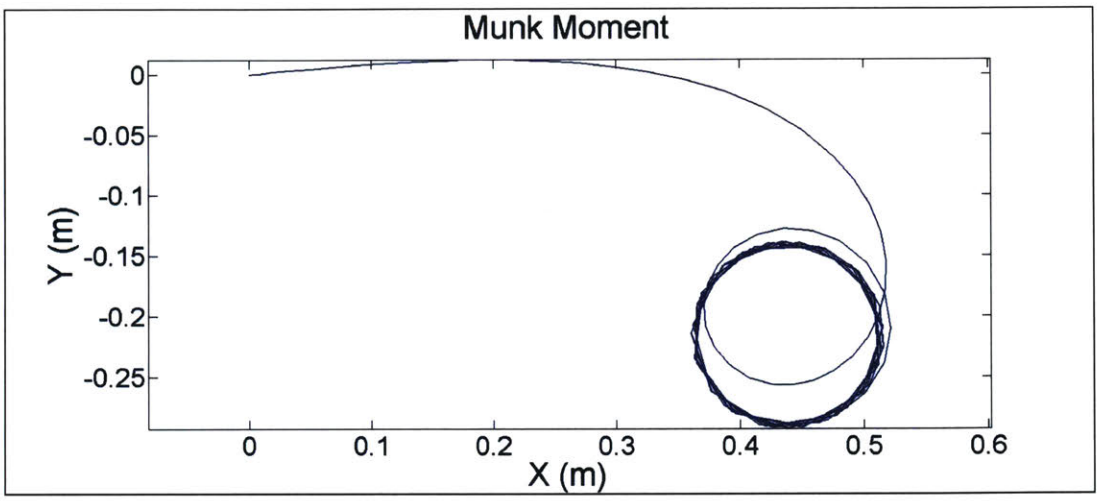

Figure 3-7: Open loop system showing instability due to Munk Moment (motion in circles) on a 2D plane underwater

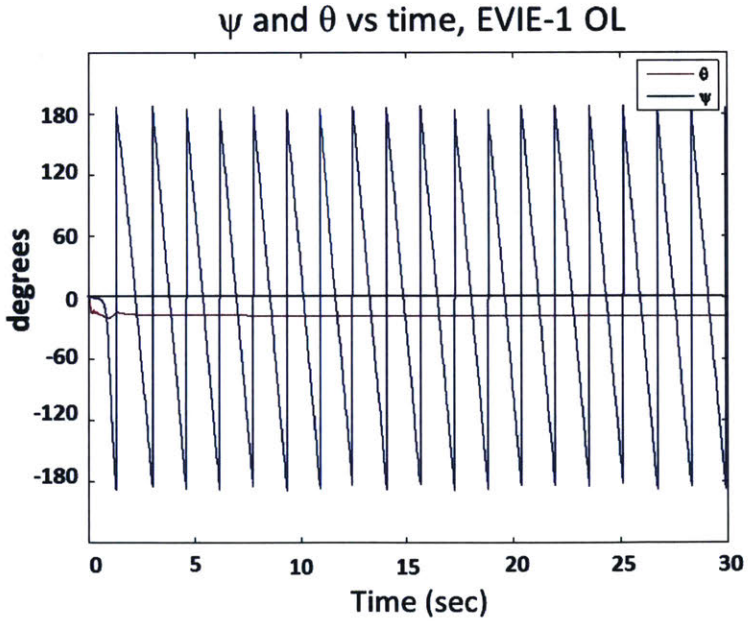

Figure 3-8: Constant pitch angle when β is zero, combined with yawing

can be seen, there is no control over v: the model is uncontrollable. Larger γ would render more control over v and yaw, but it reduces the thrust in u. As the desired velocity is primarily u, we chose as our compromise $\gamma = 30°$.

To stabilize the robot on a horizontal surface, simple controllers like LQR or PID can be used to mitigate against undesirable yawing moments. Note the control system for the full hybrid model would involve a much more complex control algorithm which takes into account the switching between the different states. Such concepts have been discussed, and in future research, integrating the control algorithms for different states will be necessary. For the simulation, we assume the robot has independent control over all jets and has a full state feedback system. A LQR controller was designed for simulation purpose. As shown before, F_y or F_x or M_z are combinations of various jets. We map back to the combination to get individual jet forces. The LQR controller result is shown in Figure (3-9)

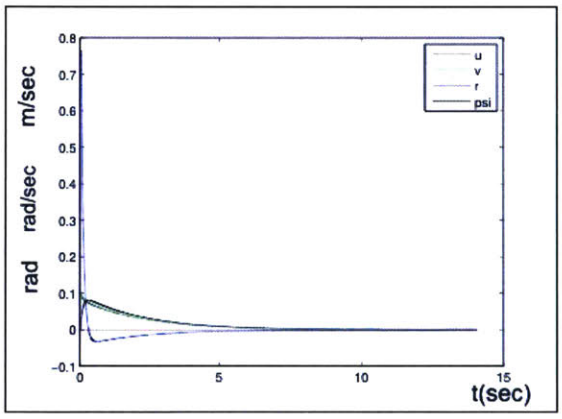

Figure 3-9: Closed loop control using LQR on linear model. Figure (a) shows the linear model control. Figure (b) shows the use of the controller on the non linear model

For our current prototype with only a yaw angle feedback we designed a PD controller (like in the Omni Submersible [46] which corrects for instability due to the Munk Moment. This can be represented as:

$$\Delta Mz = K_1 \frac{d}{dt}(\psi_d(t) - \psi(t)) + K_2(\psi_d(t) - \psi(t)) \tag{3.9}$$

where ψ_d is the desired yaw or heading angle, and K_1 and K_2 are derivative and proportional gains.

3.6 Hardware Implementation and Experimental Results

We started with two initial prototypes. EVIE-1 was a simple demonstration of a surface following underwater robot. It had two pressure jets and four propulsion jets. None of the jets were angled. The design didn't allow much scope for a closed loop control and as discussed was uncontrollable.

We performed experiments on EVIE-1 by making it slightly heavier than neutral buoyancy and putting it on a horizontal surface under water. When jets J1 and J2 were turned on to propel the robot in u, the robot instead of going forward suffered a nose down pitch and went in circles as seen in the simulation in figure 3-8. In figure 3-11 one sees the small θ angle of the robot as it yaws.

EVIE-1 had jets that come out straight and therefore the length of moment arm in z to the CG gave rise to a nose down moment. The frictional force also contributed to the pitch down moment. The velocity u being small, the drag couldn't compensate for this. The Munk moment, combined with accidental sideslip perturbation, resulted in a constant yaw rate and the robot going in the circles as shown in Figure (3-11).

EVIE-2 has two kinds of jets: propulsion and pressure. As explained in the design concepts, to avoid pitching from propulsion jets, the angle β was introduced to eliminate thrust induced pitching moment due to the low position of the CG.

Even though thrust induced pitching was eliminated, open loop system was still unstable due to the Munk Moment. We used a simple PD controller to stabilize it and maintain

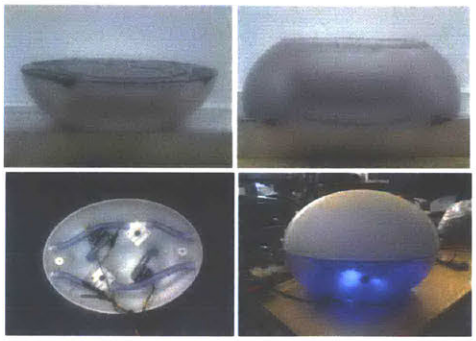

Figure 3-10: EVIE-1. 4 pumps in the submersible part. Straight jets. Water sealed part contains electronics including IMU and localization sensors

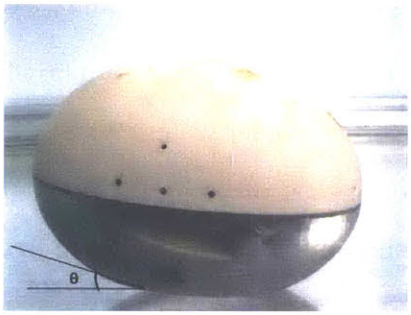

Figure 3-11: Nose down pitching moment exhibited by prototype 1 of EVIE

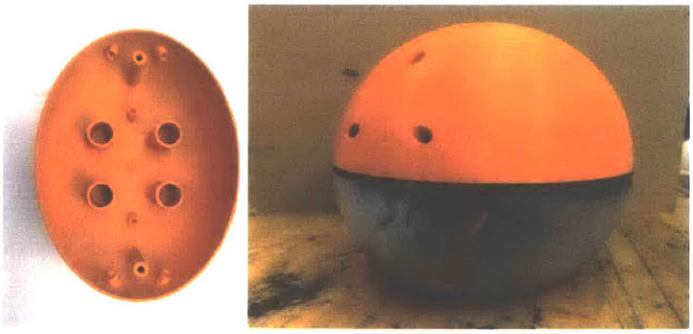

Figure 3-12: EVIE-2 with angled jets

a heading angle. Figure(3-13) shows the open and closed loop response, with the robot moving straight on contact with a low friction surface (glass tank).

To test the validity of the controller, a disturbance was injected to the system by forcing jet 2 to remain off for 50ms As shown in Figure (3-14) the controller was successfully able to stabilize it. Data is from the on-board IMU with an integrated Kalman filter to remove noise.

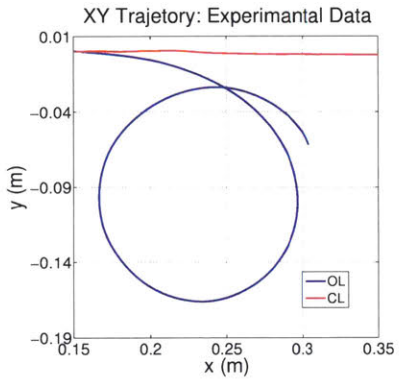

Figure 3-13: Experimental data on open(blue) and closed(red) loop trajectory

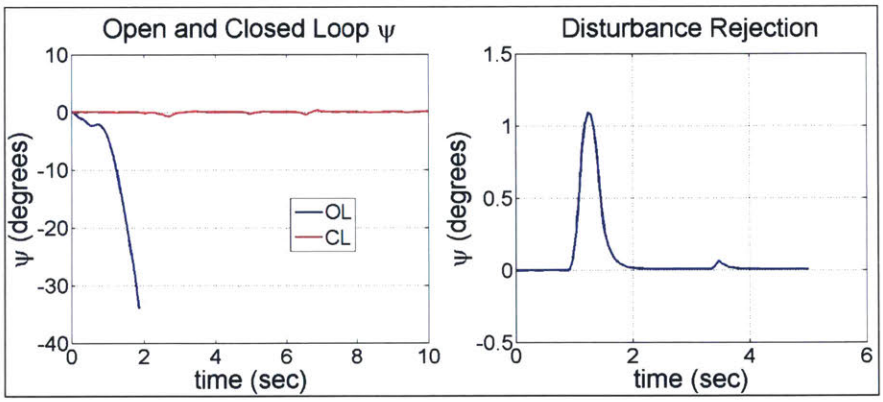

Figure 3-14: Closed Loop Control of EVIE-2. Comparing to open loop (left). Recovery from disturbance (right). Angles measured by on-board IMU.

As seen, for a low friction case, a simple PD controller is able to control the heading angle successfully. For high friction, one should note the Munk moment would face a breaking torque that would substantially reduce the yaw rate. Experiments with different friction models are yet to be done. Next as we shall see, a bottom jet was integrated with this design to allow the fluid bed layer formation and use the benefits of ground effect hydrodynamics for motion near a surface.

3.7 Conclusion

This chapter expanded d'Arbeloff Lab's unique hydrodynamically unstable underwater robot from operating only in free steam to also moving in contact with a surface. Detailed modeling and analysis has been presented based on the simulation of the full non linear model. Control techniques for stabilization have been discussed. Initial experimental results for yaw stabilization has been shown, though full state feedback controller is under development.

The limitation of this work comes from the complexity of hydrodynamic effects near a surface, i.e. hydrodynamic ground effect. We found that minimal surface roughness can impede smooth motion. And the near surface behavior was highly non linear. Thus a lot of dynamics remained unmodeled. Later chapters explicitly study ground effects and how to integrate it in the dynamical model.

Chapter 4

The Natural Hydrodynamic Ground Effect

4.1 Introduction

In this chapter we turn to the core invention associated with this thesis: hydrodynamic ground effect. We show how near surface hydrodynamics can lead to self stabilizing behavior at a precise gap from a submerged target surface. The underlying principles come from lubrication theory and the Venturi Effect which combine to a zero force – $F_z(z) = 0$ – at a particular gap to the surface. If the gap is decreased, the force is positive, pushing the body away; while at larger gaps, the force is negative and pulls the body back – that is, $dF_z(z)/dz < 0$. Thus we have a stable equilibrium. The equilibrium position can be controlled by jets which add to or subtract from F_z.

We further show this force in z can be a result of the relative motion between the surfaces, i.e due to longitudinal motion of the robot with respect to a surface and the resultant flow field. This is conceptually similar to air bearing sliders on hard disk drives. It can also be generated by a downward jet to more explicitly generate a flow field, allowing the body to hover at a fixed distance. Ground effect force is found to be primarily a function of the ratio ε of the characteristic body length and the distance from the ground. Limitations in

the restoring force are considered in the stability analysis included in this chapter.
This self stabilization method opens a whole new door for near-contact subsurface inspection of underwater structures by autonomous vehicles as well as precision distance maintenance in underwater environment. In this chapter we introduce the concept of natural hydrodynamic ground effect and a general understanding through simulation and experimental results in associated with EVIE. Subsequent chapters continue into control algorithms to deal with this highly beneficial, but also highly non-linear, force.

4.2 Literature Review

EVIE was tested in the acrylic tank with the tank floor smooth and with deliberate roughness. On-contact surface scanning can be slow if the surface is not smooth. It has been found that even minimal surface roughness decreases velocity by over 30% when compared to free stream; while tacky material (Vaseline) results in a significant speed fluctuation. Therefore, non-contact inspection is desirable. It that would provide faster and more reliable inspection without being disturbed by the surface roughness and its varying properties. Both for port security and maintenance of reactors, high speed inspection is extremely advantageous. As explained in introduction, our goal is to stay at distances from target surfaces such that we could still do high fidelity subsurface scanning[16] .
Some well known applications using the fluid flow effects in the vicinity of the ground, and their relation to our work, are worth mentioning here. Fluid forces on the body due to the presence of ground depends on the characteristic gap ratio, $\varepsilon = h/c$, where h is the distance of the surface from the ground and c is the chord length of the body. A Formula 1 race car uses the fact that at $\varepsilon \sim 0.1$ the body experiences a suction (Venturi) force which enables greater acceleration. However, for $\varepsilon < 0.08$ it was found that boundary layers merge and instead a lift force occurs [49],[23]. Another well known example is the wing in ground

effect (WIG) vehicles [50] where lift is enhanced by the water surface underneath. However, for self stabilization, instead of a constant down (car) or up (WIG) force, our goal is a zero force region with a steep gradient. A more relevant example is the air bearing slider mechanism for hard disk drive (HDD) [48]. Figure 4-1 (*credit* [47], B. Thornton and DavidB Bogy) shows a graph of how the Z force varies in a slider as the gap h is changed. The graph shows the slider has a stable region at 2nm, where $F_z = 0$. Greater than 2nm, the slider experiences a suction force to bring it back to the stable point. When h is less than 2nm, slider experiences a lift force to push it up to the stable point. HDD calculations are complicated by the distance scale. At the < 10nm fly height of a modern HDD, the gap is comparable to the mean free path of molecules in air. Navier-Stokes must be modified to incorporate intermolecular terms.In this chapter we will explore the possibility of imitating the qualitative behavior of HDD slider in a macro scale in an underwater environment for self stabilization of autonomous robots for surface inspection.

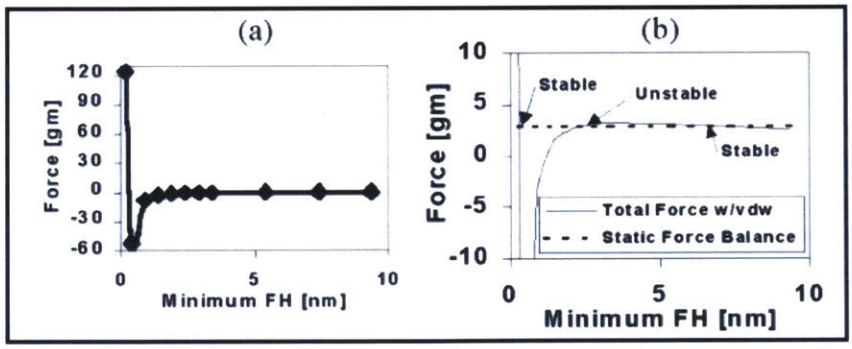

Figure 4-1: Stability curve: F_z versus gap for a HDD slider [47]

We have previously discussed existing solutions for submerged surface inspections. These robots are generally large and propelled by powerful actuators. The proposed ground-effect approach will provide an effective alternative to those existing robots. It is expected that we can build a compact, untethered robot that can maneuver across rough surfaces and

scan them with higher speed.

4.3 Theory

Ground effect is the change of fluid field around the body due to the presence of an external surface, whether or not that surface is the ground. Depending on the shape, geometry and most importantly the characteristic gap ratio $\varepsilon = h/c$, a body moving near the vicinity of an external surface experiences lift, suction or can even be self stabilized. For simplicity, we can define three regions in the flow field near the surface underwater:

a) Region extremely close to the surface: Flow in this region is most effectively understood through the interaction of the boundary layers [53].

b) Region close to the surface but greater than the boundary layer thickness. There is a flow channel between the body and the surface. Flow in this region is governed by a combination Bernoulli's effect and enhanced by Couette Flow [55]. Increased velocity in this channel leads to low pressure (suction) which is called the Venturi Effect.

c) Region further from the surface where the effect of the ground becomes less pronounced and the the flow transitions into the unbounded medium.

The robot EVIE is an ellipsoid with a flattened base. An analytical expression of 3D fluid flow around the body is not feasible. Hence we will try get a general understanding of the phenomenon using common 2D flow examples.

4.3.1 Boundary Layer Effect

When the body is extremely close to the surface, lift forces experienced can have explanation through many theories. Assuming the robot started moving with perfect contact, at steady

state a layer of thin film is developed underneath it on which the robot rests while continuing its longitudinal motion. For gap sizes of 2mm, we can use the well known lubrication theory which deals with interaction of boundary layers as two surfaces move in relative motion. Flow here is highly viscous and the reduced Reynolds number is given by $\varepsilon^2 Re$. For simplicity a small region just above the base of the robot to its bottom, can be modeled as a inclined slider of variable height fixed over a moving surface as shown in the Figure (4-2)

Note, the picture is exaggerated.

Consider a stationary slider (inclined plane) over a surface. Fluid motion is primarily in in x and is given as $v_x = u(z)$. The governing equations are 2D Navier-Stokes for incompressible flow,

$$\frac{dp}{dx} = \eta \frac{\partial^2 u}{\partial z^2} \tag{4.1}$$

and Reynold's equation for lubrication theory:

$$\frac{\partial}{\partial x} \frac{h^3 \partial p}{\partial x} = 6U\eta \frac{dh}{dx} \tag{4.2}$$

where $u = U$ is the fluid velocity at $z = 0$ (surface) and $u = 0$ at $z = h(x)$ on the static bottom surface of the wedge (no slip conditions), η $h(x)$ and $p(x)$ are viscosity, height and pressure, respectively.

Let $h(0) = h_i$ at point A ($x = 0$) and $h(L) = h_o$ at B. The pressure expression for the inclined plane is given by,

$$P(x) = \frac{6\eta UL}{h_i/h_0 - 1} \frac{h_i}{(h_i + h_o)} \left(\frac{1}{h} - \frac{1}{h_i}\right) \left(\frac{1}{h_o} - \frac{1}{h_i}\right) \tag{4.3}$$

The inlet pressure is P_i at x=0 (point A). From the above equation, the maximum pressure P_o occurs at for $h = h_o$ (point B). This flow then feeds the region from B to C with constant $h(0 < x < L) = h_o$. This middle region can be treated as parallel plates with a linear drop

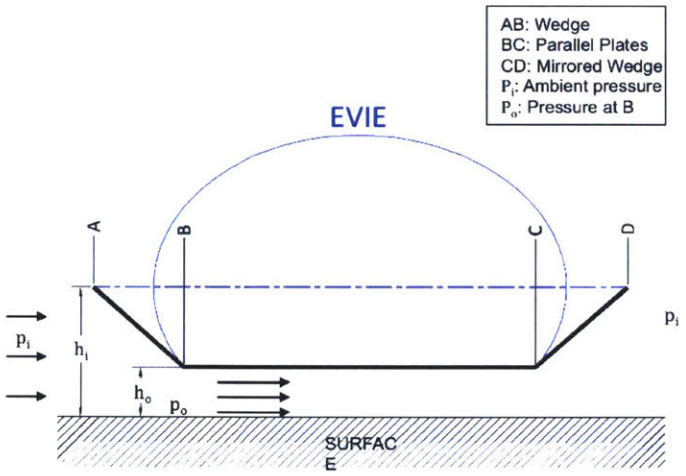

Figure 4-2: Simplification of fluid flow through the gap between EVIE and the surface in 2D explaining lift force in the boundary layers

in pressure along x. From C to D, we have another wedge (mirror of the frontal wedge) leading to pressure of P_i at D. Since the pressure at any point of the body is at or above the ambient (inlet) pressure, there is a net positive lift force F_L

It is not certain that the above is the best way of explaining the lift- because the net force is a result of multiple effects. A qualitative way of understanding the lift phenomenon is to notice the boundary layers interaction at extremely small gaps leading to choking flow. There are theories exploring what is known as the near wall lift forces[56]. For small particles translating in a linear shear flow field near a infinite wall, a theory was proposed by Saffman for explaining inertial lift forces on them. The theory was constrained to only low Reynolds number flow and mainly for tiny particles. Cherukat and Mclaughlin later showed the application of the theory to rigid spheres and explained its validity for gap sizes smaller than the radius of the sphere [57]. However, the mathematical analysis for such a phenomenon, particularly for the shape of EVIE in the water while definitely worth pursuing, is more complex and beyond the scope of this research.

Note, in addition to the lift, there is an increase in the net drag due to the viscous friction between the boundary layers moving against each other in the gap.

4.3.2 Venturi Effect

In the region above the combined thickness of the boundary layers (consider the flow inviscid), still at a small gap from the surface, flow can be considered as coming into a pipe with a narrow neck, as shown in Figure(4-3). The diameter starts at h_1, reduces to h_2, and then expands back toh_1, From Bernoulli's equation, we know this would cause a increase in velocity in the narrow section, leading to a reduced pressure or a suction force F_v. This is also called the Venturi effect, widely used in race cars and can be expressed from Bernoulli's equation:

$$\Delta P = \rho/2(v_2^2 - v_1^2) \tag{4.4}$$

The boundary layers enhance the effect as the moving ground drags fluid into the gap (Couette flow).

4.3.3 Equilibrium

The two opposing forces described above vary in strength as the gap is varied, with the lift force fading faster than the Venturi force. In between the small distances with net lift, and larger distances a net suction, there is a balance point where the forces in z zero out. The Here, $F_L = F_v$. The total ground effect force at any instant is given by $F_g = F_v + F_L$.

4.3.4 Limitations

The description given here is very much simplified and the flow is way more complex. In reality there is no distinct transition between the flow regions, rather one dominates the other. Leakage (significant v_y) invalidate 2D modeling. The inclined plane assumes a very

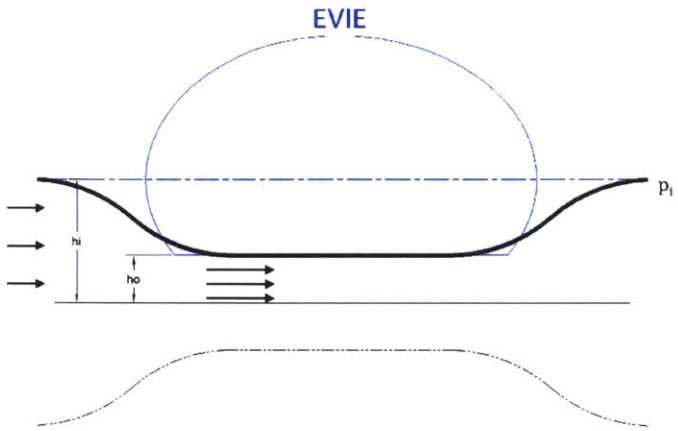

Figure 4-3: Simplification of fluid flow through the gap between EVIE and the surface in 2D explaining venturi suction

small angle, whereas the angle variation is much steeper for the robot. We also ignored vortices and wake fields at the trailing edge. Moreover, Bernoulli's principle is stated strictly for an inviscid flow whereas we work in a transitional domain.Hence, though the 2D modeling gives a qualitative explanation, a full flow characteristic is better understood through simulation.

4.4 Simulation

To explore how the fluid flow affect the robot, we simulated the flow around EVIE using standard CFX, the standard static CFD software from ANSYS[54] .For our robot moving at 0.5m/sec, the Reynolds number is $Re \sim 40,000$, based on which we chose the $k\varepsilon$ turbulent flow model. A fine (high density) mesh was used in the gap region; the remainder of the volume was meshed using standard, default settings. Mesh quality was tested by increasing mesh density until doubling the density (node count) resulted in $< 10\%$ change

in lift and drag forces. Buoyancy was not included.

From the simulation results we identified our three regimes:

1. $\varepsilon \leq 0.01$ as region (a) with positive lift force

2. $0.01 \leq \varepsilon \leq 0.3$ as region (b) with negative lift force

3. $\varepsilon \geq 0.3$, as region(c) where the effect of ground is no more pronounced

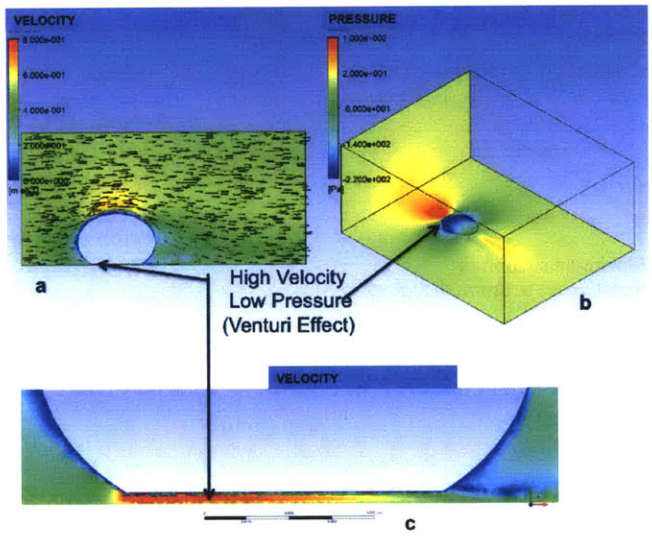

Figure 4-4: (a)Velocity(left) and (b) Pressure (right) distribution between the bottom of EVIE and the surface for u=0.5m/sec and h=5mm

Figure (4-5) shows the simulation result for the robot moving at a velocity of 0.5m/sec at various gap lengths. The curve characteristics look very similar to Figure4-1. Extremely close to the surface, below 2mm (region a) there is a lift force on the body. The body

stabilizes at 2mm, where all the forces balance. Above 2mm (region b) the Venturi force pulls the robot towards the ground. There is a second equilibrium point around 50mm, however this is unstable (positive slope). Above 50mm there is again a net lift force which extends out to large distances as the body smoothly transition to free stream behavior.

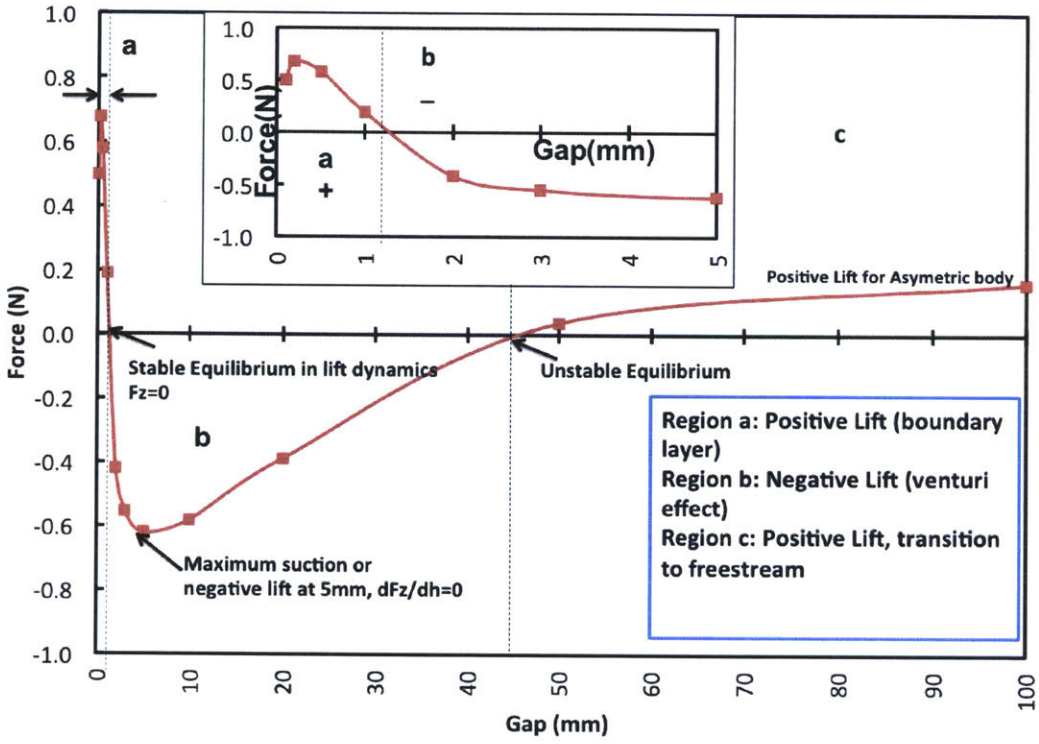

Figure 4-5: Shows the three regimes: (a) $h/c \leq 0.01$ (b) $0.01 \leq h/c \leq 0.3$ (c)$0.01 \leq h/c \leq 0.3$ and how F_z acts in each for EVIE moving longitudinally at 0.5m/sec

The transition from region (a) – $F_z > 0$ (lift) – to (b) – $F_z > 0$ (suction) – occurs near 2mm where $F_z = 0$. The negative slope at this point makes this a stable equilibrium: a positive z displacement results in $F_z < 0$ while a negative displacement results in $F_z > 0$, i.e. the robot is brought back to the $F_z = 0$ point. Whereas at the $F_z = 0$ point at $\sim$ 50mm, a positive z results in a positive F_z, pushing the robot even further away; and similarly for negative

z. The disappearance of the forces at 2mm, combined with a high gradient (high restoring force) is an exciting observation since this allows the body to be stabilized at such small gaps using hydrodynamics alone.

Figure (4-4) which is a simulation at 5mm, shows the flow and pressure patterns. The high velocity under the robot causes a drop in pressure. Note leakage of flow along y causes the flow velocity magnitude to die away fast before reaching the exit. This uneven flow and pressure distribution causes a higher pressure at the back than the front leading to a nose down pitching moment. Zero pitch can be achieved through design of the underbody as well as through active control through the pressure jets. However, for this chapter, we limit our discussion to the stabilization of F_z only.

Figure (4-6) shows the CFD simulations for runs at 1mm, 1.5mm, 2mm, 2.5mm, 5mm and 6.5 mm at velocities from 0.4m/sec to 1m/sec. The lift force are seen to go as v^2, as expected for turbulent flow. Drag forces (not shown) also vary as v^2. We can therefore use velocity-independent drag and lift coefficients in place of forces vs velocity.

$$C_L = \frac{2F_z}{\rho v^2 S_{xy}} \qquad C_D = \frac{2F_x}{\rho v^2 S_{yz}} \tag{4.5}$$

where: ρ is the density of water; area S_{xy} is the cross section at the horizontal midplane; and area S_{yz} is the cross section in the yz plane

$$S_{xy} = \frac{\pi}{4}ac \ , \ S_{yz} = \frac{\pi}{4}c^2 \tag{4.6}$$

with $c = 203.2$mm and $a = 152$mm.

4.5 Stability Analysis

Although the robot is stable at its equilibrium point, we need to consider the maximum perturbation in z that it can tolerate.

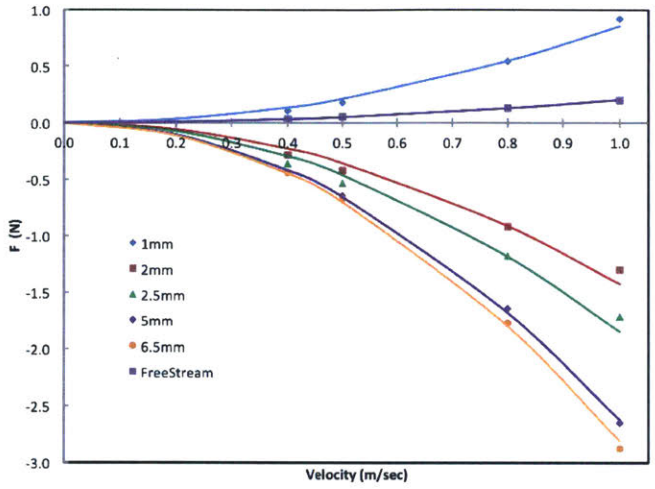

Figure 4-6: CFD Results for F_z at various gaps sizes and velocities ranging from 0.1m/sec to 1m/sec

The maximum upward force at 0.5m/sec is 0.65N compared to mass is 2.2kg for a force to mass ratio of $F/m = 0.3\text{m/s}^2$ or $0.03g$, where $g = 9.8\text{m/s}^2$ is gravitational acceleration. Since we wish to work near the point where lift force is zero, an equally important term is the restoring force, slope of force vs gap. At 1m/sec this is

$$\frac{dF_z}{dh} = -220\text{N/m} \tag{4.7}$$

Modeling this as a spring-mass system with $k = dF_z/dh$, we get a resonant frequency of

$$\omega = \sqrt{k/m} = 8.8\text{rad/sec} \leftrightarrow f = 1.4\text{Hz} \tag{4.8}$$

Therefore, at 0.5m/sec and a gap of 2mm, an external perturbation imparting kinetic energy $\frac{1}{2}mv_z^2$ will cause the robot to move by a distance h' where the potential energy $\frac{1}{2}kh'^2$ equals the imparted kinetic energy. In the absense of control jets, if

$$\frac{1}{2}mv_z^2 > \frac{1}{2}kh^2 \leftrightarrow |v_z| > \omega h \tag{4.9}$$

EVIE will touch bottom. For $h = 2$mm this is 0.018m/sec.

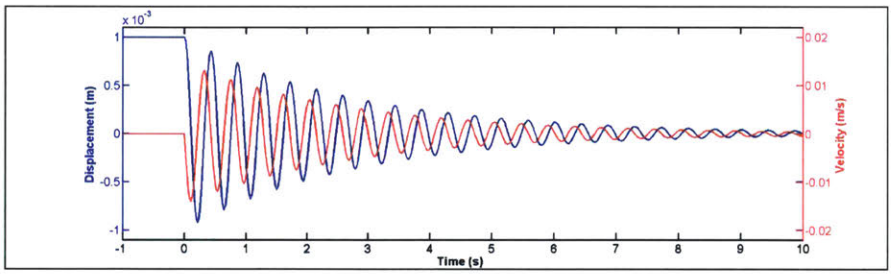

Figure 4-7: System response for a perturbation of 1mm from equilibrium

We consider next what happens as the size of EVIE is adjusted. For this, we scale all dimensions of EVIE by a constant of $\frac{1}{2}$ and 2 to compare with the standard ($1\times$) size. Figure 8 shows the force vs gap for velocity of 0.5m/sec. The gap, h, is expressed in terms of ε and force as the dimensionless lift coefficient (equation 4.5). We find C_L is a function of ε but nearly independent of size and velocity. Deviation at higher velocities and size may correspond to a transition from laminar to turbulent flow through the gap.

With this finding, we can consider we want a generalized expression if EVIE is scaled by a factor α while keeping the speed v_x and distance parameter ε constant. Let $\tilde{}$ indicate nominal ($\alpha = 1$) values.

$$\frac{F}{m} = \frac{1}{\alpha}\widetilde{\left(\frac{F}{m}\right)} \tag{4.10}$$

$$h = \alpha\tilde{h} \tag{4.11}$$

$$k = \alpha\tilde{k} \tag{4.12}$$

$$m = \alpha^3\tilde{m} \tag{4.13}$$

$$\omega = \frac{1}{\alpha}\tilde{\omega} \tag{4.14}$$

$$\omega h = \widetilde{\omega h} \tag{4.15}$$

Thus the force to mass ratio degrades as size increases. However, the maximum velocity perturbation, $|v_z| < \omega h$, is independent of size if the gap is scaled as well. Furthermore, the resonant frequency goes down for larger sizes, allowing more time for the control system to respond.

We note that the approximation used in the above conclusion breaks down as Reynolds number rises and flow transitions to turbulent through the gap. Up to $2\times$, we find forces and slopes increase with sizes, indicating higher stability for larger robots. We should strongly emphasize these results require the gap is scaled up as well: a $2\times$ EVIE is as or more stable at a 2mm gap compared to a $1\times$ EVIE at 1mm gap.

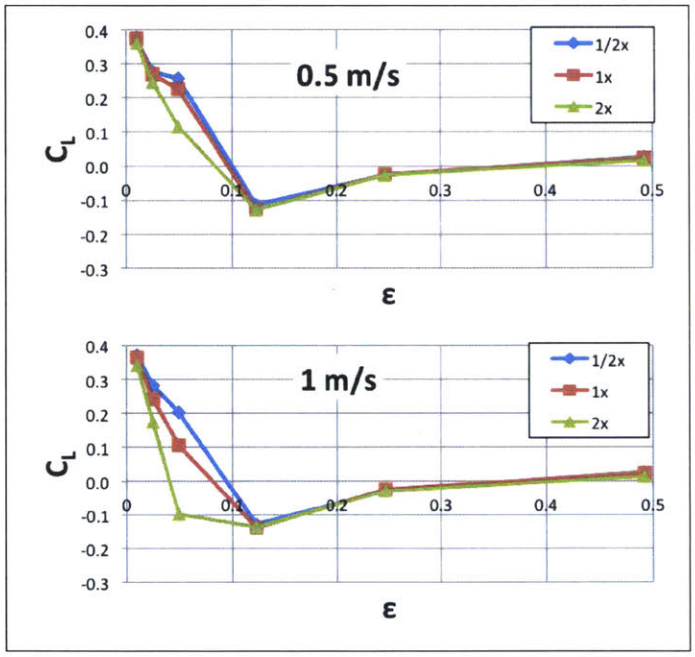

Figure 4-8: Lift coefficient for 0.5m/sec (top) and 1m/sec and for 1x, 2x, and 1/2x sizes of the robot. The curves shows the coefficient is mostly independent of size and velocity and strongly depends on the characteristic gap, $\varepsilon = h/c$

4.6 Experimental Results

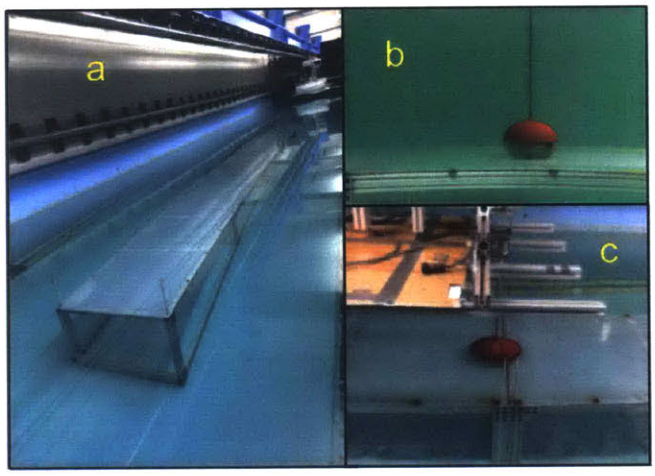

Figure 4-9: Experimental Setup at MIT's tow tank. (a) 16 ft long table (b) Robot moving at 2mm gap over the table (c) Suspension to the carriage

Preliminary experiments were carried out at MIT's 100ft long tow tank. The setup is shown in Figure (4-9). The experimental setup included a 16ft$\times$3ft polycarbonate table on an aluminum support frame with leveling capability along the edges. The biggest challenge was attaining sub-millimeter precision on the 16ft table standing on an uneven ground underwater to conduct the measurement. Simple things like temperature of the water could cause small fluctuations of the table elevation. Sub-millimeter shims were placed along the table length to get precision leveling. After an extensive effort a precision of 0.3mm was achieved across the length.

The robot was suspended with a hollow steel rod from a ATI force and torque sensor. We ran various tests at gaps of 1mm, 1.5mm, 2mm, 5mm and 6.5mm from the table, as well as in the free stream. Speeds varied from 0.1m/sec to 1m/sec, plus stationary. We analyzed both the drag and lift forces and compare with CFD.

Note matching experiment and simulation for fluid behavior in a boundary layer is extremely

challenging, particularly for a large set up like this. Hence, for our initial experiments, we focus more on qualitative behavior across different gaps than a quantitative match.

The robot was started several feet away from the table. After acceleration to the desired velocity, there remained a region of free stream travel. To reduce sensitivity to sensor errors, we consider only the difference in force between free stream and over the table, using the free stream data taken just prior to overlapping the table; thus the "ΔC_L". When comparing to simulation, free stream forces are subtracted for the CFD data as well.

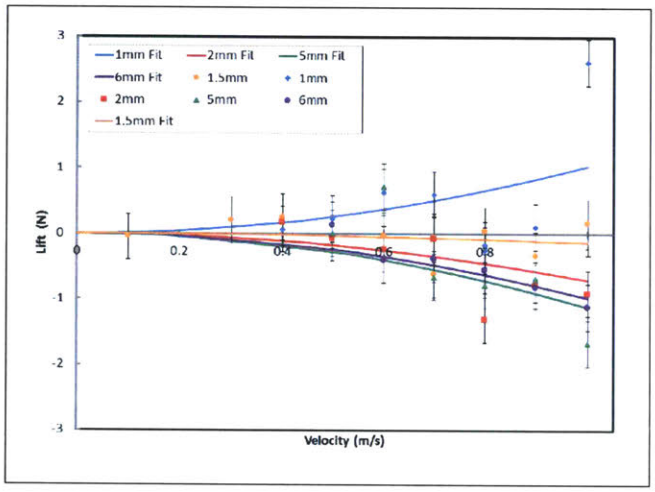

Figure 4-10: Experimental Data for lift force F_z from tow tank with error bars

Figure(4-10)shows data points from varying velocity and gap, overlaid with a quadratic fit for force versus velocity. Though there are several sources of error, for simplicity we consider only the dominant one: the sensor measurement accuracy. This is independent of velocity and gap. Therefore, a single error estimate was made by taking multiple runs with identical settings. This is shown as error bars on the 1mm gap data. To avoid clutter, error bar is not shown on the other data.

The most prominent feature is the lift at 1mm gap, particularly at 1m/sec velocity. Forces are quite small at 1.5mm for all velocities. Above 1.5mm, negative lift (Venturi effect)

occurs. Over 6mm, this negative force starts fading out.

Figure(4-11) shows the drag data (points) overlaid with a quadratic fit.

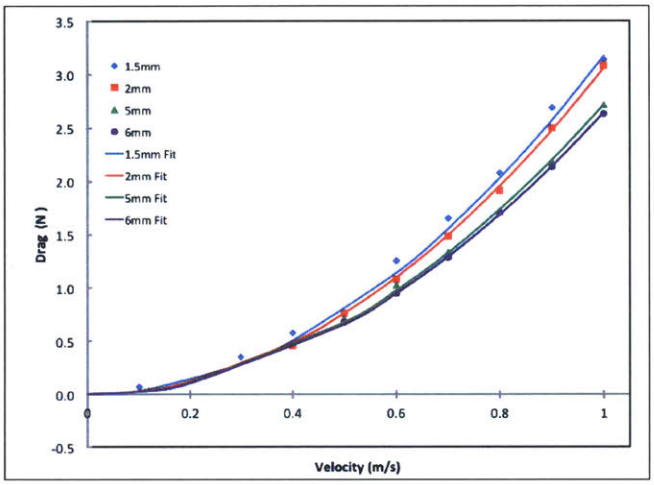

Figure 4-11: Experimental Data for drag force F_x from tow tank

We turn next to comparison with simulation. For this we use lift and drag coefficients taken from the quadratic fits to force versus velocity. In the Figure (4-12) and Figure (4-13) we overlay lift and drag coefficients from simulation and data. There is good qualitative match, with both exhibiting similar transition from lift at low gap and suction at high gap. There remains a 20% in quantitative match. The CFD simulations cannot completely imitate the experimental conditions, nor can the experiment reproduce the idealized condition assumed in the CFD. To set the scale for how serious this is, consider that a 10% change in velocity would give a 20% change in force. As we progress to more advanced design issues, we will look at improving the simulation, in particular whether applying the $k\varepsilon$ model throughout is appropriate. However, to the accuracy of the present apparatus, the agreement is excellent.

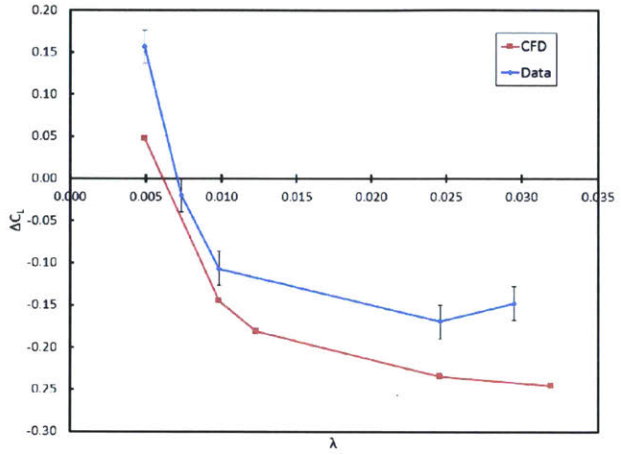

Figure 4-12: Comparisons of Lift Coefficients calculated from CFD and experimental data here

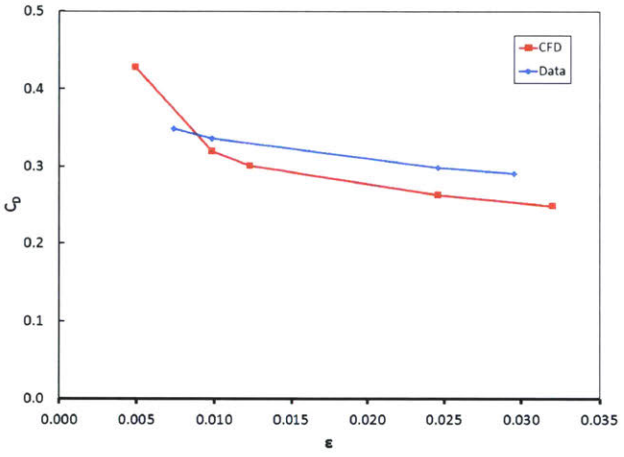

Figure 4-13: Comparison of Drag Coefficients calculated from CFD and experimental data

4.7 Design Effects

In this section we analyze how the variation of the underbody design affect the stability we have discussed so far. Thorough underbody design manipulation for faster acceleration is commonly seen in race cars. We make simple transitions from an ellipsoidal base to rectangular one and extend further with inclusion of protrusions on the base. The simple design translation explicitly demonstrate how flow dynamics and stability changes with minimal design variations and what parameters are of importance for achieving desired behaviors. The results are based mostly on simulations with the goal of using the same to decide on the correct experiments required to validate the observed phenomenons.

4.7.1 Simulation Setup

In this section we explain the simulation set up and the various runs will will perform. As before using ANSYS for simulation, we study the ground effect dynamics as we make simple transitional changes to the underbody design based on intuition and observation of the flow [58] The different designs of the bottom are shown in the Figure (4-14) and are described as

a) Elliptical base

b) Square with tapered edges

c) Elliptical front with rectangular sides and back edge with tapered edges Rectangular front and back

d) Item (b), with protrusion (two sizes tested) at the back

e) Item (c), with protrusion (two sizes tested) at the back

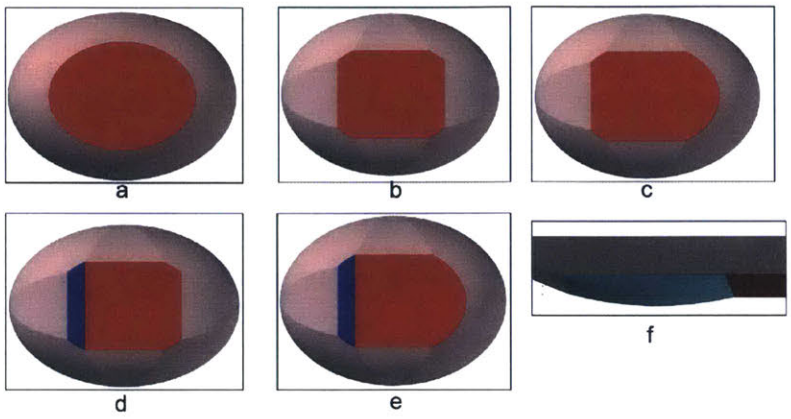

Figure 4-14: Different simple transitional designs of the base. Protrusion is shown sub-figure (f)

The explanation for the choices is done in details in the next section. But for simplicity, elliptical base comes from the original prototype. The first modification to a base with a rectangular back end, was motivated to capture more of the streamline flow along the direction of motion. We therefore borrow from race cars which typically uses a elliptical front and square back. We chose the dimensions of the rectangle to maximize the area while being (almost) contained within the original ellipse. The 3D model was then sliced by arcs to form the rectangular base. The arcs meet the rectangle and are tangent to the ellipsoid at the midplane; see Figure (4-15). For the elliptical front, only the sides and back are sliced, while for the rectangular front and back all four sides are sliced.

It is to be noted the base area changes through these operations. Design comparison via non-dimensional variables, which naturally would use this base area, is not pursued here since we are concerned with the overall performance and stability of the robot rather than exclusively the behavior of the base.

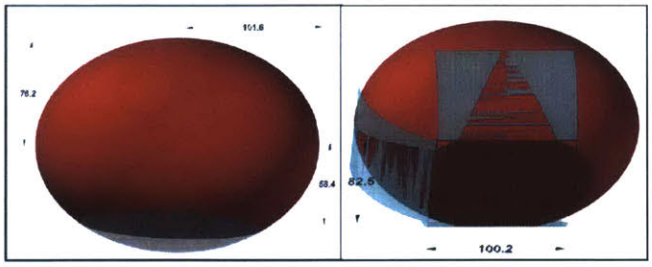

Figure 4-15: From perfect ellipsoid to a flat base and transitioning to a rectangular base

4.7.2 Simulation Results

Figure (4-16) shows the absolute lift, pitch and drag forces on the current vehicle as a function of gap lengths. As discussed in the section on forces and moments, at gaps far from surfaces, $\sim 20mm$ and above, considered as free stream, the body experiences an almost constant torque and lift. However, as one can see, in the near surface proximity the torque doesn't zero out as we vary gap.

This pitching moment on the body at a gap of 5mm can be for example explained easily by looking at the pressure distribution on the bottom surface as in Figure (4-4b). It is obvious the suction pressure at the frontal edge is much more greater than the posterior edge. The suction pressure is caused by the high velocity, and is termed as the Venturi effect. However the non uniformity of this effect can be contributed to the fact that the flow is not 2D and the elliptical base causes a flow loss due to dissipation from the sides. The velocity of the flow suffers considerable reduction at the back, leading to weaker Venturi suction. This pressure gradient between the front nose and the back edge causes a nose down pitching moment.

A more relevant plot is shown in Figure (4-18). Convention followed here is that counterclockwise torque and angles are taken as positive. It is seen that a stabilizing behavior is noticed between $3^\circ - 4^\circ$ (nose down). Beyond 4° the robot nose touches the bottom. We see that

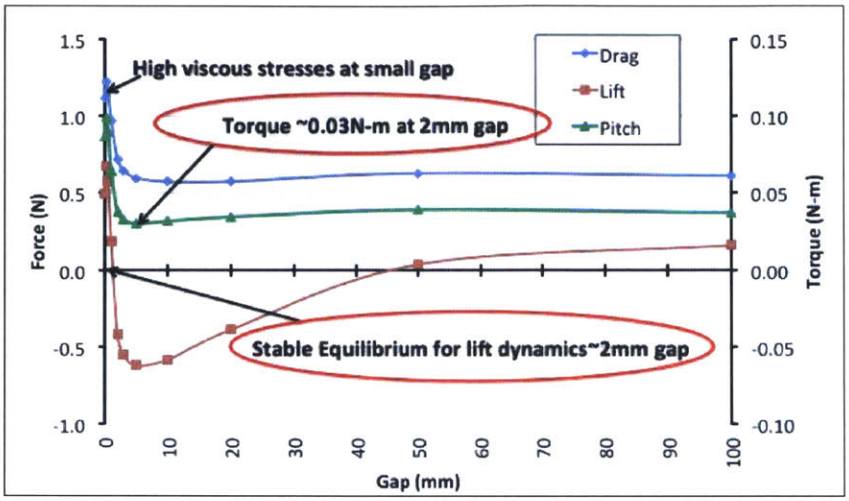

Figure 4-16: Gap versus lift, drag and pitching moment. Note the red line showing the lift dynamics has a stable equilibrium at 1mm, and the venturi suction to bring it back to equilibrium acts unto 5mm. The green line indicates a non zero for torque (nose down at 5mm). The blue line shows drag, which is higher when robot is closer to the ground.)

the slope of the curve in this region is negative- which means the body can be stabilized here. Note by stable, we mean a negative slope. The jets will be required to provide a constant torque to reach this condition, but perturbations are self-correcting. However, there is no stabilizing behavior in the nose-up orientation. Below 2° of nose down pitching, and for all nose up pitching angles, the slope is positive; thus a perturbation would not return to a stable point.

This brings us to understand what is the desirable characteristic we would like to see in the robot. Ideally, we would want the robot base to be parallel to the inspection surface. Of course sensor can be made parallel in other ways as well, but the simplest and ideal design would be to achieve a zero torque at a zero pitching angle. Intuitively that means the pressure distribution should be entirely uniform across the base or the variation at the front and back edge should somehow nullify each other resulting in a zero torque at zero

pitching moment.

To explore if this is achievable we made simple transitional design changes to the robot's base. First we went from an elliptical base to a partially rectangular base to get more uniform flow as in Figure (4-14), as with a race car. This turned out not to have much improvement besides a reduction in drag due to the reduction of the base area. For completeness we simulated a symmetrical base, with rectangular front and back . The result to note here is there is no stabilizing behavior in either nose down or nose up as seen in Figure (4-19). Note, some random scatter points from CFD has not been excluded.

Next, inspired again by underbody design in race cars to manipulate pressure distribution, we added a bump or protrusion toward the rear of the robot, shown in in Figure (4-14 -d,e, f). The reduced cross section results in a high velocity region in the back to balance the one in the front and is mostly analogous the flow through a pipe with varying cross section (except there is mass dissipation).

Since drag is less with rectangular sides and back, and fully rectangular, we introduced protrusions in these two designs. A 1mm bump had little effect, but increasing the protrusion to 2mm height revealed unique results seen in the Figure (4-19) . For the square base, the protrusion creates a stabilizing region between -3° and -4°, but no stabilizing region for a nose down pitching moment. The protrusion for the elliptical rectangular sides and back led to a somewhat symmetric stabilizing behavior for nose up and nose down orientation. The restoring torque in nose up orientation is weaker than for the nose down, and we do not achieve stability at zero pitch. However, the negative-slope region at $+3^\circ$ to $+4^\circ$ can be utilized. A robot traveling at nominally zero pitch, if perturbed, may experience uncontrolled motion up to $\pm 3^\circ$to $\pm\ 4^\circ$; but at that point it can stabilized.

The ideal condition - zero torque at zero pitch, and negative slope for torque versus pitch at zero pitch - maybe be possible with a protrusion design and placement not studied in this chapter. However, the basic stabilization mechanism can be understood from this

study. When the robot is around 4° nose down, it is essentially in the region (a) where the front nose experiences a lift force trying to cause the robot to nose up. When the robot is perturbed such that it's nose is 2.5 mm above, it is in region (b) where Venturi suction takes place pulling the nose back down. The rear perturbation creates a similar phenomenon in the back for nose-up pitch.A nose down orientation under CFD simulation condition is shown in Figure (4-17).

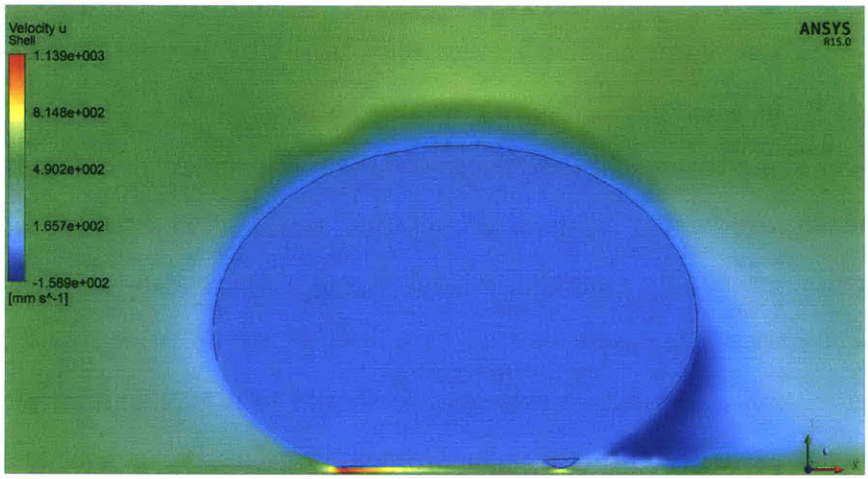

Figure 4-17: Flow behavior (velocity profile shown) around a nosedown orientation of robot

Finally we look briefly at lift and drag characteristics as in Figure (4-20) and Figure (4-21).The square base was observed to have the lowest shear drag, whereas the protrusion has the maximum drag force. A stronger propulsion system could overcome the increased drag forces. However, we intend to first explore smoothing the transition from the flat region to the protrusion to reduce drag. Stability in lift dynamics occurs for all designs in the same sense as for torque and pitch: The lift force is not zero, but has a negative gradient with gap. With a steady force from the jets, a perturbation that moves the robot

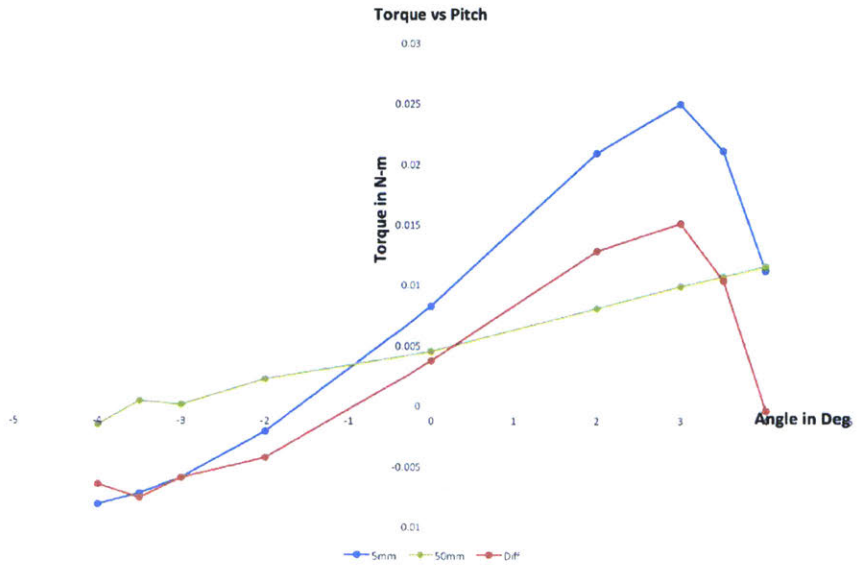

Figure 4-18: Pitch vs. Torque for elliptical base. Red plot shows the difference between the free stream and the ground effect. Green is free stream behavior, and blue is the behavior in the proximity of ground

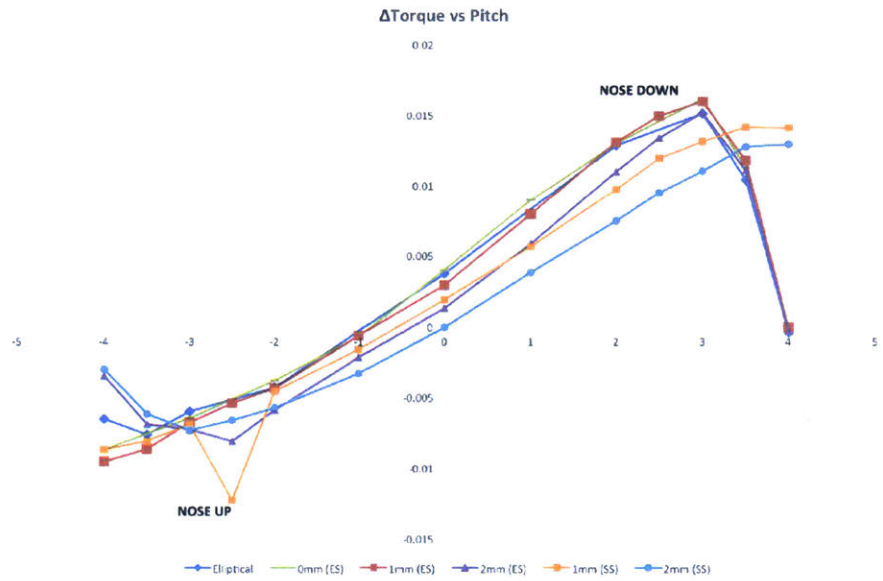

Figure 4-19: Pitch and Torque comparison for all kinds of bases. Note purple plot -with elliptical front, rectangular sides and back, and a 2mm protrusion have a negative slope indicating stabilizable behavior in both nose up and nose down orientation.

closer (farther) to the surface results in less (more) suction from ground effect and the robot moves back to its nominal position. We note the design with the best pitch stability rectangular sides and back, 2mm protrusion has the weakest restoring force.

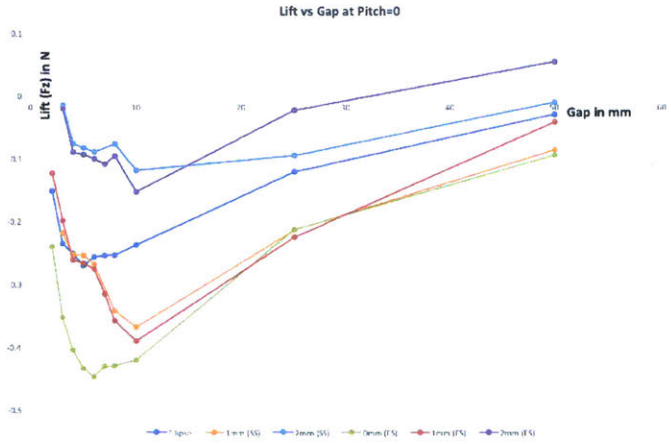

Figure 4-20: Lift versus gap for various base designs. Note the one optimal for pitch stability, that is the elliptical front with square sides, and protrusion - doesn't give the best lift stability characteristics (purple plot). The elliptical base with square sides and minimal protrusion of 1 mm (red), or the symmetric square base (green) performs the best though they are not really optimal for pitch stability

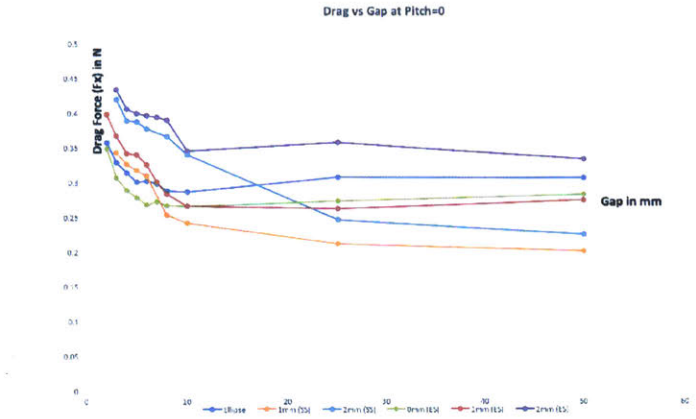

Figure 4-21: Drag versus Gap for various base designs. Square base was observed to have the lowest shear drag, whereas the protrusion has the maximum drag force.

4.8 Conclusion

Ultrasound and eddy currents are widely used for subsurface inspection of underwater structures. Currently, robotic testing requires the robot be in contact with the surface to be tested. Particularly on a rough surface, contact reduces the speed with which such inspections can be performed, which in turn limits the applicability of these techniques. For instance, it is not currently possible to examine a large number of boats and ships in a port for threat detection in a practical way. Having low cost small untethered vehicles, like EVIE that can perform fast scans would be an ideal solution.

This chapter described a novel method to stabilize our micro UUV EVIE using hydrodynamic forces to maintain a small, precise gap. Combining the lift force from choking flow at extremely small gap with the Venturi suction a stable equilibrium point is achieved at few millimeters height which allows the robot to move on a fluid bed created by natural hydrodynamics. This enables faster movement on rough surfaces. Analogies of this phenomenon has been discussed and behavioral similarity has been found with that of hard

disk drives which occurs at micrometer and milligram scale. Although the fluid dynamics is quite different, we have demonstrated a similar self-stabilization phenomenon in water at the scale of millimeters and kilograms.

Hydrodynamic simulation of the concept has been presented and compared with initial experimental results for longitudinal motion. The process have been evaluated for different parameters, and a stability analysis was performed. Note, effect in turbulent flow was not studied and only calm water is considered. It is obvious for practical practical applications relying solely on natural hydrodynamics will not be adequate, and we might need a more active method of controlling the fluid bed height. Though initial research showed the possibility of stability in lift dynamics, stabilizing pitching moment was not intuitively expected. Further simulations brought forward new insights and possibilities in design optimization utilizing near surface stabilizing phenomenon. A specific option is a mostly flat rectangular base but with a bump (protrusion) near the rear; this was shown to achieve a degree of stability not possible with active controls alone. Zero torque at zero pitch angle has not been yet achieved, but stabilizing behavior in both nose up and nose down orientation of the robot confirms the existence of a geometry to satisfy this ideal orientation. Further work is needed to optimize the design for reduced drag and a narrower window of pitch. However, for our research we shall use the preliminary design (flat base) in the upcoming chapter to demonstrate ground effect and how to integrate the same with vehicle dynamics.

Chapter 5

Jet Induced Hydrodynamic Ground Effect

5.1 Introduction

In the previous chapter we discussed the phenomenon of the natural hydrodynamic ground effect (passive hydrodynamics). We found that to truly exploit the phenomenon in real applications, we need to have some level of active control on utilizing this resultant non linear force for the purpose of near surface maneuvering. This means we might want to actively change the stabilization height or thickness of the fluid bed. It could also mean detecting the nature of the surface based on the resultant non linear force experienced by the body. For example ground effect force experienced on a rough surface would be different than on a perfectly smooth surface. Active control would be essential in real environments where water is not entirely calm and some level of turbulence would be existing. In this chapter we explore and analyze an active control via the use of a single bottom jet that enables hovering and sliding over underwater surfaces. By sliding, we mean smooth motion using a fluid bed layer. And hovering implies reduced thrust near surface motion (few body lengths) over a region of interest. Such motion has applications to both visual and volumetric ("on contact") inspection methods of underwater surfaces: pipelines,

oil rig infrastructure, ships, or even fore stealth detection of threats like underwater mines. Examples of applications that uses similar methods of using fluids for enabling smooth motion are air hockey, where disks move on a film of air (sliding); and hovercraft which uses a air-cushion at a higher pressure than ambient contained within what is called a "skirt". And, then there is vertical/short takeoff and landing (V/STOL) vehicles which experiences additional thrust (upwash) in proximity to the ground. The common feature is using the fluid between the body and an external surface to generate forces. The phenomenon though widely known in the context of motion over land and water surface, with air as the fluid, but has not been utilized for underwater motion. In our research we exploit the fluid flow between a submerged surface and a robot with a single active thrust jet coming out of the bottom. A lot of work has been done on single and double jets impinging on the ground for V/STOL, particularly for NASA, but no analogous studies exist on how a water jet affects the dynamics of an underwater drone moving near submerged surfaces. Results from simulations and initial experiments show unique phenomena of multiple equilibria points at various heights from the ground. For a fixed thrust force we demonstrate two stable regions: in extremely close proximity, when the robot rests on a thin fluid film which enables it to glide; and another with the robot a body length or more away. Stability at close proximity is relevant to volumetric inspection methods such as ultrasonic testing. A larger gap has application in visual imaging, where an additional upward force (upwash effect) due to the impinging jet allows the robot to hover at fixed distances from the target surface at reduced thrust. The upwash effect is more prominent for multiple impinging jets. We explain the observation and understanding of the jet impingement phenomenon through CFD simulations and experimental data and discuss exploiting this effect for practical application using micro UUVs like EVIE. In an actual inspection mission, passive and active ground effect will be coupled to give the combined force and determine the thickness of the fluid bed layer. The modeling of the coupling of

the vertical and horizontal motion is beyond the scope of the current research.

5.2 Literature Review

In the previous chapter we investigated ground effects from longitudinal motion. Results are summarized in Force vs. Ground Effect curve - a strong negative (suction) force is seen at small gaps (less than half the body length). This results in a stable equilibrium at $\approx 2mm$ and therefore a formation of a thin layer of fluid bed on which the body can glide smoothly. But as discussed, fluid bed created by passive hydrodynamic effects might not be sufficient for actual applications. In this chapter we extend the work to explore an impinging jet to create a controlled fluid bed layer. Constraining the robot to motion only in z, we study how the ground effect created by the impinging jet influences the net z force and the resultant vertical motion of the body. We find similar force vs distance behavior at small gaps behavioral curve, but also a new phenomenon at larger gaps suitable for hovering under reduced thrust.

There are a few analogies to this model which are worth discussing. For the first stable point, at small gaps ($h/c << 1$) a good analogy is the hydrostatic bearing where an external pressure supply (pump) is used to continuously force the fluid through an orifice to create a lubrication film. More broadly speaking, from theoretical analysis perspective this is perhaps best understood from the concept of incompressible radial flow between two parallel plates through a center inlet. The effect seen due to the flow in the gap, in terms of real world applications, can be compared to VTOL vehicles.

We notice, if EVIE is made negatively buoyant, it will attain equilibrium in free-stream at an optimal jet thrust (created by the bottom jet), F_{opt}, which cancels out the net weight under water. For any thrust force $F_T < F_{\text{opt}}$ the body will sink. In our experiments using a negatively buoyant system with a single bottom impinging jet, we find that as we lower

the thrust force, the body begins to sink towards the ground as expected, but then stabilizes at a new point - close to the ground ($\sim$ one body length) even though the thrust force is slightly lesser than needed to balance the body's weight. This was observed to be even more prominent when two impinging jets were used. As we lower the jet force further, the body sinks to a new equilibrium further closer to the ground. This is due to an 'upwash' effect which creates an additional thrust from the interaction of the impinging bottom jet(s) with the floor. The characteristic force curve due to impinging jet can be related to that seen in a vertical take off and landing vehicle with a single jet impinging on the ground [62]- however, at a very different Reynolds number. In a VTOL, the impinging thrust force creates suction pressure at close proximity and added lift at a further distance away. In our research, we demonstrate these behaviors through simple experiments and analyze them using CFD simulations. Complex analytical modeling of such flows have been done for fluid flow in parallel plates and ground effects on VTOL flights, but is beyond the scope of the chapter. Our use of CFD is primarily for visualization as a means of achieving a more intuitive understanding of the velocity and pressure distributions in our experimental domain. The "F_g vs. H" Curve for the jet impinging robot is shown in Figure (5-1) - and it is similar in characteristics and shape to that obtained due to longitudinal motion and natural hydrodynamic effects shown in Figure (4-5) .

5.3 Basic Design

The basic design has been explained in Chapter 2. Different experiments were performed to understand the impinging jet effect. The prototype of EVIE was used with a single 5mm diameter cylindrical nozzle centered at the bottom. A simple centrifugal pump powered at 0-12V is mounted inside and the flow passes through a short (15mm) tube to the nozzle. The pump effective working region is 3-12V with a maximum heard pressure of 60kPa at

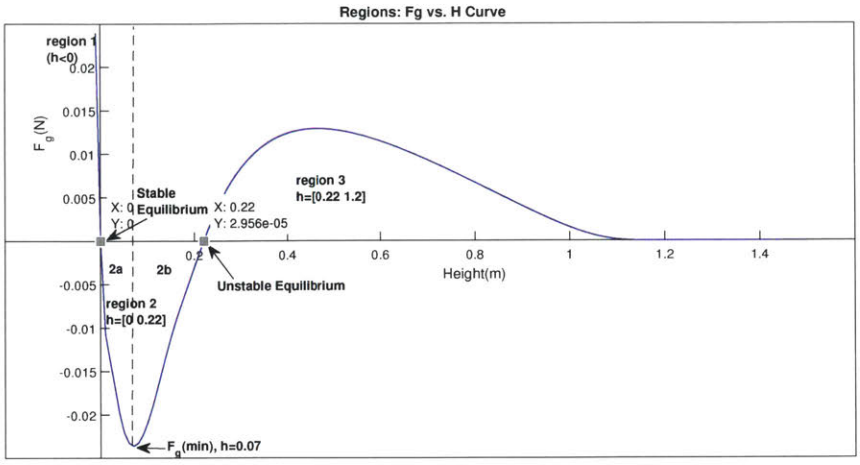

Figure 5-1: Hydrodynamic Force F_g caused by a single jet from the center bottom of the robot impinging the ground

12V. In free stream the jet can produces thrust between 0.0007N (at 3V) and $\sim$ 0.036N (at 12V). Our robot has a net submersed weight of 3gf (gram force) or .03N.

Thus there is a unique setting where with jet thrust exactly balances weight: $F_T = F_{\text{opt}}$, the equilibrium condition for depths far from a surface. Small increase in thrust jet and the robot rises; small decrease and it sinks.

The presence of a surface alters the flow pattern and forces. Our analysis, confirmed by experiment, show two stable equilibrium points for a given thrust force. The first one at close ground proximity and the other at a further distance from the surface which can be varied by the jet setting. There is also one unstable equilibrium point which is of lesser interest.

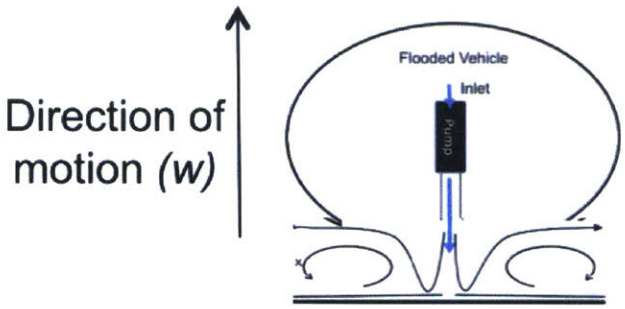

Figure 5-2: Block schematic showing a single bottom jet robot

5.4 Theory

As shown in Fig 5-5, the jet flow through the bottom creates three different regions of interest which are dominated by three different kind of fluid flow. For understanding the effect of the flow near the ground, the key parameters to consider are: the ratio of the height from the ground to the UUV's characteristic length, $\varepsilon = h/D$, where h is the height, and D is the characteristic body length (diameter of the bottom); the ratio of the gap to nozzle size,$\eta = h/d$, where d is the nozzle diameter, the ratio of the volume flow to νh where ν is the kinetic viscosity of water . The three regions of interest are described as below and shown in the Fig :

- Region 1, Pressure Build Up. When the robot's flat bottom is in contact with the surface, the thrust jet results in pressure building up to lift the body and releasing the flow by creating a thin fluid bed. The radial flow here is laminar in nature unless the Reynolds number is very high at the nozzle exit.

- Region 2, Ground Effect Induced Lift Loss. At gaps past Region 1, the primary jet creates what is called the "wall jets" – flows parallel to the surfaces – radiating

outward and creating a low pressure region under the body, resulting in a strong suckdown.

- Region 3, Upwash. At larger gaps the impinging jet can interact with its flow along the wall (wall jet) creating an upwash effect that leads to an additional positive lift. This is prominent when there is multiple impinging bottom jets, where the upwash results from a phenomenon known as the fountain effect. The upwash effect is suppressed at close proximity to the ground as the flow shifts to radial.

5.4.1 Region 1

Region (1) is dominated by "pressure build up" inside the nozzle. When in contact with the wall, the flow is blocked by the surface obstruction. At a particular pressure for a given opening size, the built up pressure at the nozzle exit p_1 leads to a pressure differential with that at the outer edge of the body p_2 (ambient) leading to a radial flow. The flow underneath the body creates sufficient force in Z to lift the body by a height h_0 resulting in a radial flow between the body and the wall. This flow at very small gaps is laminar in nature, and the analytical model for representing the same is similar to that of a hydrostatic bearing. A pressure drop in the radial direction due to shear stress may be observed. For extreme small distances in this region, inertia and turbulent terms are neglected and this kind of flow can be modeled as a laminar flow. The governing equations and principles are based on Navier-Stoke equations for radial flow between parallel plates and for low Reynolds number can be found [51], [52].

$$\rho u \frac{\partial u}{\partial r} = -[\frac{\partial p}{\partial r}] + \mu[\frac{\partial d^2}{\partial y^2}] \tag{5.1}$$

$$\frac{\partial (ru)}{\partial r} = 0 \text{ continuity} \tag{5.2}$$

If the exit jet from the nozzle is extremely high, the flow underneath in the gap could be entirely turbulent in nature.

5.4.2 Region 2

Though at close proximity to the ground one might expect additional lift when thinking in terms of an aircraft, in this particular configuration, the reverse is witnessed. It has been found negative pressure and strong suckdown (negative lift) forces dominate as h/D increases. The suckdown at small η can be understood as the jets entraining and accelerating fluid beneath the body, resulting in reduced pressure. This is clearly seen in the simulation section through flow visualizations. The phenomenon was studied extensively in fluid dynamics, and in the context of VTOLs by Stewart and Kuhn (1983) [64] where single jet impingement induced lift loss is a matter of concern. The VTOL studies points out $\eta = h/D$ – the ratio of the proximity to the ground (h) , the nozzle diameter (D) and the flow volume Q/vh as some of the the key parameters.

An active jet of water impinging on a submerged ground surface affects the net lift force on the body. The flow now transitions to the turbulent regime.For $\eta \lesssim 0.3$ outward flow remains attached to the body leading to small ground vortices in the gap. The strength of the ground vortices decreases with increased height; at a limiting height h_v the ground vortex disappears and the pressure goes to zero. VTOL studies identified the nozzle pressure ratio (NPR) – the ratio between the jet stagnation pressure and the ambient pressure – as another important parameter. The NPR gives the jet thrust and flow rate relationships. Other parameters that affect induced lift (positive or negative) are jet structure, jet impingement angle to the ground, shape of the outer edge of the model, ground plane size relative to the model, as well as the size of the test chamber and obstructions above or near the model [63]. Effects of these additional parameters should be done in future research.

5.4.3 Region 3

Impinging jets can also lead to a positive lift from upwash effect: jets rising upward after striking the ground. The fountain upwash, is more commonly invoked for multi jets, though additional positive lift may also observed in single jets, perhaps due to interaction with the wall jets (cross flow). Stewart and Kuhn [64] found that for direct thrust circular jet configuration like in our model, ground effect initially induces a favorable (increased) lift out that increases rapidly as the body approaches the ground. However, closer to the ground and for low velocity, the fountain upwash overcame by the suckdown. The upwash effect does reduce some of induced lift loses from the suckdown at the transitional region. Lift losses for VTOLs is a complex phenomenon and has been studied in various research. In Figure 5-3 [65] the percentage lift loss with height from ground is plotted. Note the other common term used is the out of ground effect lift loss, which we won't explore as such in this chapter. The basic equations used to describe the net jet induced lift loses $\Delta L/T$ in the proximity of the ground can be given as:

$$\frac{\Delta L}{T} = \left[\frac{\Delta L}{T}\right]_s + \left[\frac{\Delta L}{T}\right]_f \tag{5.3}$$

where $[\Delta L/T]_s$ is the lift loss due to suckdown and $[\Delta L/T]_f$ is the lift increment due to fountain effect, with lift (L) normalized to thrust force (T).

5.5 F_g Model

In our research so far, we have demonstrated and analyzed the hydrodynamic ground effect phenomenon - the different force regions- and their implications mainly through experiments and simulation. We have observed the effects of changing parameters like size or area of the body or noted how the flow changes by varying the underbody design

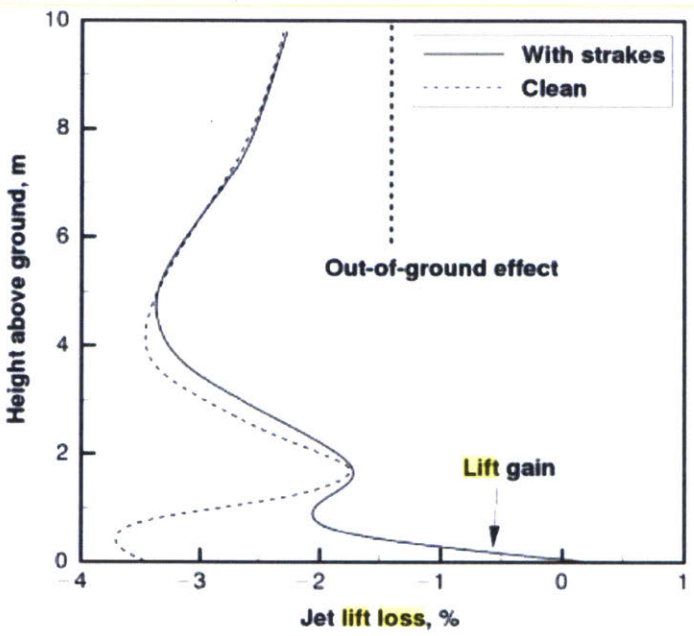

Figure 5-3: This graph by Antonio Filippone [61] shows ground induced lift loses for fixed and rotary wing aircrafts with varying heights from ground. As one can see the region 2 of maximum loss occurs at pretty close proximity to the ground (4m), and then is compensated somewhat by a positive lift force, likely from fountain effect. The out of ground effect lift loss is also shown as a constant.

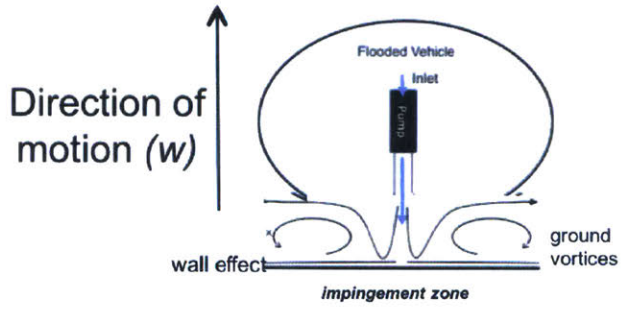

Figure 5-4: A block schematic showing the different effects of the ground. The wall jets, ground vortex and fountain upwash phenomenon are shown here that leads to negative or positive lif

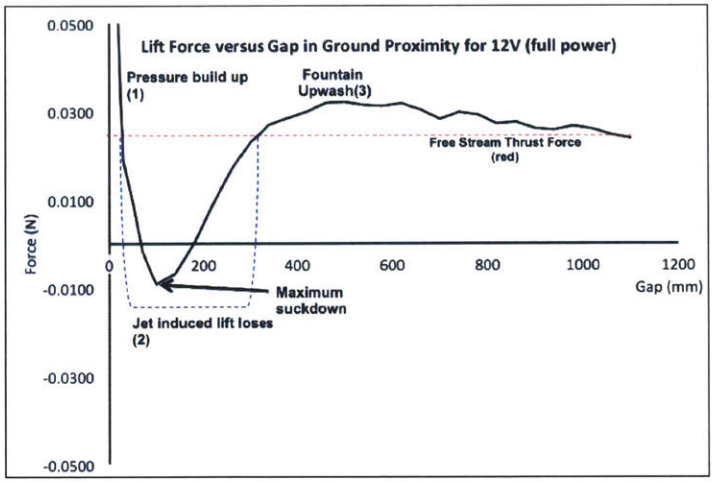

Figure 5-5: This is the general lift force trend found for our underwater robot. We broadly divided into 3 regions, (1) Pressure build up and leading to a large lift force (2) Suckdown or jet induced lift loss region (3) Fountain upwash or positive lift region. Note for low velocities the suckdown extends beyond the upwash.

[59]. In this chapter, now take a deeper dive into modeling the system -particularly keeping in mind the need for an onboard control system. Some of the parameters taken into account for the modeling should be the characteristic gap, size and scale of the object, the height from the ground, the flow rate, velocity of the body, surface roughness among others.

From previous research presented, it was shown that the non dimensional lift force is dependent solely on the characteristic height, that is $\varepsilon = h/c$ where h is the height from the ground and c is the chord length of the body. It is observed that the ground force can be represented as a function of height and the thrust force F_T. The thrust force F_T goes quadratically as the velocity of the jet w_j as well as the pump control voltage V (direct control variable). That is,

$$F_g = f(h)f(V) = f(h)f(F_T) = f(h)f(w_j) \tag{5.4}$$

We know, the F_T can be represented as-

$$F_T = \dot{m}_e w_e - \dot{m}_o w_o + (p_e - p_o)A_e \tag{5.5}$$

where $\dot{m}$ is the mass flow rate, and subscript e and o denote parameters at entrance and outlet of the nozzle. Again, the mass flow rate which is related to velocity as

$$w = \frac{\dot{m}}{\rho A} \tag{5.6}$$

The CFD data of F_g overlays perfectly as we scale by $\frac{1}{V^2} \simeq \frac{1}{w_j^2}$ - taking away the dependency on flowrate (or voltage or velocity). So, the height dependency is given by the curve shown. We can say that,

$$F_g = f(F_T)f(h) = q^2 f(h) \tag{5.7}$$

The curve in Figure (5-6) shows $F_g(h) = 1/q^2 F(g)$- which gives us a clear idea of how the force depends on the height at a given F_T and - as expected -is highly non linear. The overlaying of the experimental data was not that clean since there are many other real parameters that affected the experiment came into play. This is seen in the Figure 5-7. Although it doesn't overlay, the force is scaled down to a factor of $\approx$10. The result could still be used for an initial estimation for F_g when applying an estimation theory for determining F_g.

5.6 Simulation Results

Since lubrication theory is relatively well understood, for simulation we restrict ourselves to a turbulent flow model emulating the VTOL in an underwater environment. The model is set up using CFX, the standard static CFD software from ANSYS[54]. Turbulence is

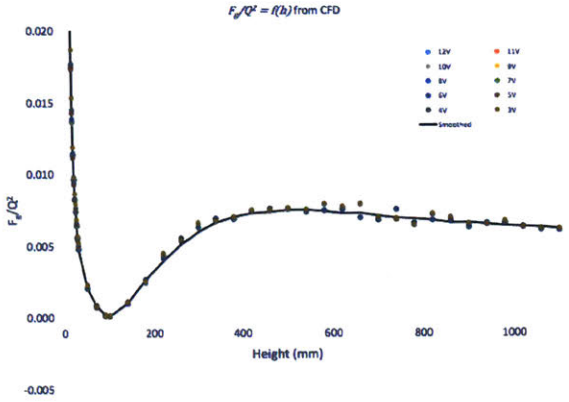

Figure 5-6: CFD F_g data scaled by $1/{w_j}^2$.

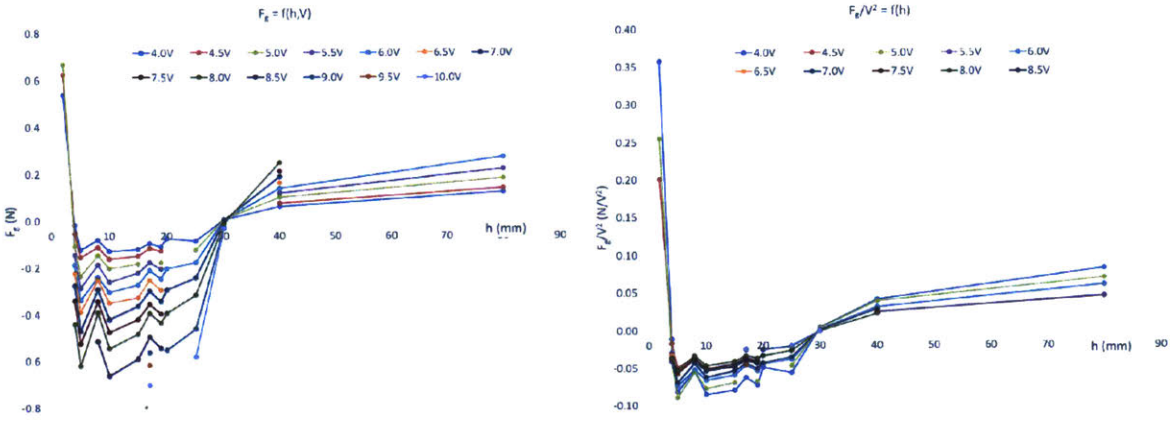

Figure 5-7: Left: Shows the experimental F_g for all different voltages Right : Shows $F_g/f(V)$ to see the sole effect of distance. Unlike the CFD results, the curves do not overlay due to unaccounted factors in the experiment.

handled by the $k-\varepsilon$ model. The mesh was generated using "Proximity and Curvature" for the advanced size function, resulting in a dense mesh around the robot bottom, particularly when close to a surface. The pump is represented by an inlet at the top of a pipe, with the inlet flow rate set to match the measured properties of the pump.

Figure 5-8 shows the the suckdown phenomenon for a flow rate corresponding to full power (12V) at gap size 100mm and 20mm respectively. We see the expected downward flow under the body; and, for small gaps, a low pressure region underneath the body formed by the ground vortex. The plots are in logarithmic scale to cover the large range of velocity and pressure.

Figure 5-9 shows how lift force varies with gap heights for different inlet pressures. Recall the stable condition

$$W = T + [\Delta L]_f + [\Delta L]_s \tag{5.8}$$

As described above, at small gaps the suckdown or negative lift L_s, is strong compared to the positive lift due to fountain upwash, L_f, and there is reduced lift or even a net downward force. However for a single jet L_s drops rapidly with distance, L_f less rapidly, resulting in an enhanced lift for larger gaps. As the gap is made still larger, this lift enhancement also fades. Thus we get two stable conditions. First, very small gaps: the suckdown pulls the robot to the surface. (Note actual contact does not occur, but the thin-film regime is not properly modeled.) Second, thrust plus upwash, minus a weakened suckdown, balances the weight of the robot. Upward perturbation of distance decreases L_f contribution, while downward perturbation increases L_f; thus this is a stable equilibrium. Note Figure 5-9 includes a correction for varying cable length (for pump power) immersed in the water. The rigidity of the cable is however not included in our model. Thus, although we have qualitative agreement with our measurement – a stable equilibrium at a distance which varies with pump power – we do not have (and cannot expect) quantitative

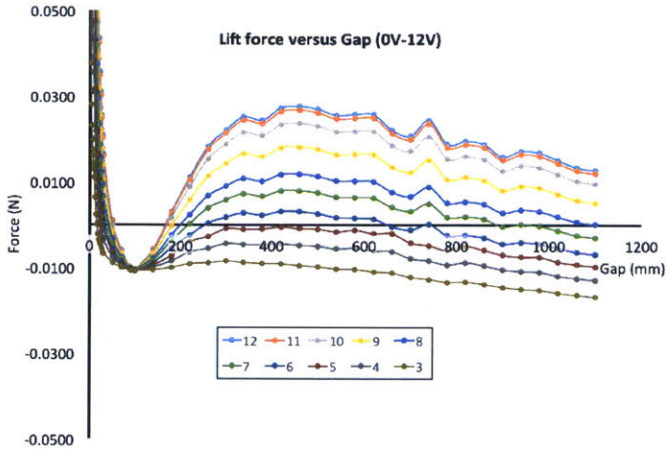

Figure 5-9: Lift force versus gap heights as the pump voltage is varied (therefore the flow rates) for a negatively buoyant robot with a net weight underwater =.03N

and turbulent flow at the larger gaps. For really understanding the flow in the channel- that is the bottom of the robot and the floor- we use just a elliptical plate with a center hole and an impinging jet.

For our studies with a vertical jet and a stationary robot (representing a hovering vehicle), we use the gap between the body and the floor as the characteristic distance. We recognize this is valid only if the gap is small compared to the body size; the Re at large gaps cannot be taken seriously and are not included in our Reynolds number plots.

For velocity, we use the average at the outer edge of the plate. This is simply Q/A where A is the exit area and Q is the volumetric flow rate. Using $A = h\chi$, where χ is the plate circumference and hA is the gap, we get

$$Re = \frac{Qh}{\nu A} = \frac{Q}{\nu \chi} \tag{5.9}$$

The results for the small gap region (which is of most interest to us) upto $50mm$ using the above model is shown as below, which has a better match to small gap experimental

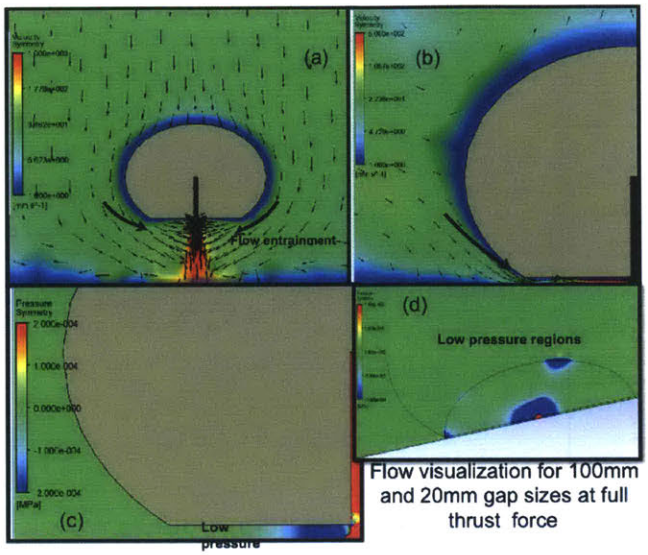

Figure 5-8: Flow visualizations demonstrating lift reduction or suckdown phenomenon. (a) Flow entrainment at 100mm, and full power thrust (b) Flow entrainment at 20mm gap height(c) Pressure distribution at 20mm across the gap (d) Pressure distribution showing low pressure on the bottom surface of the robot

agreement on the stable distance and corresponding voltage.

The upwash can be made more clear by understanding the difference of flow between the free stream and a closed bottom. This is shown in the Figure 5-10. This is done at a gap height of 300mm. As one can see the upwash, which then changes direction and escapes out of the edges of the undersurfaces giving rise to the additional lift. The large reflection (red arrow) colinear with the jet is an artifact of the very high velocity associated with the jet, and a slight broadening of the jet in the presence of a surface. The combination results in a very large Δv at the core of the jet.

We found the $k-\varepsilon$ model gave a good behavioral match to our observation, from a quantitative perspective for predicting the stable equilibrium it was quite off. We therefore redid the model by using the $k-\omega$ SST model to capture the laminar flow at small gaps

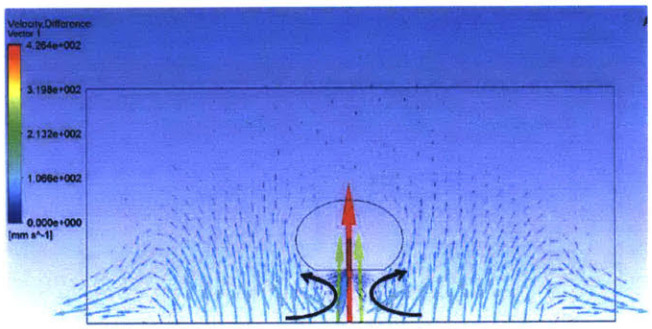

Figure 5-10: Flow visualization for Lift Increment due to Fountain upwash

results.

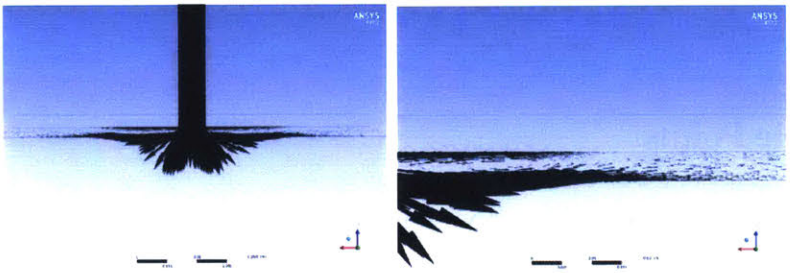

Figure 5-11: Flow in the jet impinging channel- that is between the bottom of the robot and the ground

5.7 Experimental set up

Two types of experiments were performed. First, we address whether the robot has multiple stable points as predicted by CFD. After confirming the CFD prediction, we proceeded to measuring forces.

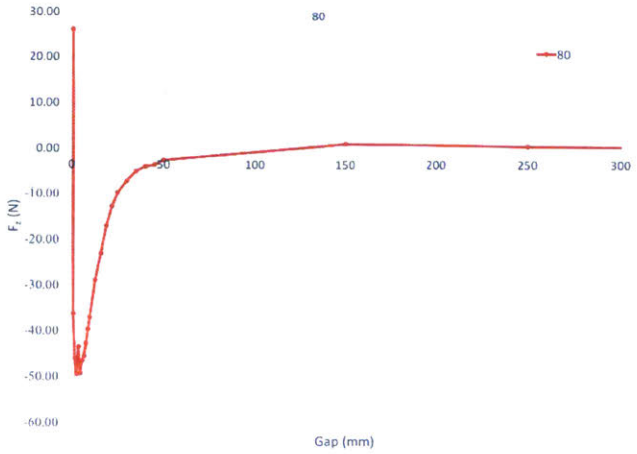

Figure 5-12: Experimental set up in lab showing the robot resting and hovering in a 5ft deep tank

5.7.1 Stable Points

In the first round of experiments, a robot with a net weight of 3gf (0.03N) was placed on the floor of a tank in 0.6m (2ft) of water. Being heavier than water, the body stayed in contact. When the bottom jet was powered at 3 volts, the robot still stayed in contact. As we raised the voltage, we observed a tendency to rock; we interpret that as being due to imperfect mating of the two surfaces. The fluid oozes out of the nozzle and forms a film below the robot. This was evident when the robot was lightly tapped. With the jet off, the robot would barely move; whereas with the jet powered, the robot moved smoothly and for considerable distance. It was simple demonstration of lubrication theory, except the lubrication fluid and the medium of propagation are both water.

Next the robot was attached to a force sensor and suspended above the floor of a 1.5m (5ft) deep tank. An ultrasonic range finder was used to measure the distance between the robot and the floor. At 1.4m (4.5ft) above the floor, and with the pump powered at 10V, the jet's thrust balanced the weight of the robot, i.e. the force sensor read zero. To check

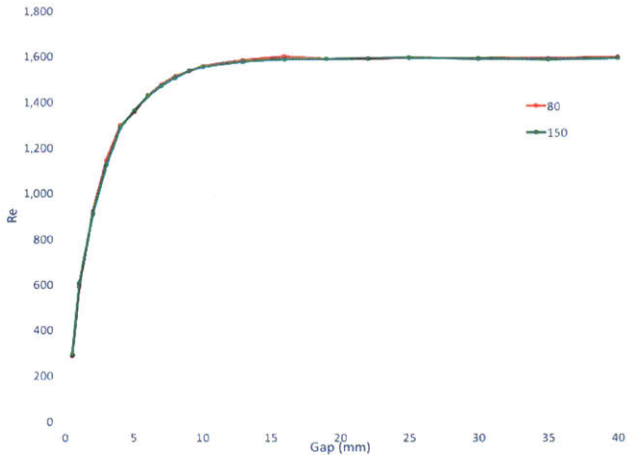

Figure 5-13: F_z verus gap for distances upto 100mm using the SST model. The zero cut off for the stable equilibrium matches experimental observatqwing few mm thickness of fluid bed layer. The upwash effect is however somewhat undermined in this model.

if we were already dominated by ground effects, we lowered the robot to 1.2m (4ft) depth while keeping the pump powered at 10V. It maintained a neutral equilibrium at that height as well, indicating the ground was not a dominant factor.

However at 1m (3.5ft) the body experienced an upward force pushing it back up to 1.2m (4ft). We put the robot at 1.4m (4.5ft) again and decreased the voltage to 8V; the robots started sinking, as expected, but stabilized at $\sim$ 1m (3.5ft). As we decreased the voltage the robot sank to a new stable point. This was observed down to 4V, where the robot stabilized at $\sim$ 0.6m (2ft) from the surface. At 3V, the robot sank to the floor. These measurements were repeated over 5 runs. Stable point versus pump voltage is shown in Figure (5-16).

The free stream thrust at each voltage can be calculated from the pump flow versus voltage characteristics (measured separately), from which we can deduce the upwash force at each stable point. The upwash force, normalized to thrust, as a function of gap is shown in Figure (5-17).

Our range finder could not measure distances $<$ 500mm and could not be used except in

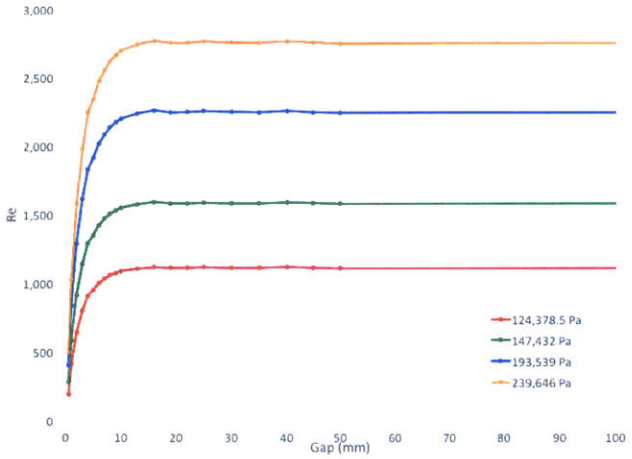

Figure 5-14: This is showing the F_z versus gap for various inlet pressures (and therefore flow rates) at smaller gaps

the upwash dominant region. However, our observations are in agreement with our CFD analysis, where the suction forces dominate over fountain upwash at small distances. The strong suction force could be demonstrated easily even when the robot is balanced by the jet at 9V. When a moving plate (or a hand) passes underneath the robot, the robot is instantly attracted toward and follows that surface, both in depth and laterally.

5.7.2 Lift Force

Our second set of measurements used a single point 100g micro load cell to measure force. The device is intended for use in sensitive, high precision weight scales and was well suited to the force range we anticipated. To constrain the robot to 1-dimensional, vertical-only motion in response to the jet, while still measuring forces in z, we used a low friction slide. One half of the slide was attached to beam which in turn attached to the water tank. The other half attached to the robot body via a rigid, vertical rod. A clamp between the rod and the slide allowed the robot depth to be adjusted: First the robot and slide were placed

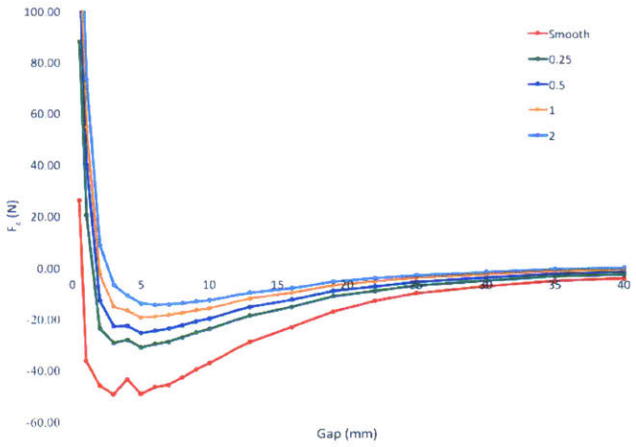

Figure 5-15: This is showing the Reynolds number versus gap for various inlet pressures (and therefore flow rates) at smaller gaps

at their desired positions, then the clamp was tightened. The buoyancy of the system was adjusted by adding or removing polystyrene foam until the robot, plus rod and (half) the slider, were a little more than neutrally buoyant: nominally, 50g upward force to place it in the mid-range of our load cell. The load cell was then brought in contact with the part of the slider connected to the robot. Finally, the height of the robot was checked and, if necessary, adjusted.

Our load cell is a 4-element device configured as a Wheatstone bridge to minimize sensitivity to off-axis forces. The load cell was read out with a commercial Wheatstone bridge interface board with amplification, digitization, and a USB interface. We chose to read data at 5Hz and average over ~ 20 seconds for each height and voltage setting. Since the buoyancy deliberately non-zero, but not precisely known, for each height setting we started with a pedestal, i.e. pump-off, measurement. This pedestal was subtracted from all subsequent measurements to separate jet-related forces from simple buoyancy.

The measurements are presented in Figure (5-19). Although the precision of the load cell

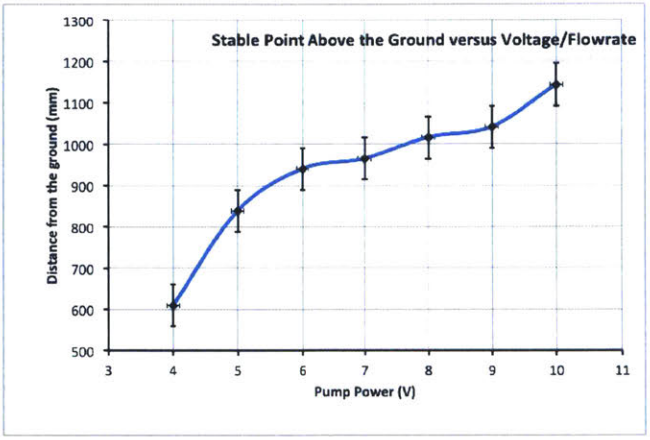

Figure 5-16: Height of stabilization, in mm, versus voltage. Error bars indicate the accuracy of our measurement device (vertical) and resolution of our power supply.

is excellent, there are many other potential sources of error in this setup. To quantify the accuracy of our data, after completing our measurements we retook a subset of the data. The two sets of data were found to have a 0.015 RMS deviation. To better understand the source of the errors, for the second set of data we retook pump-off data at the end of the measurements in addition to at the start. The deviation is is a measure of the system hysteresis which we attribute to friction, primarily in the slide. We found the pedestal measurements had 0.013 RMS discrepancy, essentially identical to the pump-on data. Based on these measurements we assert that our errors are dominated by friction. Since friction is unaffected by the jet and height settings, we assign a constant error to all data points.

For both experiment and CFD run - we simplify to using a elliptical plate of quarter inch thickness with a center outlet, since our interest is mostly about the hydrodynamics occurring at the bottom of this plate. For most of the work presented here, the upper body effect is not explored. The dependency on scale was explored. It was found that the ground force $F_g(h) \propto A \propto L^2$ where A is the area of the body and L is the length.

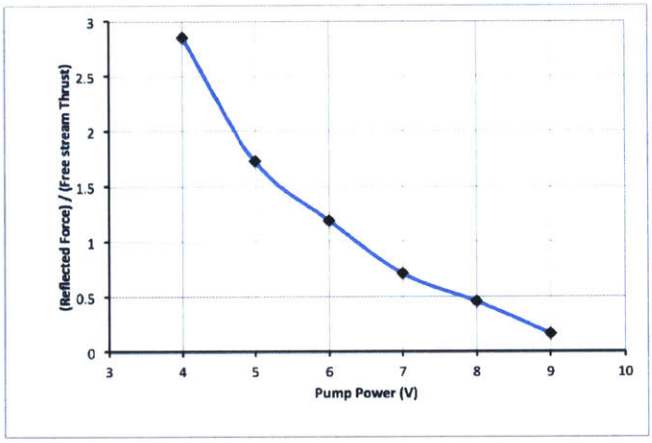

Figure 5-17: Upwash versus height is plotted as measured from the experiment.

The next parameter of interest was surface roughness. In a lab experiment, we used a rough mat with roughness factor $\varepsilon_r = \frac{\delta_r}{c} \approx .008$, where δ_r is the height of the surface roughness and c is the nozzle diameter. Intuitively one might think surface surface leads to turbulence in the flow, thereby would decrease the suction or Venturi effect. It was seen from the experiments that in fact the suction became stronger at smaller gaps but decreased at larger gaps.This is because rough surfaces causes local vortices leading to increase in suction, or pressure drop dominant when closer to the surface. The setup is shown in Figure 5-20 and a comparison example with the given mat and just glass surface is shown in Figure 5-21. To measure the forces, we conducted an experiment constraining the body to only one degree of motion (Z) and used a single point 100g micro load cell. Sensors used are two kinds- a precision distance sensor and a larger distance sensor (ultrasonic distance with .05 mm accuracy). The force sensor is a 100gm micro load cell. Repeatability and hysteresis for this sensor is $\approx .005N = 1/100$ of the force measured. Setup shown in Figure 5-18. The sensor data is further filtered to get a precise estimation of the distance from the ground. Effects of other submerged portion subtracted out through subtraction of the value at no

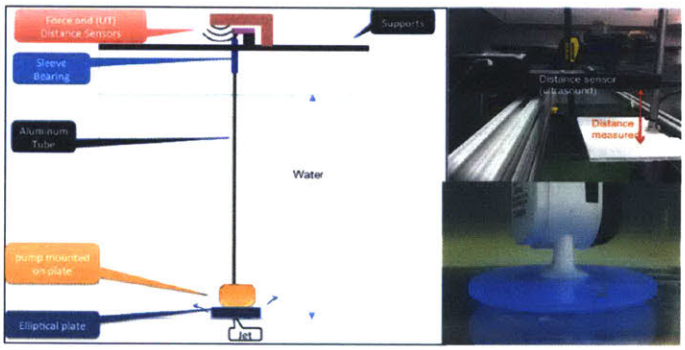

Figure 5-18: Left: Schematic showing experimental setup with elliptical plate. Right Top: Setup for Distance Measurement. The white plate moves with respect to the ultrasound sensor along with the elliptical plate. When the body touches the ground, the white plate is the furthest from the sensor (taken as positive distance). Right bottom: Pump mounted on elliptical plate resting at equilibrium

load (no pump). Error sources came from the friction in the slider , sensor measurements, limitations in reproducibility of the setup and inaccuracy in the system measurement.

As mentioned, instead of using the whole robot, we used elliptical plates cut into the shapes of robot's bottom. We looked into the effect of a sudden external force on the system with different buoyancy conditions pushing it all the way to the ground. The set up is shown in Figure 5-18. A ultrasound distance sensor was used in the arrangement shown to measure distance. Note, negative distance implies away from the ground as measured by the sensor.The system response is given byFigure (5-22).

5.8 Conclusion

The conceptual design presented in this chapter opens up a whole new method of traversing underwater surfaces. Extending work done for air as the fluid medium, we developed a simple prototype to allow hovering and gliding underwater using single jet impingement on the ground. Our analysis of the dynamics of this configuration show it can be understood

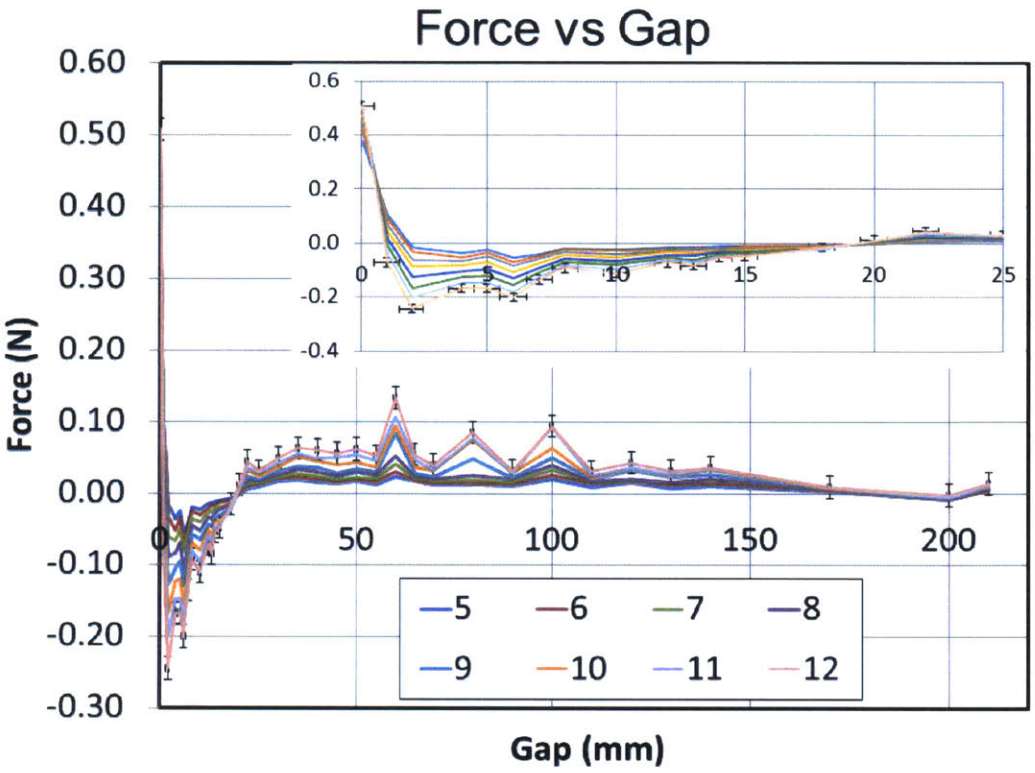

Figure 5-19: Experimental Results for force vs gap for various voltages. Inset: zoom in on small gap data. Error bars based on reproducibility; see text.

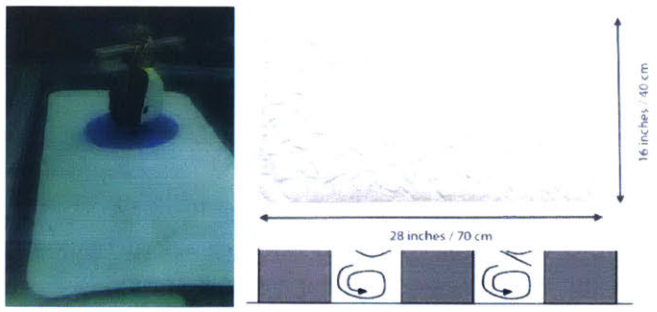

Figure 5-20: Experimental Setup for Roughness Test

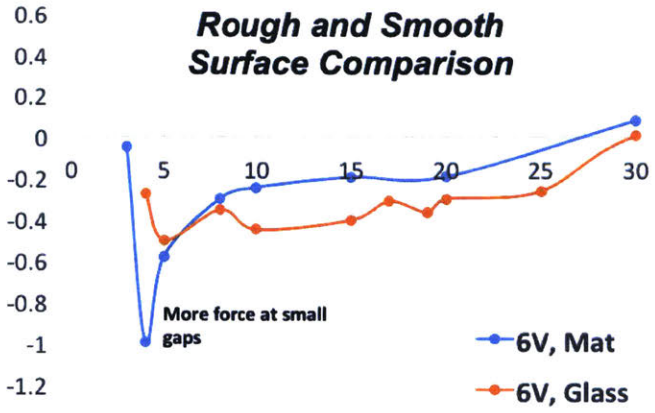

Figure 5-21: Ground Effect Force comparison between rough surface and smooth(glass) surface

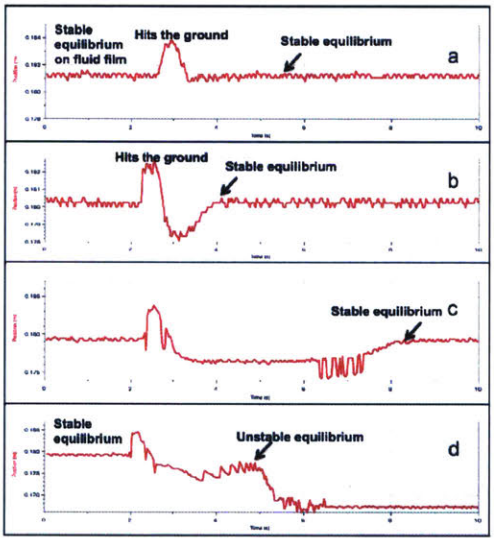

Figure 5-22: (a) An force of 5N given. Very damped system, stabilizes right away on the fluid film (b)Body made slightly more buoyant- note the body bounces on the other side of the equilibrium into the venturi region and is sucked back to stability (c) Body is made even more buoyant - experiences lesser venturi force - oscillations representing possible lateral vibrations (d)Further increase in buoyancy shows for the same force - the body escapes the venturi region and passes through the unstable equilibrium to free stream region- flat section. (max distance allowed in the experiment)

Table 5.1: F_g dependency on Robot Parameters

Size	$\propto d^2$ *where* $\pi(d/2)^2$ *is the bottom area*
Height and Size	$\sim \varepsilon = h/d$
Body Lateral velocity	$\propto \dot{x}^2 + \dot{y}^2$
Downward Jet velocity	$\propto w_{J_j}^2$
Surface Roughness	Sharper, deeper dip at low h for rough surface

as a cross between traditional lubrication theory at small gaps, and upwash at larger gaps. With the body close to the ground, flow out of the nozzle oozes across the bottom surface, forming a thin film which enables smooth sliding motion: traditional lubrication theory. It may however be debated if the flow of this fluid film is turbulent or laminar and there remains work to be done on radial turbulent flow through parallel disk. As distance to the ground is increased, initially ground induced lift losses dominate: the body pulls back to reduce the gap, i.e. this is a stable equilibrium point. As the gap is increased further, lift enhancement from upwash pushes the body away. This phenomenon fades as distance is increased still further. This behavior, well matched to those of VTOL aircraft hovering near the ground, creates another stable equilibrium point. Preliminary experiments confirmed the existence of the phenomenon with clear demonstration of suction, upwash, and stable equilibrium points. Empirical results are qualitatively and quantitatively confirmed by different types of CFD analysis (different models used). Future work should focus on improving both the apparatus – eliminating the tether for power – and the simulation : capturing incorporating thin film modeling and the transition to turbulent flow accurately in a single model.

Chapter 7

Data Driven Linear Model of UUV with Augmented States

In Chapter 3 we demonstrated simple control of a robot on a smooth horizontal plane without explicitly accounting for ground effects. Subsequent chapters presented experimental observations and CFD simulations of the hydrodynamic ground force, F_g, and an analysis on how the force affects the system at various regions of operation, given by $\phi(h,w)$ near the target surface of inspection. To take advantage of these hydrodynamic phenomenon in a real application, we need a control system which incorporates the ground effect; and this in turn requires a suitable system dynamical model. We start by noting the complexity of F_g vs H curve: highly non-linear, with multiple equilibrium points. The problem is not amenable to analytic solution. Further, CFD simulations are computationally intensive and, while sufficient to guide the design, are not robust enough to directly build the model. In the absence of a well defined analytical model, we apply a data-driven approach. In order to study the results in detail, we use a large number of simulated data samples that sufficiently covers the entire

operational region; however, the method is suitable for use on real data as well.

Our goal is to develop a demonstrably stable and robust control system. We require a method where accurate state estimation is possible despite modeling errors, such as unaccounted variables affecting system dynamics. Traditional linearization by tangent line approximation fails in such cases. Therefore we propose to apply a new and novel approach: we recast the non-linear system to a higher dimensional space with "auxiliary" state variables where the system becomes linear. (A simple example is $y = x^2$, which is non-linear in $[y,x]$ space but becomes linear in $[y,x,x^2]$ space.) This method allows us to form a nominal state matrix which is combined with a state estimator for optimal estimation of the non linear elements. A simple robust controller can be then designed to compensate for these non linearities based on on-line estimation.

The non linear forces we will consider are drag and hydrodynamic ground effect forces, F_d and F_g respectively. In the 1-dimensional system we will work with, estimating just the total force F_T, would suffice in many cases. Separate estimate of F_d and F_g is more challenging, but opens up a number of options. First, it more readily generalizes to a real-life, 3-dimensional problem. Our goal is to ensure for inspection purpose we are using the hydrodynamic ground effect to our benefit to maintain the close proximity without costly actuator control effort. In reality, the amount of suction needed would depend on many external factors that are not known a-priori, like surface roughness, turbulence and others. The single impinging jet flow rate must be therefore be controlled accordingly to ensure correct amount of suction and fluid bed layer thickness. Therefore it is necessary to estimate the suction experienced by body and how the jet impingement must be controlled to generate the correct force. However, recall venturi suction results in coupling between motion parallel to a surface and force perpendicular to the surface in presence of an impinging bottom jet as we saw in Chapter 4 and 5; there is no analogous coupling for the

drag force. Thus, in the more realistic case of 3-dimension motion, separately modeling F_g and F_d would be required. Second, as we found earlier, the ground effect depends on the smoothness of the surface. Thus, an independent estimate of F_g is a measure of the surface. Besides being potentially valuable information in itself, it allows higher-level logic to select among a range of models for the one most applicable to the circumstance. This is illustrated in Figure (7-1) and Figure (7-2). It is to be noted, for the scope of our problem, we will assume a fixed impinging jet denoted by u_j which remains constant in the problem. The

The concept of state estimator for a data driven linear model and feedback control will be explored in Chapter 7. In this chapter we will briefly present some background on existing data driven methods of system modeling, limitation of traditional linearization methods, and then turn to the use of Principal Component Analysis (PCA)[28] for forming a linearized model. We discuss the performance based on the covariance matrix, order of truncation of the latent variables, sampling processes, number of auxiliary variables, and region of operation. The method described in the chapter forms a critical part of the doctoral thesis contribution and opens a entirely new approach of data driven dynamical system modeling and control to capture non linear system behavior and estimation of individual non linearities which cannot be done by traditional linear approximation techniques.

7.1 Literature Review

Data-driven techniques are increasingly important as a vast amount of data is becoming available at low cost [66]. Various systems working in the field are now monitored 24/7. Field data uploaded to a cloud environment are analyzed for providing better maintenance and efficient services. Construction machines, for example, have been monitored for predicting the life span of key components, so that replacement parts can be ordered in

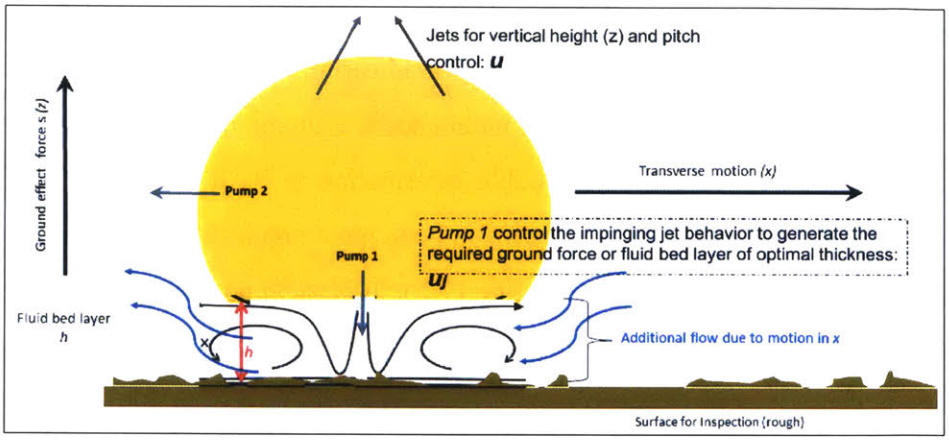

Figure 7-1: Multi-DOF Coupled Motion

The actual robot will move in multi-DOF and has coupling in the non linear forces. For example, while moving in longitudinal motion on the inspection surface it also has the bottom jet for forming fluid bed turned on. Total ground effect forces along (z) axis therefore are the net result of both the passive and active (or jet induced) forces. The drag force along (z) axis however is very small since there is no significant motion along (z) . Therefore separate force estimation is useful.

advance. As instrumentation and communication technology grows further, more detailed and richer variety of data will be available from the field. Yet, the challenge is to find a way to extract useful information, develop new services and improved products by exploiting the data. Cloud computing also generates a vast amount of data through advanced simulation. Detailed computational models have been available for many complex machines and systems. Yet, potentials of valuable data have not yet fully been explored and exploited.

For the control community, emerging data technology will open up a new opportunity to augment its core methodology with a data-centered methodology. The challenge is to extract critical information from the vast data that is required for control design. Such data may include signals beyond the standard input-output data, and may contain information more than state variables. For complex non linear systems like ours, the question is which set of variables sufficiently informs the dynamics of the system and are useful for control.

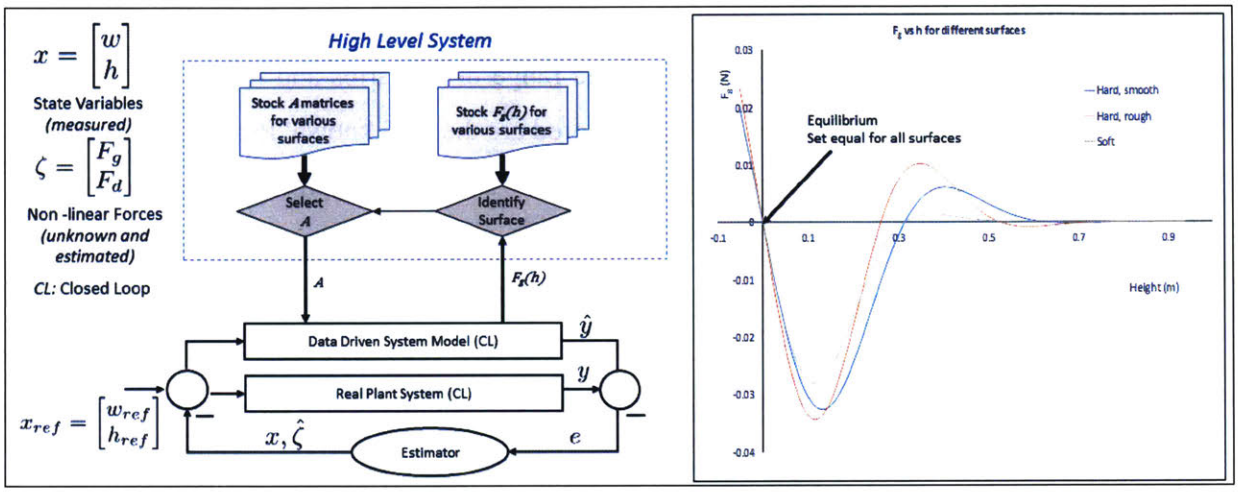

Figure 7-2: High Level System diagram: Roughness Identification

Using estimated ground force to in turn predict the surface roughness and identify the right dynamical model for the operation. Roughness of target surface will not be known with accuracy prior. However, it will be studied and modeled and the information will be loaded on the system's computer.

Here, we address how we can find informative variables for a class of unknown nonlinear dynamical systems, and how we can reduce them to a state equation in the space that is useful for system analysis and control synthesis.

There are different statistical data fitting methods for constructing a linear model but they are often not optimal when dealing with large amount of data. Though the example in this and the next chapter would be a simplified second order system. These can either measured or simulated. It is easier to establish the foundational framework of a method using simulation data to encompass a wide range of scenarios and then move to actual system data. For large data spaces, we explored are the well known"Principal Component Analysis" (PCA) and a more newer technique: "Subspace Identification Methods" also known as "4SID methods" (Subspace State Space Systems IDentification) [71]. These are alternative to the usual regression methods like ARX or ARMAX and are based on concepts of geometric projections and linear algebra. They are robust techniques (can be implemented with robust methods like QR and SVD factorizations), have same computation complexity for both SISO and MIMO system and are guided by only one parameter: system order (to what high dimensional space you would like to transform the model to). However, the underlying math being extremely complex, it generates a black box model from which it is very difficult to grasp how various dynamical parameters are reflected into the model, and how tuning them changes it. We did some initial work using this method, but majority of the work and ultimate results uses the PCA method.

The PCA approach uses what we call the "latent variables" denoted by "z" [72]. Latent variables are variables which are not observed but rather inferred through some transformation and are key to dimensionality reduction while retaining system information to the required resolution. "Latent space" or "z-space" can be viewed as a rotation of the original state variables defined by the system's modal matrix. It is an unambiguous, reversible mapping from one space to another: - when no truncation is involved, no

information is lost (or added) in the process, and conclusions drawn in one are readily transferable to the other.

Using a Latent Variable technique combined with physical modeling theory, two salient features and properties have been explored. One is a systematic method for finding a complete set of variables that can sufficiently inform the system's nonlinear dynamics. Independent state variables are augmented by adding auxiliary variables that are needed for describing constitutive laws of individual components, which may be nonlinear. The other major result is that the nonlinear dynamical system in the augmented space can be represented as a linear equation. The class of nonlinear dynamical systems behaves linearly when it is recast in the high-dimensional space derived from the augmented state space that is sufficiently informing. While the resultant latent state equation is linear, complex nonlinearities are embedded in the compact model, leading to precise and global linearization of nonlinear dynamics.

New approach to the data drive method using bond graph theory [67] has been explored in [68],[69].This chapter extends the approach to both autonomous nonlinear systems to non-autonomous, nonlinear systems for our UUV [70] . A data matrix is formed by collecting samples of a set of sufficiently informing variables. It will be shown that a class of nonlinear dynamical systems can be exactly linearized and represented as Differential Algebraic Equations (DAE) in augmented state space. A causal linear state equation is also derived from the data matrix, which approximates the nonlinear dynamics precisely. The richness of data matrices is evaluated in terms of matrix rank, which is upper-bounded due to the structure of the nonlinear dynamics. Though the method is proposed for general application, we demonstrate it through our complex non linear 2^{nd} order UUV model with a single impinging bottom jet and moving on a single axis.

The power of data driven modeling in capturing non linearity can be once for all explained in terms of a non linear spring through the Figure (7-3). When a non linear

spring is modeled using solely traditional method like Taylor series, one can notice that depending on the line fit, it is possible to miss out on most of non linearity. On the other hand, statistical modeling method often capture the more of the non linear behavior based on the population of the data samples in the non linear area. Having more data samples in the non linear region will force the trend line to pass through that.

An important question that comes up in the high dimensional linear representation of the system is: redundancy. The original system is second order, is a higher dimension space linear model then essentially rank deficit? The answer is no. The higher dimensional model is not formed from a traditional Jacobian matrix. We will explain this with the well known mass spring damper system example.

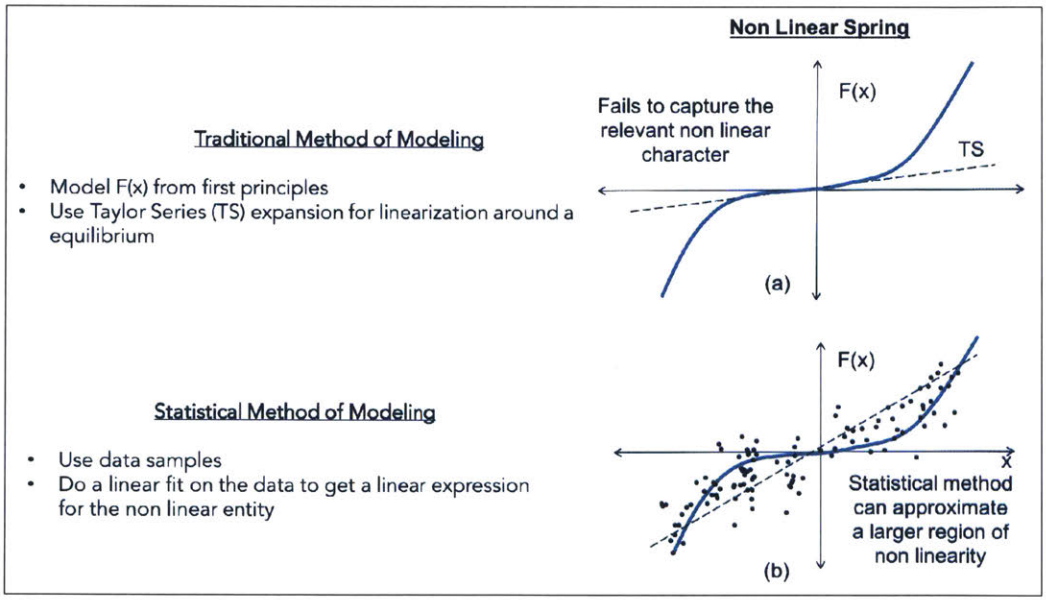

Figure 7-3: Explanation of why data driven modeling helps to capture non linearities that traditional modeling cannot through the case of a non linear spring.More data samples of the non linear behavior help to form a trend line that capture those non linearity better than in a traditional Taylor Series method

For example, let in a mass spring damper system, F_s be the spring or restoring force and F_b is the damping force respectively. We know, states of a system are not unique. So, if the forces were linear, adding them to the second order model would be redundant since the states and the linearly dependent forces are interchangeable. That is there is an exact reversible relationship between them- one can be derived from the other in the state space model. Let k be the spring constant , x is the elongation and u be the external force.

$$\begin{aligned} m\ddot{x} + b\dot{x} + kx &= 0; \\ F_s = -kx &\rightarrow \text{ linear relation} \\ F_b = b\dot{x} &\rightarrow \text{ linear relation} \end{aligned} \tag{7.1}$$

Non linear Model :

$$\begin{aligned} F_s &= f(x, F_s, F_b, u...) \text{ linearizing} \rightarrow J_s \\ F_b &= f(x, F_s, F_b, u...) \text{ linearizing} \rightarrow J_b \end{aligned} \tag{7.2}$$

But if F_s and F_b were highly non linear function, the Jacobians wouldn't capture all of the non linearity. In addition, if there may be uncertainty in the non linear function representation relating the state variables and the forces. The Jacobian J_s and J_b do not contain all the information required for estimating states from the non linear forces or vice versa.Therefore the following equations are not reversible anymore- and here the addition of the non linear forces as auxiliary states in the high dimensional linear model helps to enrich it.

7.2 The System Model

Hydrodynamic force on a body in motion in the vicinity of a submerged surface is substantially different from motion in the free stream and is under-explored. The $Fg(h)$ curve in Figure (**??**) is unique and challenging to model - particularly due to the presence of two distinct equilibria- one stable at very small distance and one unstable at a comparatively larger distance. The system dynamics is characterized by complex non linearities which are non monotonic in nature. Traditional linearization techniques using a tangent line approximation and Jacobian matrix though preferable captures very limited operational area (less than 3%) at extremely low velocities which we will demonstrate as below.

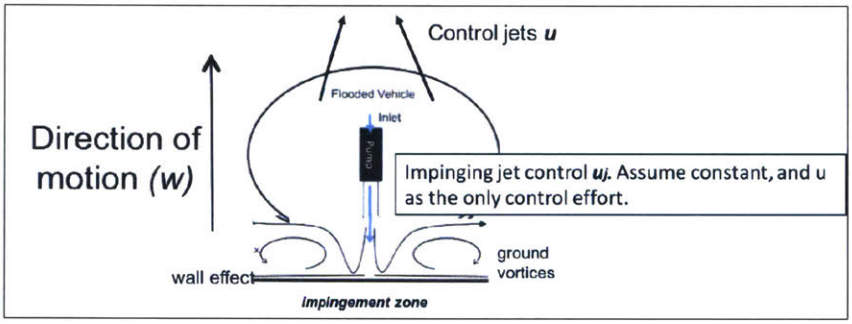

Figure 7-4: Vertical Motion of EVIE with Single Impinging Jet

The non linear equation of the single axis vertical motion of the jet impinging robot as shown in the Figure (7-4) as described in Chapter 5 is given by:

$$\boxed{\dot{w} = \frac{1}{S_z}[(mg - F_b) + F_g(u_j, h) + F_d + F_j + u]} \tag{7.3}$$

$$\boxed{\dot{h} = w} \tag{7.4}$$

where, F_d, the drag force (if considered quadratic) is given by $F_d = Z_{ww}w^2$, and w is the

vertical velocity of the robot. The impinging bottom jet at a particular flow rate (or control input u_j) gives rise to two kinds of forces: the constant thrust force F_j and a ground effect force $F_g(h)$. Far from the ground - in the freestream- at a height H_{fs}, we have $F_g(h) = 0$. Therefore, for a fixed u_j we can treat F_j merely as a bias or offset and there's no need to include the same in our equations going forward.

The non linear terms - F_g and F_d - are major constrains to linearize the above equations for constructing typical state space linear model. For traditional linearization we need a physical equation of the system. Since we do not have the same for $F_g(h, u_j)$, we fit it to a parabolic curve to the simulation data of F_g and h that covers up to the upper bound of the venturi or "suckdown" region or the second equilibrium. The fit given by equation (7.6) is shown in Figure(7-5) which is then linearized.

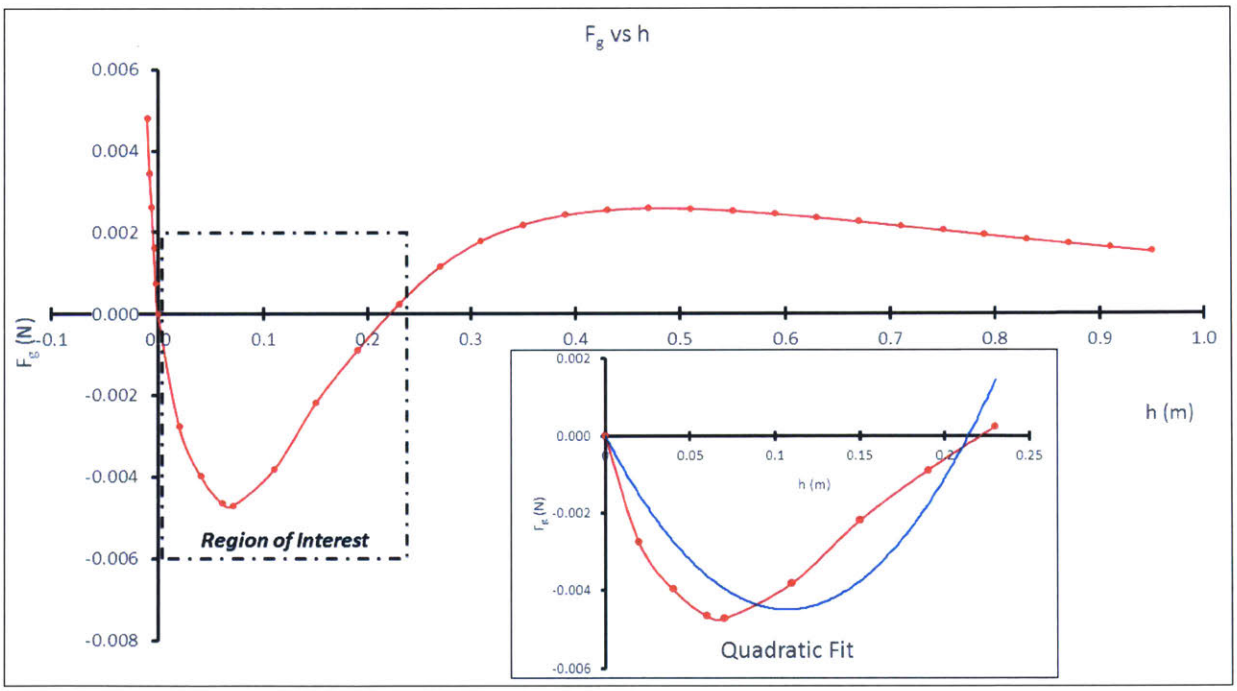

Figure 7-5: Parabolic Fit in the region of Interest (Venturi Suckdown)

$$F_g(h,u_j) = u_j[\alpha h^2 + \beta h + \gamma] \tag{7.5}$$

where α, β, γ are the fit parameters.

For a robot like EVIE with given shape and size moving on a surface of given roughness, and with a particular impinging jet control input U_j (which is the input at the stable equilibrium condition), we have F_g solely as a function of h. Total force in (z)

$$F = U_j[\alpha h^2 + \beta h + \gamma] + Z_{ww} w|w| + u] \tag{7.6}$$

So now the equation (7.3) can be expanded by substituting for F_g

$$\dot{w} = \frac{1}{S_z}[(mg - F_b) + u_j[\alpha h^2 + \beta h + \gamma] + Z_{ww} w|w| + u \tag{7.7}$$

In the region of the operation, the drag function is complex: linear at very small velocities, transitioning to quadratic at larger velocities, and ideally with a fifth order polynomial splice between the two. This is shown in Figure (7-6).

In equation (7.7) , u_j is the thrust control for the bottom impinging jet that regulates the thrust force F_j and goes quadratic as jet velocity w_j. The actual control input is given by u.

If we use the quadratic drag model, as before- the linearized parametric model is given by-

$$\begin{bmatrix} \dot{w} \\ \dot{h} \end{bmatrix} = \begin{bmatrix} Z_{ww} w_e & u_e(2h_e\alpha + \beta) \\ 1 & 0 \end{bmatrix} \begin{bmatrix} w \\ h \end{bmatrix} + \begin{bmatrix} \frac{1}{Sz} \\ 0 \end{bmatrix} u \tag{7.8}$$

where the subscript 'e' denotes the value at the equilibrium.

Let us now consider the equilibrium position. We mentioned that $u_e = U_j$ here.We shift our F_g vs. h curve for convenience, such that now $F_g = 0$ passes through $h = 0$. The

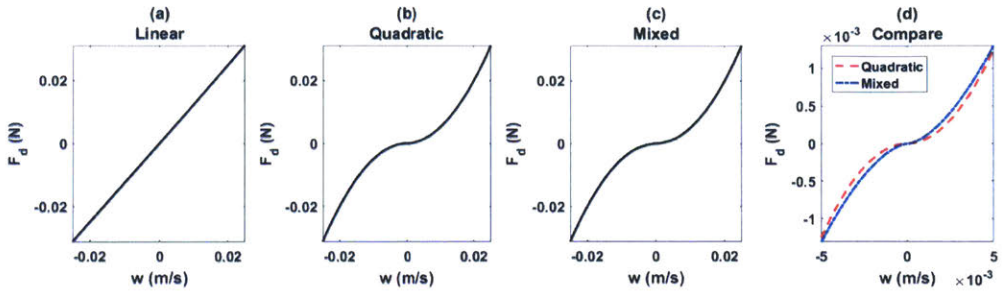

Figure 7-6: Drag Types- (a) Linear – augmented state F_d linearly dependent on w. (b) Quadratic – F_d quadratically dependent on w. (c) Mixed – linear for Re<1, quadratic for Re>1000, 5^{th} order polynomial for smooth transition between the two. (d) Comparison of quadratic and mixed drag at low velocity; note the small linear term for $w \rightarrow 0$ results in more realistic damping of perturbations after many seconds.

fluid bed layer therefore occurs at negative values of h. Hence the states at the equilibrium conditions are given by $w_e = 0v/sec$, $h = 0m$. When the values are substituted in the Jacobian matrix of the state space model, the damping term disappears leading to the failure of the linear model.

$$\begin{bmatrix} \dot{w} \\ \dot{h} \end{bmatrix} = \begin{bmatrix} 0 & U_j\beta \\ 1 & 0 \end{bmatrix} \begin{bmatrix} w \\ h \end{bmatrix} + \begin{bmatrix} \frac{1}{Sz} \\ 0 \end{bmatrix} u \tag{7.9}$$

The second alternative is a hybrid linear model - also known as the 'equivalent linear model', where we apriori have an estimate of the range of velocities the body can attain, and we use the average RMS value of the velocity and that accounts for the damping. This basically uses either simulation or experimental data to get the estimate and is therefore a hybrid between a linear and a data driven model.

$$\begin{bmatrix} \dot{w} \\ \dot{h} \end{bmatrix} = \begin{bmatrix} Z_{ww}w_{rms} & U_j\beta \\ 1 & 0 \end{bmatrix} + \begin{bmatrix} \frac{1}{Sz} \\ 0 \end{bmatrix} \tag{7.10}$$

The performance is seen in the Figure 7-7. The linear model (blue) shows no damping, the modified linear or pseudo linear model (red) shows a smooth convergence to equilibrium and the non linear model (black) simulation shows damped oscillations and eventual stabilization at equilibrium. As you can see the hybrid model however fails to predict at the positive slope region. We will come back to linear model comparisons later in the chapter, but the limitations are clear enough from this section to transition from a hybrid to a fully data driven technique.

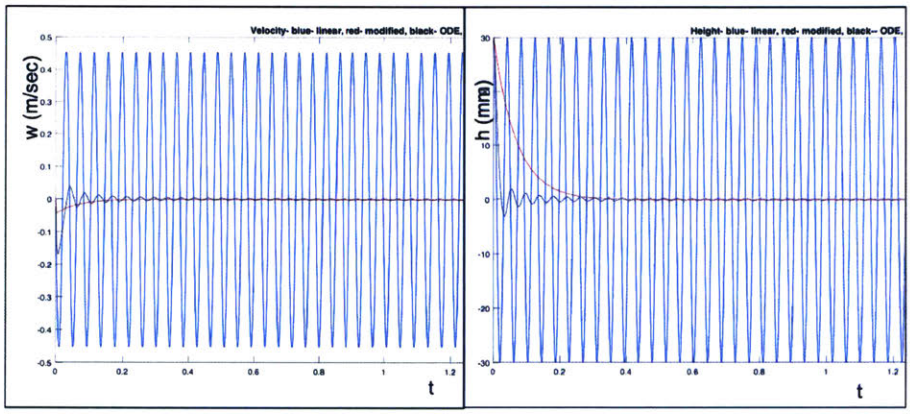

Figure 7-7: Blue: Linear model Red: Modified Linear Black: Non linear ODE simulation results. Left: Velocity Right: Height

7.3 Data Driven Model for UUV

Our goal is a linearization model that captures the dynamics of a non linear system more accurately, and over a wider operating region, that is possible with the standard Taylor series expansion into a linear Jacobian matrix.

Most real systems are non-linear in nature. Standard linearization methods function well only over a narrow region and small perturbations. This limits the range over which

the controller can be applied. An example would be a car engine. When the engine is pushed towards the boundaries of its operation, problems such as knocking and misfiring occur. The need to capture a greater part of the system dynamics and allow a control method satisfying the boundary constrains robustly is therefore very much needed.

As seen in the previous section, the same problems applies for our robot approaching a target surface with non linear forces acting on it. The unique and challenging features of this highly non linear F_g vs. h Curve shown in Figure (7-5) is the presence of multiple equilibria (one stable, one unstable and one neutral at far distance) and no simple, well established physical model. Compounding the complexity is the need to include a non linear drag force. Thus system dynamics are non linear and even non-monotonic in nature and therefore might demand the use of non linear control. Yet for real applications, a simple robust feedback control compensating non linearities that can be easily integrated with a linear dynamical model has a large advantages; whereas, as we noticed in the previous section, traditional linearization fails to capture most of the system's critical behavior in the operational region. Hence we investigated methodologies to develop a linear model that sufficiently informs us of the system over a wide region of interest.

Given there is no simple linear model to capture non linearities, we explore directly incorporating data – experimental or CFD simulation – to build a linear model that is capable of capturing nonlinearities. This is done by augmenting the state variables with "auxiliary variables" associated with the non linearities in the output vector. As mentioned before, we chose to use PCA as being more intuitive, and therefore more robust.

A natural question to ask is: why do data driven methods make sense now, whereas linear methods have been used extensively in the past? This system is complex – but many systems, past and present, are as ore more complex. The reasoning can be summarized as follows.

- Increased focus on autonomous systems which must tolerate a wider range of conditions without human intervention
- Development of a wide range of economical, fast sensors to collect information previously unavailable
- Availability of memory and computing power to collect and process large bodies of data
- Related to the above, development of "Big Data" algorithms we can learn from
- Advances on the CFD front and other simulation platforms allowing more reliable modeling of complex systems

The underlying hypothesis in the data driven approach is that dynamical systems behave linearly when recast in a suitable higher dimensional space. State variables are augmented by adding auxiliary variables that sufficiently inform the nonlinear dynamics of the system. We start with a data matrix containing a large number of samples in the augmented state space. This is then analyzed to extract latent variables that in turn predict state transitions in the latent space. There are many ways to determine the so called auxiliary variables. One way is through a physical system representation via a Bond Graph where the connective structure of networked elements is known, but the constitutive laws of individual elements, which may be nonlinear, are unknown. Or in absence of a good understanding of the physical model or a systematic methodology to derive it, auxiliary variables can be chosen as polynomial representations of various orders. We use Principal Component Analysis (PCA) to compute the latent variables. The latent variables are used to generate an exact linearization of the Differential Algebraic Equation (DAE) in the augmented state space. The resultant matrices are then used to get approximate linear state space model in the true (non-augmented) state space.

Before we begin with our simplified example, the following point must be understood. The focus of this thesis is a thorough understanding of estimators for multiple non linear forces. To this end we use a single degree of freedom and only two measured variables – w and h – from which we estimate two auxiliary variables: F_g and F_d. With this minimalist data set, we do not benefit from the data handling capability of PCA. Direct linear fitting methods are well understood and easily applied. In fact the overall approach here would work with any conventional fitting technique.

As we expand the system for multi DOF motion, with number of non linearities increasing as there are more and more coupled forces, and environmental factors like turbulence that enter the model, there is a increasing need for more and more data in order to model those complex non linearities. The power of PCA enters when we expand the number of measurements, i.e. sensors. As noted previously, the availability of low cost sensors makes it cost effective to use more than the minimal number of sensors. An example is velocity sensors distributed around the surface of the robot, each giving a local water velocity measurement. Each measures a linear combination of u, v, w depending on the sensor location. PCA is well suited to extracting the relevant information from such an array of data. The example problem in the thesis is to demonstrate the overall approach, which is fairly complex by itself, and therefore has been kept simple to a second order system model.

7.3.1 Theory

Let $x \in \Re^{n_l}$ be the original state variables. let $\zeta \in \Re^{n_{nl}}$ be the auxiliary state variables formed by non linear elements. The auxiliary variables are chosen such that the original state variables are linear in the auxiliary variable space. However, from a more theoretical background, it can be derived from a bond graph approach mentioned in [68]. The combined

the Augmented State Vector is

$$\tilde{x} = \begin{bmatrix} x \\ \zeta \end{bmatrix} \in \Re^{(l \times 1)} \quad l = n_l + n_{nl} \tag{7.11}$$

Dynamic transition of the system is represented by by ζ, input $u \in \Re^r$, and the time derivative of the state, $\dot{\tilde{x}} \in \Re^l$. Thus

$$\eta = \begin{bmatrix} u \\ \tilde{x} \\ \dot{\tilde{x}} \end{bmatrix} \in \Re^{(r+2l)} \tag{7.12}$$

sufficiently informs the entire system.

Let $\eta_1, \eta_2 ..... \eta_N$ be N samples of these sufficiently informing variables. Concatenating these we can form a data matrix:

$$X = (\eta_1 \eta_2 ..... \eta_N) \in \Re^{(r+2l) \times N} \tag{7.13}$$

For us

$$\eta = \begin{bmatrix} u \\ w \\ h \\ F_g \\ F_d \\ \dot{w} \\ \dot{h} \\ \dot{Fg} \\ \dot{Fd} \end{bmatrix} \tag{7.14}$$

PCA depends on the loading or weight vectors as discussed earlier. For a meaningful comparison of eigenvalues the PCA needs mean centered and "dimensionally homogeneous" input. For most data cases, including ours, this does not hold hold true for the raw input. The most standard solution is to offset and normalize the data

$$x_{PCA} = \frac{x_{raw} - \mu_x}{\sigma_x} \tag{7.15}$$

where μ_x and σ_x are the mean and standard deviation, respectively, of x. We will discuss later the impact of the offset affects results.

The structure of the data matrix X fed to the PCA is as follows.

$$X = \begin{bmatrix} u_0 & u_1 & u_2 & \ldots u_N \\ \tilde{x}_0 & \tilde{x}_1 & \tilde{x}_2 & \ldots \tilde{x}_N \\ \dot{\tilde{x}}_0 & \dot{\tilde{x}}_1 & \dot{\tilde{x}}_2 & \ldots \dot{\tilde{x}}_N; \end{bmatrix} \in \Re^{(r+2l)\times N} \tag{7.16}$$

where it is understood that the variables in X are mean-centered and normalized to unit width, the exception being where we explicitly consider the impact of the offsets. It is important to ensure that there is sufficient training samples such that the system has been excited in all possible operational region of interests.

The interrelationships between the elements of η will be summarized by the covariance matrix

$$C = \frac{XX^T}{N} \in \Re^{(r+2l)\times(r+2l)} \tag{7.17}$$

C contains the variance (diagonal) and covariance (off-diaganol) associated with the variables. Note due to our choice of normalization, the diagonal elements of C are 1.

Since C a square, symmetric matrix, we can apply eignevalue decomposition

$$C = MDM^T \tag{7.18}$$

where the Modal matrix M is an orthogonal matrix containing the eigenvectors of C, and D is a diagonal matrix containing the eigenvalues. For systems with a long η vector, C is likely to be rank-deficient since there might be at least one or more one exact linear relationship (e.g. $\dot{h} = w$). Therefore it will have one or more zero eigenvalues. The examples in the result section will illustrate the same. Assume the eignevalues are sorted in descending order, and truncated such that

$$\begin{aligned} D &= \text{diag}(\lambda_1, ...\lambda_m) \\ \lambda_1 &> \lambda_2 > .... > \lambda_m > 0 \end{aligned} \tag{7.19}$$

with $m < (r+2l)$. Let $T \in \Re^{(r+2l)\times m}$ be the truncated orthonormal matrix with eigenvectors associated with zero eigenvalues dropped; note T is *not* square. Our formulation sets an upper bound on m, but we may choose to the truncate at any order at or below this bound. We will revisit the impact of truncation order during analysis of results.

The orthonormal matrix T now can be decomposed into three blocks associated with u , $\tilde{x}$, and $\dot{\tilde{x}}$, respectively.

$$T = \begin{bmatrix} U \\ V \\ W \end{bmatrix} \qquad U \in \Re^{r\times m}, \quad V \in \Re^{l\times m}, \quad W \in \Re^{l\times m} \tag{7.20}$$

In our case, $r = 1, l = 4$. Transforming η by T yields the principal componenets, which

we can break into three terms

$$\begin{aligned} z &= T^T \eta \in \Re^{m \times 1} \\ &= U^T u + V^T \tilde{x} + W^T \dot{\tilde{x}} \end{aligned} \tag{7.21}$$

$$u = Uz \tag{7.22}$$

$$\tilde{x} = Vz \tag{7.23}$$

$$\dot{\tilde{x}} = Wz \tag{7.24}$$

Substituting (7.21) in (7.24) gives an exact linear Differential Algebraic Equation (DAE) for the non linear system

$$(I - WW^T)\dot{\tilde{x}} = WV^T x + WU^T u \tag{7.25}$$

We note each row of W is a complete row of T. If we apply no truncation in T – i.e., T is a square, orthonormal matrix – $W^T W = I$ based on the orthonormality condition of T. However, since a column of W is a partial column of T, $WW^T \neq I$.

7.3.2 Approximated State Equations

Method 1

Equation (7.25) can be written as:

$$\dot{\tilde{x}} = (I - WW^T)^{\#}(WV^T x + WU^T u) \tag{7.26}$$

Using, $W_i = (I - WW^T)^{\#}$ where # denoted pseudo inverse, equation (7.26) can be written in the familiar linear state space form as

$$\begin{aligned} \dot{\tilde{x}} &= \bar{\tilde{A}}\tilde{x} + \tilde{B}u \\ \bar{\tilde{A}} &= W_i W V' \\ \bar{\tilde{B}} &= W_i W U' \end{aligned} \tag{7.27}$$

Note the use of a pseudo inverse (indicated by #) is necassary since $(I - WW^T)$ is not of full rank. Further, for some choices of truncation order, it may be singular e.g. for $m = l$, W is a square matrix and

$$W^T W = I \Rightarrow WW^T = I \rightarrow I - WW^T = 0 \tag{7.28}$$

Thus the pseudo inverse does not entirely eliminate the issue of inverting $I - WW^T$. However, it is important to know this is an exact linearization where the error is bounded by the error due to pseudo inversion of W. We need to consider the optimal truncation order in applying (7.26) and also determine if a correction or method can be applied for the inversion error.

Method 2

To avoid ambiguity from the inversion of $(I - WW^T)$, an alternative derivation is given here. Let $\varepsilon \in \Re^{(l+r)\times 1}$ be the combined vector of augmented and state variables

$$\varepsilon = \begin{bmatrix} u \\ \tilde{x} \end{bmatrix} \tag{7.29}$$

Let

$$S = \begin{bmatrix} U \\ V \end{bmatrix} \tag{7.30}$$

Using these with equations (7.22) and (7.23)

$$\varepsilon = Sz \rightarrow z_1 = S^{\#}\varepsilon \tag{7.31}$$

Note S is not a square matrix, and ε does not contain information about derivatives. Thus z_1 does not fully represent z of equation (7.21) although we will still have m latent variables in Z_1. We cannot obtain all the variables in X from this equation. The issue analogous to before: the dimension of z is greater than u and $\tilde{x}$ combined, hence we cannot recover all the original information (excluding cases where they are strictly linear). What we left out in ε are the derivatives since in a state transition matrix, derivatives are computed based on previous states and are not known in advance. However, we can get approximate derivatives as follows. To get the entire

$$z_1 = A_v\tilde{x} + B_v u \tag{7.32}$$

where

$$S^{\#} = \begin{bmatrix} B_v & A_v \end{bmatrix} \tag{7.33}$$

where Bv and Av are the parts of $S^{\#}$ associated with the input and the state variables, respectively. Replacing z with z_1 in equation (7.24)

$$\dot{\tilde{x}} = Wz_1 \tag{7.34}$$

Substituting z_1 from (7.32)

$$\dot{\tilde{x}} = \tilde{A}\tilde{x} + \tilde{B}u \tag{7.35}$$

where

$$\begin{aligned} \tilde{\bar{A}} &= WA_v \\ \tilde{B} &= WB_v \end{aligned} \tag{7.36}$$

This equations gives us the well familiarized linear model of the state space form.

As with method 1, with no truncation applied to the square matrix M or T, this will produce unreliable results since WV^T and WU^T will be singular or close to singular based on properties of orthogonal matrices. We expect with a large enough data matrix, correlations between original state variables and the non linear auxiliary variables are captured sufficiently for an approximate system representation. We will use this model as a nominal or a base reference and then apply estimation techniques using a linear state observer (discussed in the next chapter) to incorporate non linearities. These non linearities can be then be used to develop a simplified control system.

The theoretical order of truncation can be adopted from [68]. It is given by

$$O = n_l + 2n_{nl} + r \tag{7.37}$$

The generalized system where the original state variables are measured and the non linear elements are estimated can be can be represented as follows:

$$\dot{\tilde{x}} = \begin{pmatrix} \dot{x} \\ \dot{\zeta} \end{pmatrix} = \begin{pmatrix} A_x & A_\zeta \\ J_x & J_\zeta \end{pmatrix} \begin{pmatrix} x \\ \zeta \end{pmatrix} + \begin{pmatrix} B_u \\ J_u \end{pmatrix} u \tag{7.38}$$

where y is the output vector- which is measured, e is the error between the estimated

and measured states; and L is the state observer gain to guarantee asymptotic stability in the region of operation. This is discussed in details in Chapter 7.

7.4 Practical Application to an UUV

We now apply the above methodology to our non linear single jet impinging robot system performing vertical motion towards or away from the ground. The specific application we will study is the micro UUV maintaining a constant height h_e while traversing an inspection surface. Control of h_e, the fluid bed thickness, is critical to certain inspection methods such as ultrasound. We will operate at the stable equilibrium point where forces are balanced. The UUV when perturbed can either move towards the ground, or away from it. While it is in a region where F_g (ground effect force) dominates, passive hydrodynamics will bring it back to its equilibrium position; however, it suffer a damped oscillation around the equilibrium. If however the body is perturbed into the unstable region (beyond the minima), it must be brought back to back to it's position. In both cases, a fast acting control system is required to quickly stabilize the UUV. Recovery speed is crucial for many inspection tasks to avoid losing knowledge of position on the target surface.

As described previously, the non linear dynamics results in a unique and challenging for modeling problem for analytical or data driven method. To summarize the complications:

1. highly non linear, non monotonic force
2. multiple equilibria (one stable, one unstable)
3. no well defined physical model for the phenomenon

We will use the data driven model of the previous section to represent the system dynamics over the entire operational region and estimate the non linear forces in order to develop a simplified control system.

7.4.1 Auxiliary variables for UUV model

As mentioned earlier, the auxiliary variables can be determined either via Bond Graph representation of the physical system, or by choosing functions of the state variables (higher order polynomials, for example) where linear combination are expected to reproduce non linear forces through a linear model. However, such additions result in an apparently meaningless augmented state in the linear model: it may work, but the terms have no clear physical interpretation. This is not a prohibitive disadvantage; indeed, the results can be recast into another state space where physical interpretation is possible. As shown in [68] the two non linear elements would be our auxiliary variables. Another way to look at it is, we chose to develop our model using the non linear forces, F_g and F_d, as such that the original state variables are represented linearly in the non linear space.

We have three objectives.

1. Derive an approximate linear state space model.
2. Estimate the non linear forces
3. Use the results of (2) in a simple controller

We begin with the underlying equation for the system

$$\begin{bmatrix} \dot{w} \\ \dot{h} \\ \dot{F}_g \\ \dot{F}_d \end{bmatrix} = \bar{\tilde{A}} \begin{bmatrix} w \\ h \\ F_g \\ F_d \end{bmatrix} + \tilde{B}u \tag{7.39}$$

The˜accents indicate the state transition matrix corresponding to the augmented system ($\tilde{x}$). And $\bar{\tilde{A}}$ is the data driven approximated value of the $\tilde{A}$ nominal or analytic matrix derived

directly from the non linear equation, and is exact to the non linear equation. The nominal $\tilde{A}$ matrix is a state dependent matrix as seen in equation (7.42) in a higher dimensional space for the original second order system. Let us now explain how we derive this.

Assume a fixed downward jet u_j and robot velocity small compared to the jet velocity, F_g is strictly a function of h while F_d is strictly a function of w. The robot is operating in the region $\phi(h,w)$. With this, we can analytically derive the $\tilde{A}$ matrix

$$\begin{aligned}
\dot{w} &= (F_g - F_d + u)/S_z \\
\dot{h} &= w \\
\dot{F}_g &= \frac{dF_g}{dh}\frac{dh}{dt} = \frac{dF_g}{dh}w \\
\dot{F}_d &= \frac{dF_d}{dw}\frac{dw}{dt} = \frac{dF_d}{dw}\dot{w} = \frac{dF_g}{dw}\frac{1}{S_z}(F_g - F_d + u)
\end{aligned} \tag{7.40}$$

which we can put in Jacobian form

$$\begin{bmatrix} \dot{w} \\ \dot{h} \\ \dot{F}_g \\ \dot{F}_d \end{bmatrix} = \begin{bmatrix} 0 & 0 & \frac{1}{S_z} & -\frac{1}{S_z} \\ 1 & 0 & 0 & 0 \\ \frac{dF_g}{dh} & 0 & 0 & 0 \\ 0 & 0 & \frac{1}{S_z}\frac{dF_d}{dw} & -\frac{1}{S_z}\frac{dF_d}{dw} \end{bmatrix} \begin{bmatrix} w \\ h \\ F_g \\ F_d \end{bmatrix} + \begin{bmatrix} \frac{1}{S_z} \\ 0 \\ 0 \\ \frac{dF_d}{dw}\frac{1}{S_z} \end{bmatrix} u \tag{7.41}$$

Suppose we can only measure the original state variables, then

$$C = \begin{bmatrix} 1 & 0 & 0 & 0 \\ 0 & 1 & 0 & 0 \end{bmatrix} \tilde{x} \tag{7.42}$$

When the parametric model is represented in a Jacobian form, a few things is noticed. We see 3 and 4 of $\tilde{A}$ are state dependent. They change at every operation point in $\phi(h,w)$. We also note, that row 1 and row 4 of the non linear matrix are collinear at any point

in ϕ when represented in such a parametric form and therefore brings us back to the question of redundancy as we introduced using the non linear spring example. The model in the parametric form is an approximate and simplified representation and is non linear, so traditional Jacobian method is not the best choice here. While good to keep in mind for a reference, concepts of observability, controllability for non linear model is different than that of a linear model. For our data driven model, we do not use any parametric model to compute the traditional Jacobian but avail the elements in the matrix directly from the data. To summarize,

The state derivatives in the linear model are given by

$$\dot{x} = A_x x + A_\zeta \zeta \tag{7.43}$$

And the linearized relation between the state variables and the non linear auxiliary variables (non linear forces) are given as:

$$\zeta = J_x x + J_x u + \zeta_0 \tag{7.44}$$

Then we have,

$$\dot{x} = A_x x + A_\zeta (J_x x + J_x u + \zeta_0) \tag{7.45}$$

For our data driven model, ideally we shouldn't use any parametric model to compute the traditional Jacobian like in equation (7.42) but avail the elements in the matrix directly from the data as in:

$$(J_x, J_u, \zeta_0) = \arg\min E[|\dot{x} - x|^2] \tag{7.46}$$

Equation (7.43) doesn't contain all the information about the non linearity- it gives an idea of the variation in the state variables as forces are varied. Adding the auxiliary

variables in the augmented system gives an additional perspective- essentially looking at the variation in the forces as the states are varied. The linearized relationship is not reversible for such highly non linear systems, rather they are complimentary. However, (7.42) is useful to have some approximated understanding of the system dynamics and interrelationships between different variables and for comparison at a particular operating point.

As seen in Figure (7-8), dF_g/dh is too non linear and is not even of constant sign over the operational region, being negative at the low h region (slope(1)), switching to positive at higher h (slope (2)), before dropping to negative again (slope (3)) beyond about a meter from the surface. Note also $\dot{F}_g$ is proportional to w but has no direct h dependence. This has implications in the covariance matrix, discussed next.

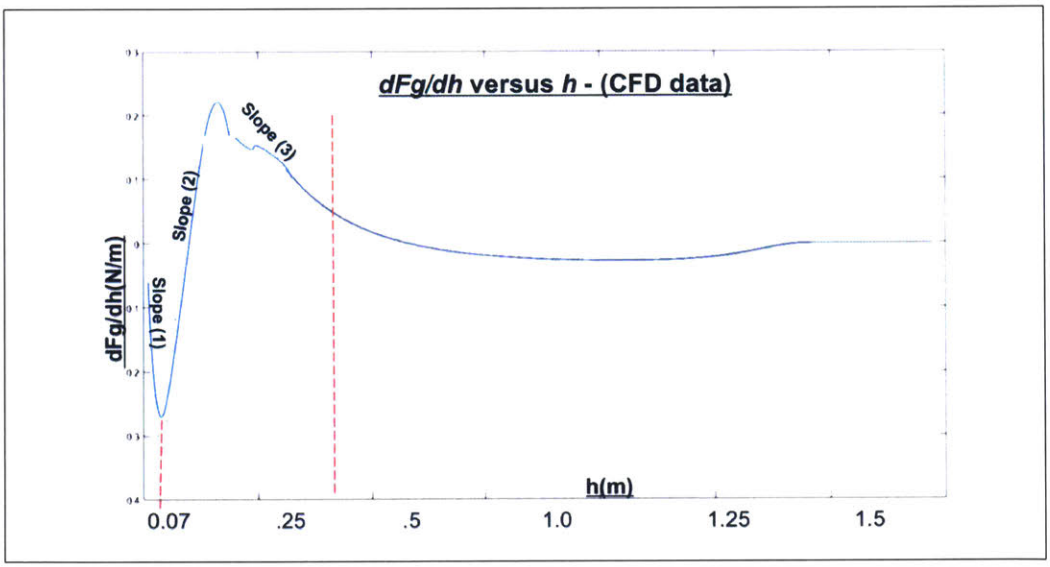

Figure 7-8: dF_g/dh shown as a function of h which is highly nonlinear. For control, the critical region is from $.07m$ to $.45m$ though we train unto 1.2m. Note the first slope change at minima at $h = .07$.

7.4.2 Data Generation

Our starting point is experimental data, e.g. the time response show in Figure (7-9). From this we establish a CFD (Computational Fluid Dynamics) model which matches our experiments, as shown earlier. It is computationally unrealistic to use the full CFD model to generate a large body of data: it is simply too slow. Therefore, we use the CFD results to create a simplified model in MATLAB. The MATLAB program implements $F_g(h)$ as a lookup table from the CFD results with cubic spline interpolation. $F_d(w)$ is based previously measured drag versus velocity. MATLAB's Ordinary Differential Equation (ODE) solver is used to determine the trajectory of the vehicle, i.e. h and w versus time, given forces $F_g(h), F_d(w), u(t)$.

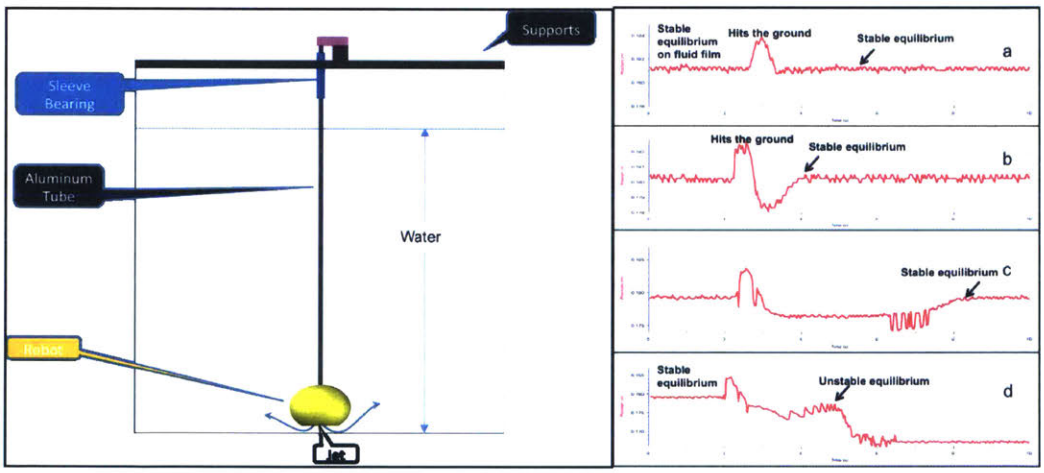

Figure 7-9: An Expertimental Setup (left) from which the force response is generated (right)

We use this MATLAB simulation to generate training data – used through the PCA to get state transition matrices – as well as test data. Recall each column of X contains the nine elements of the augmented state vector η which represent a column of the sample

data matrix X. Elements of η are enumerated below.

$$\begin{array}{llll} 1: u & & & \\ 2: w & 3: h & 4: F_g & 5: F_d \\ 6: \dot{w} & 7: \dot{h} & 8: \dot{F}_g & 9: \dot{F}_d \end{array}$$

Next X is reduced to a covariance matrix.

$$C = \frac{XX^T}{N} = \begin{bmatrix} \sigma_{uu} & \sigma_{uw} & \cdots & \sigma_{u\dot{F}_d} \\ \sigma_{wu} & \sigma_{ww} & \cdots & \sigma_{w\dot{F}_d} \\ \vdots & \vdots & \ddots & \vdots \\ \sigma_{\dot{F}_d u} & \sigma_{\dot{F}_d w} & \cdots & \sigma_{\dot{F}_d \dot{F}_d} \end{bmatrix} \tag{7.47}$$

where N is the number of samples in X.

We use two types of training data from which to create X.

- Method 1: **Grid** This is the simpler case. We select the independent variables u, w, and h independently to populate a fixed region of the u, w, h space. We then analyze F_g, F_d, and the derivatives algebraically, e.g. we use $\dot{F}_g = \frac{dF_g}{dh} w$ with dF_g/dh gotten as a numeric derivative from the tabulated data. Because instantaneous derivatives are used, results can be directly compared to classic linearization via a Jacobian. However, several real and relevant correlations are not captured in the covariance, as we shall explain below.

- Method 2: **Time Evolution**. As with the Grid method, we select initial values from a grid, but we run the simulation for a significant span of time: 10 seconds. An entry is made in X array every 0.1 seconds, resulting in 100 entries for each initial condition. Time Evolution better captures correlations inherent to the system dynamics. It is also more suited to real, experimental data which by it's nature

evolves with time. However, results are very different the classic Jacobian, making comparison to traditional linearization difficult.

For each, we study the affect range. We have also looked at the affect of data density: within any given range, and for either method, how the number data points changes the simulation. We took the expedient of generating data at high density and confirming that using 1/4 of the data gave equivalent results. (The use of 1/4 is tied to specifics of the code: it is simpler to reject half each in w and h.)

In addition to training data, we generate test data to validate the model. Test data is like the time-evolution training data, except it runs for hundreds of seconds and is *not* used to form the linear model. Figure (7-10) shows an example phase plot – height h versus velocity w – for test data and training data. Note in Figure (7-10b), with time the body has tendency to prefer certain areas more than others -as evident by the density variation - which follows the bimodal behavior of the non linear F_g curve. The test path (red) happens to follow this region here.

We wrote a software to enable creating unto 4 million data points in the operational region. The approximated $\tilde{A}$ matrix developed depends on many things:

1. Training types- grid or time evolved simulation (there are option to choose sub types in those)
2. Training Region
3. Subtraining region for specific problem
4. Constrains, and other specifications of parameters and variables
5. Number of auxiliary variables - if using individual forces or total force as a single variable

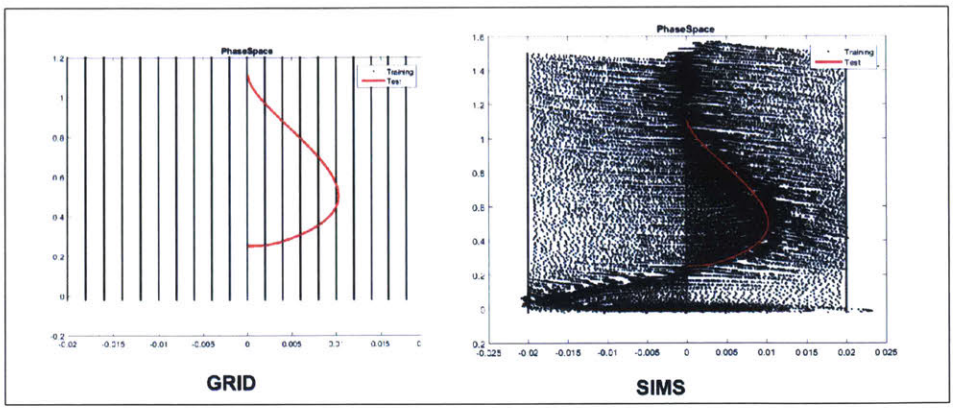

Figure 7-10: Left show grid type training and right shows time simulation type training. The red line shows the test path. Notice due to time evolution, there is a natural tendency of a time dependent system to reach steady behavior in a certain region. This region therefore is more densely populated than the other. The correlation might seem pseudo and not represented in a instantaneous equation, yet is important in the physical understanding of the system

The software works in generating a large data file in the region specified, which then can be used with different procedure to generate the state transition model. It has capabilities of using different offsets, adding new auxiliary variables as well as use a state estimator along with the model.

7.4.3 Covariance Matrix

Though we rely on data for modeling, we also emphasize an intuitive understanding of each step, even if only qualitative. Without this, we cannot say under what conditions our methodology works, and where it might fail. Therefore, here we analyze the expected elements in the covariance matrix based on our physical understanding of the system dynamics.

We start with the Grid data because it is amenable to analytic calculations. As a byproduct, we demonstrate it's problems and why we prefer the Time Evolution data.

In this method, since u, w, h are each chosen independently, they are statistically independent. Further, functions of h – such as $F_g, dF_g/dh$ – are independent of w and functions of w such as $F_d, dF_d/dw$. Since the covariance of independent variables is zero, and using $\dot{F}_g = w\frac{dF_g}{dh}$, $\dot{F}_d = \dot{w}\frac{dF_d}{dw}$, we get the following. (Note this is a symmetric matrix, we list only one of the two elements.)

- $\sigma_{uw} = 0 \Leftarrow w$ is independent of u
- $\sigma_{uh} = 0 \Leftarrow h$ is independent of u
- $\sigma_{uF_g} = 0 \Leftarrow F_g$ depends only on h, which is independent of u
- $\sigma_{uF_d} = 0 \Leftarrow F_d$ depends only on w, which is independent of u
- $\sigma_{u\dot{h}} = 0 \Leftarrow \dot{h} = w$ is independent of h
- $\sigma_{u\dot{F}_g} = 0 \Leftarrow \dot{F}_g$ depends only on h and w, both of which are independent of u
- $\sigma_{wh} = 0 \Leftarrow h$ is independent of w
- $\sigma_{wF_g} = 0 \Leftarrow F_g$ depends only on h, and h is independent of w
- $\sigma_{w\dot{h}} = 1 \Leftarrow \dot{h} = w$
- $\sigma_{hF_d} = 0 \Leftarrow F_d$ depends only on w, which is independent of h
- $\sigma_{h\dot{h}} = 0 \Leftarrow \dot{h} = w$ is independent of h
- $\sigma_{F_gF_d} = 0 \Leftarrow F_d$ depends only on w, while F_g depends only on h
- $\sigma_{F_g\dot{h}} = 0 \Leftarrow \dot{h} = w$ is independent of h, and F_g depends only on h

Two additional terms can be shown to be zero if the mean value of w – $\overline{w}$ – is zero.

- $\sigma_{h\dot{F}_g} = \overline{\left(h\frac{dF_g}{dh}\right)}\,\overline{w} = 0$
- $\sigma_{F_g\dot{F}_g} = \overline{\left(F_g\frac{dF_g}{dh}\right)}\,\overline{w} = 0$

Looking through the above list, we see that dependencies which are intuitively present are not captured by the covariance. For instance, it seems intuitively clear that $F_g > 0$ would tend to go with $w > 0$ – but in the grid method, there is no correlation between the two. Though it is seen that along with an appropriate estimator a model generated using grid works quite well, particularly cause its well understood and certain spurious computation errors can be identified and corrected, from state derivative and long term prediction using simply the state transition matrix- the system cannot do any reliable estimate of the non linear forces.Unfortunately, time evolved data does not have the simplicity required for analytic calculations. From derivative prediction it often yields better results, especially when compared to grid method. Along with an estimator though the particular model may provide very good non linear force estimate, it is highly sensitive to small perturbation in its elements or even to regions of sampling. Regional dependency for the net estimation of $\dot{F}_g$ and F_d is however shown in the next chapter as here we focus mostly on the fidelity of the state derivative prediction model.

7.5 Results and Analysis

In this section we will present the performance of the model in the three regions shown in Figure (7-11). We compare the two data generation models described earlier, as well as the region over which we operate and train. We systematically go through how we apply the theory previously described in this chapter to achieve an optimal linear model for our problem.

The regions in Figure (7-11) are defined by the sign of $F_g(h)$. Two of these regions we further sub-divide based on the sign of dF_g/dh.

- Region 1: $h < 0, F_g > 0$
- Region 2: $h > 0, F_g < 0$
  - Region 2a: $dF_g/dh < 0$
  - Region 2b: $dF_g/dh > 0$
- Region 3: $h > 0, F_g > 0$
  - Region 3a: $dF_g/dh > 0$
  - Region 3b: $dF_g/dh < 0$

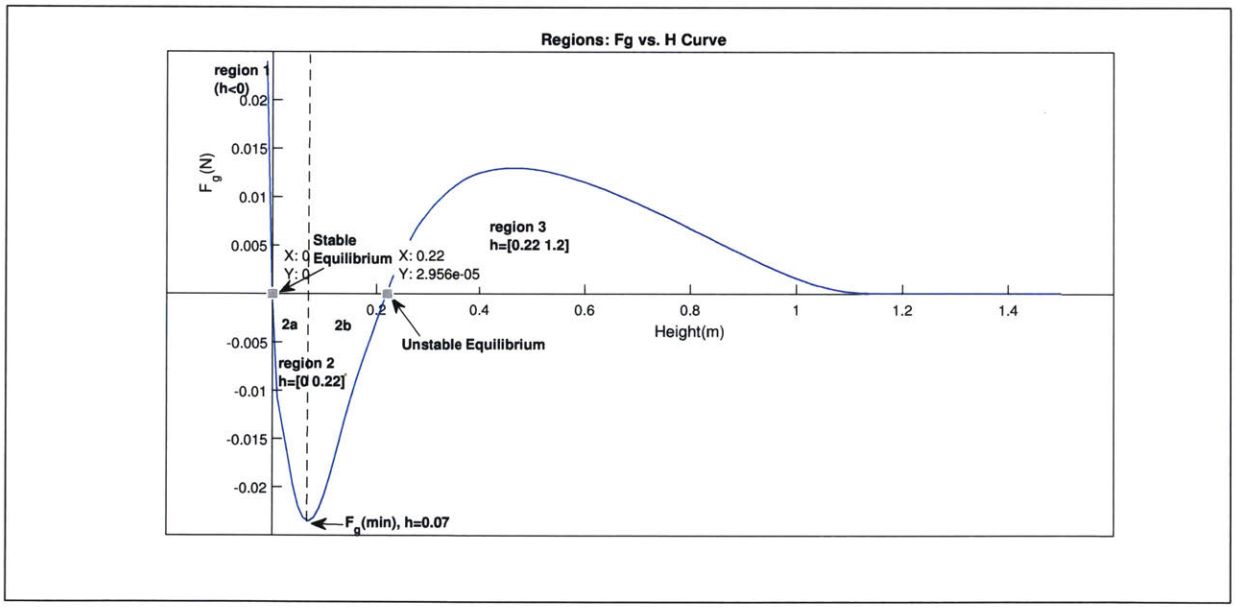

Figure 7-11: Force Regions in the F_g vs h curve

We use a sample space X of size 9×50000 points. We will show results using two cases: (a) linear drag and non linear ground force i.e. $n_{nl} = 1$.(b) both drag and ground force are non linear $n_{nl} = 2$. From equation (7.37) $O = n_l + 2n_{nl} + r$ we see which for a 1 non linear element (like linear drag and non linear ground force) comes out as 5, and for two non linear elements it is 7. This is verified quantitatively through RMS error analysis of the simulation data as well (see Figure (7-20). Another way to understand this is as follows. We have two linear relationships in the covariance matrix C: $\dot{h} = w$ and $\dot{w} = 1/(S_z)(F_g - F_d + u)$. Therefore, the rank of C should be 7 for perfect reproduction in the latent variable (LV) space. However, for most velocities in our operational range, a line is a reasonable approximation to $F_d(w)$; thus an order of 6 might suffice and in the 6^{th} order sufficient relationship of F_d and w is captured already. Figure (7-13a) shows the eigenvalues of the covariance matrix C. We find a large drop from the 6^{th} to the 7^{th} eigenvalue signifying that 6 latent variables are sufficient. Figure (7-13) shows how many relevant LVs are needed for the system representation. In figure (7-13d) - we see the original latent variables in $Z = T^T \eta$ and $Z_1 = S^{\#} \varepsilon$ differ since the derivatives are not included in ε. Figure (7-20) shows the RMS error of the estimate for various orders of truncation. Figure (7-21) uses poles of $\bar{\tilde{A}}$ to shows how stability changes with order of truncation. The anomaly at certain orders reflect singularities arising from pseudo inversions. There is a balance between avoiding large erroneous matrices from pseudo inversion versus performing at lower orders where we do not have enough information to reproduce the system.

Let us first generate the model using the grid method. The Covariance Matrix is as follows for a system with in ear drag and non linear ground force for example was found to be :

$C =$

```
1.0000   -0.0007    0.0018   -0.0000   -0.0007    0.3888    0.0067   -0.0013    0.3888
```

```
-0.0007    1.0000   -0.0000   -0.0000    1.0000   -0.8436    0.9999    0.0018   -0.8436
 0.0018   -0.0000    1.0000    0.3361   -0.0000    0.1253    0.0024   -0.0167    0.1253
-0.0000   -0.0000    0.3361    1.0000    0.0000    0.3709    0.0070   -0.0151    0.3709
-0.0007    1.0000   -0.0000    0.0000    1.0000   -0.8436    0.9999    0.0018   -0.8436
 0.3888   -0.8436    0.1253    0.3709   -0.8436    1.0000   -0.8381   -0.0032    1.0000
-0.0007    1.0000   -0.0000   -0.0000    1.0000   -0.8436    0.9999    0.0018   -0.8436
-0.0013    0.0018   -0.0167   -0.0151    0.0018   -0.0032    0.0018    1.0000   -0.0032
 0.3888   -0.8436    0.1253    0.3709   -0.8436    1.0000   -0.8381   -0.0032    1.0000
```

The eigenvalues of C are λ

```
4.6901
1.4913
1.1239
0.9986
0.6960
0.0000
0.0000
0.0000
0.0000
```

The truncation order of 5 is evident both via the eigen values and the figures below.

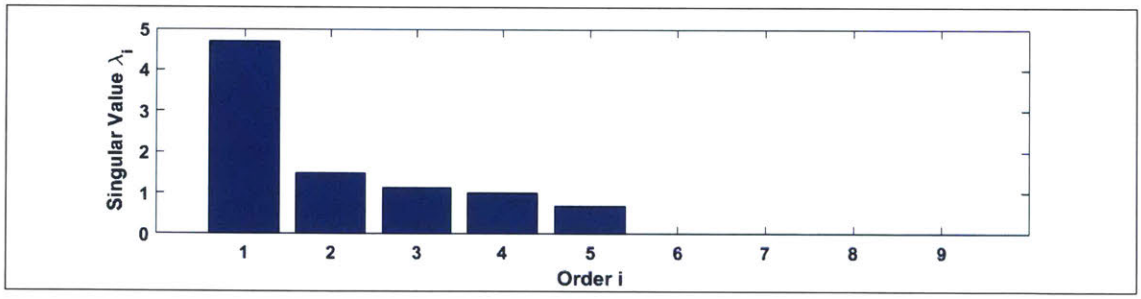

Figure 7-12: Singular Values of the system with only one non linear element F_g

The sub blocks of T are
$U =$

```
-0.0928    0.2940   -0.8408    0.0523   -0.2191
```

$V =$

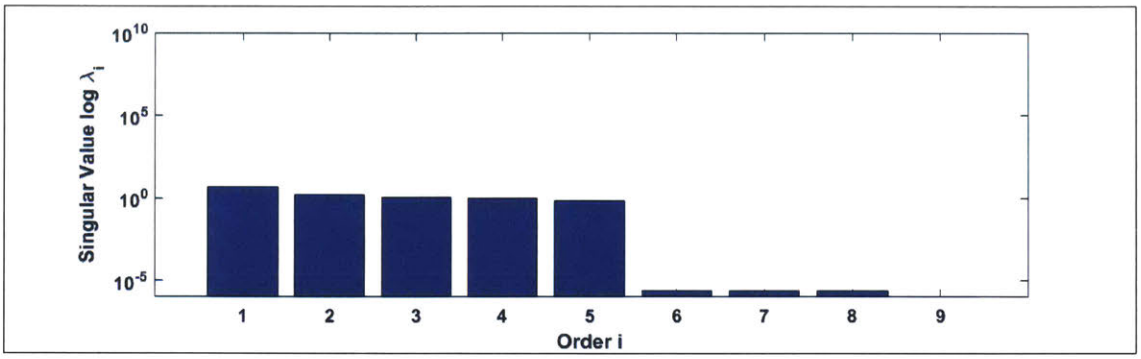

Figure 7-13: Log Plot of Singular Values of the system with only one non linear element F_g

```
 0.4428    0.2048   -0.1209   -0.0005    0.0637
-0.0383    0.5427    0.3855   -0.0409   -0.7444
-0.0918    0.6517    0.2442   -0.0483    0.6087
 0.4428    0.2048   -0.1209   -0.0005    0.0637
```

$W =$

```
-0.4435    0.1830   -0.1342   -0.0016    0.0870
 0.4428    0.2048   -0.1209   -0.0005    0.0637
 0.0020   -0.0393   -0.0712   -0.9966   -0.0109
-0.4435    0.1830   -0.1342   -0.0016    0.0870
```

So, we now have the approximated state transition matrix as:

$$\bar{\bar{A}} = \begin{bmatrix} -0.1556 & 0.0000 & 0.2490 & -0.1245 \\ 0.4922 & 0.0000 & -0.0000 & 0.3938 \\ 0.0005 & -0.0000 & -0.0008 & 0.0004 \\ -0.1945 & 0.0000 & 0.3112 & -0.1556 \end{bmatrix} \tag{7.48}$$

The analytic form has first two rows constant and given by:

$$\tilde{A}(\text{first two rows}) = \begin{bmatrix} 0 & 0 & \mathbf{0.2529} & \mathbf{-0.2529} \\ 1 & 0 & 0 & 0 \end{bmatrix} \tag{7.49}$$

The highlighted elements basically represent the inverse of the associated mass. Due to the linear relationship with drag, the confusion in the split — of $\tilde{\tilde{A}}$ is not unexpected. Since for linear drag $F_d = Z_{ww}w$ and $\dot{w}$ is essentially force per unit mass, has its estimation is split with both w and $Z_{ww}w$. Similar for $\dot{h} = w$ estimation- split between w and Z_{ww}. The result from simulation didn't show this splitting but the numbers there are much more of a blackbox to compare with the original model. Nevertheless with an appropriate state observer, the above model still estimates each of the forces quite well as will be seen in the next chapter. And we also have,
$\tilde{\tilde{B}}$ =

```
 0.2492
-0.0000
 0.0200
-0.0000
```

and we expect

$\tilde{B}$(first two rows) =

```
0.2582
   0
```

Now for two non linear forces, we get the following.

The correlations between the different variables in η from our data samples taken over the entire operational region for the time evolved method Figure(7-17) respectively. Note the correlations in method (2) that do not show up in method (1). However, the resultant matrices from method 1 is readily understood since the grid method follows the physical

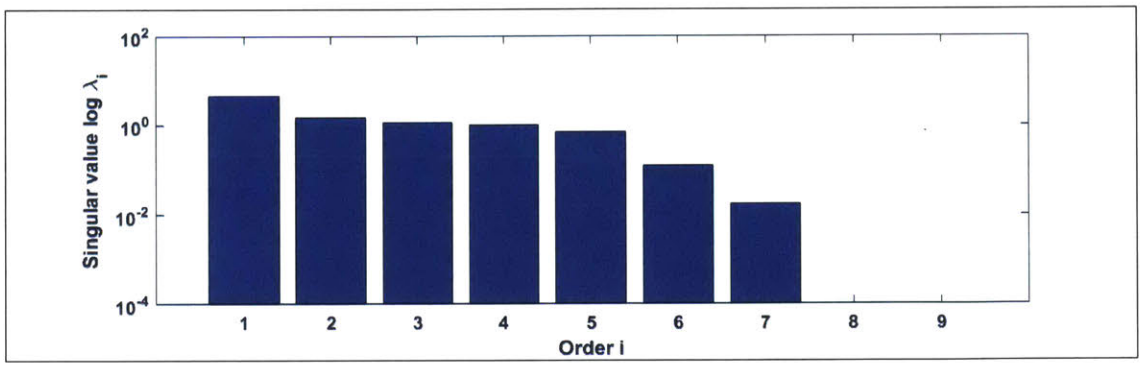

Figure 7-14: Singular Values of the system with two non linear elements F_g and F_d

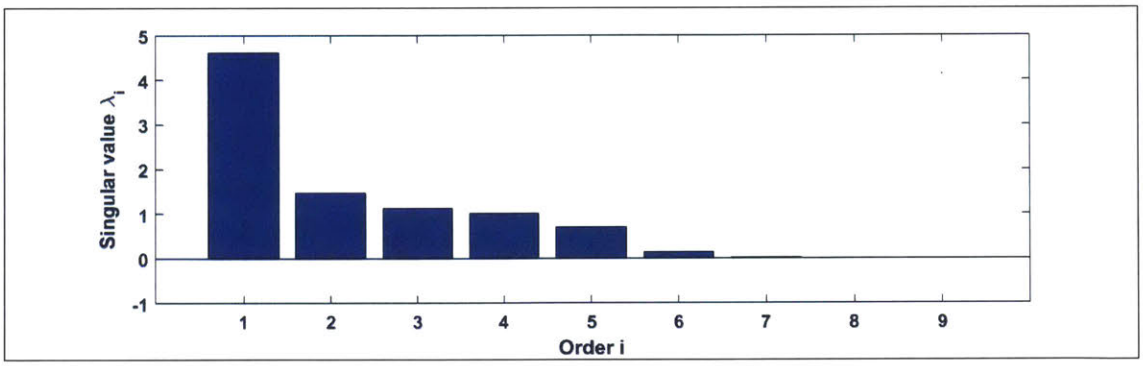

Figure 7-15: Log of Singular Values of the system with two non linear elements F_g and F_d

model in equation (18) more accurately. A sample $\bar{\bar{A}}$ and $\bar{\bar{B}}$ from grid data:

$$\bar{\bar{A}} = \begin{bmatrix} 0.0000 & -0.0000 & \mathbf{0.2529} & \mathbf{-0.2529} \\ \mathbf{1.0000} & \mathbf{0.0000} & \mathbf{0.0003} & \mathbf{-0.0003} \\ 0.0411 & -0.0013 & -0.0236 & 0.0275 \\ 0.8737 & 0.0001 & 0.3760 & -1.3748 \end{bmatrix} \qquad \bar{\bar{B}} = \begin{bmatrix} \mathbf{0.2528} & 0.0003 & -0.0042 & 0.3778 \end{bmatrix}$$

we see (highlighted elements above) $1/S_z = 0.2529$ between $\dot{w}$ to F_g, F_d, u; $\dot{h} = w$. For comparison, training with time evolved data yields

$$\bar{\bar{A}} = \begin{bmatrix} 4.0987 & -0.0109 & -0.1338 & -5.2921 \\ 1.1599 & -0.0004 & -0.0026 & -0.2089 \\ 0.2634 & -0.0007 & 0.0085 & -0.3632 \\ 6.3350 & -0.0159 & -0.5655 & -7.6784 \end{bmatrix} \qquad \bar{\bar{B}} = \begin{bmatrix} 0.1024 & 0.0076 & 0.0098 & 0.0898 \end{bmatrix}$$

None of the elements have physically interpretable values. (Both examples come from training for $0 < h < 1\text{m}, |w| < 0.03\text{m/s}$.)

Observed Correlations in an Unforced System

We will first try to get an intuitive and physical understanding of this regional dependency of the ground effect force. For purpose of inspection, the goal is a precisely controlled height as the body moves across the target surface. Therefore, we focus on behavior relevant to staying at, or returning to, the stable equilibrium point.

Imagine an unforced system with constant jet force F_j stationary at the stable equilibrium i.e. $h = 0, w = 0$ where all forces are balanced. Due to some perturbation, it is displaced to, say, $h = .04m$ where it comes to a momentary halt. Starting at $h = .04, w = 0$, the body gets sucked by the Venturi effect back to the equilibrium. Therefore, the velocity here is

negative. Conversely, if it was pushed down towards the target surface, i.e. into Region 1, the force is repulsive (positive), again pushing the robot back toward the equilibrium. The Figure (7-16) system shows this phenomenon, the arrows along the trajectory showing the direction of motion if the body started at those initial conditions.

Using analogous reasoning for the other regions, we expect the following for the signs of the various elements of η as mentioned in the table.

	Region 1	Region 2a	Region 2b	Region 3
w	+	−	−	+
h	−	+	+	+
F_g	+	−	−	+
F_d	−	+	+	−
$\dot{F}_g$	−	+	+	−
df_g/dh	−	−	+	+

Table 7.1: Unforced System Sign Relationships in an Undriven System. Sign relationships between variables in the operation region $\phi(h,w)$ of the F_g vs. H curve.The initial condition is set as [w=0, h=H] where H is varied along the curve till 0.5m. This demonstrates the natural behavior of the body under the effect of the complex non linear force. The sign correlations are captured more distinctively in time evolving simulations which helps to establish causal relationships between variables not obvious in the grid method

External perturbation or initial velocity may cause the body move in a manner inconsistent with this table and the A matrix may not reflect the unforced behavior. We minimize this by using maximum RMS value of the excitation input $\sigma_u \lesssim F_g$ (as in example 2 earlier), and for the time-evolved data, starting at rest, i.e. $w(t=0)=0$, but allowing w to change over time. The latter is, of course, not an option for grid data where there is no evolution over time. Resulting corrolation plots are shown in Figures (**??**)and (7-17). Note in particular that for the grid data, $\dot{F}_g$ (middle row of plots) shows no corrolation with h or F_g, whereas

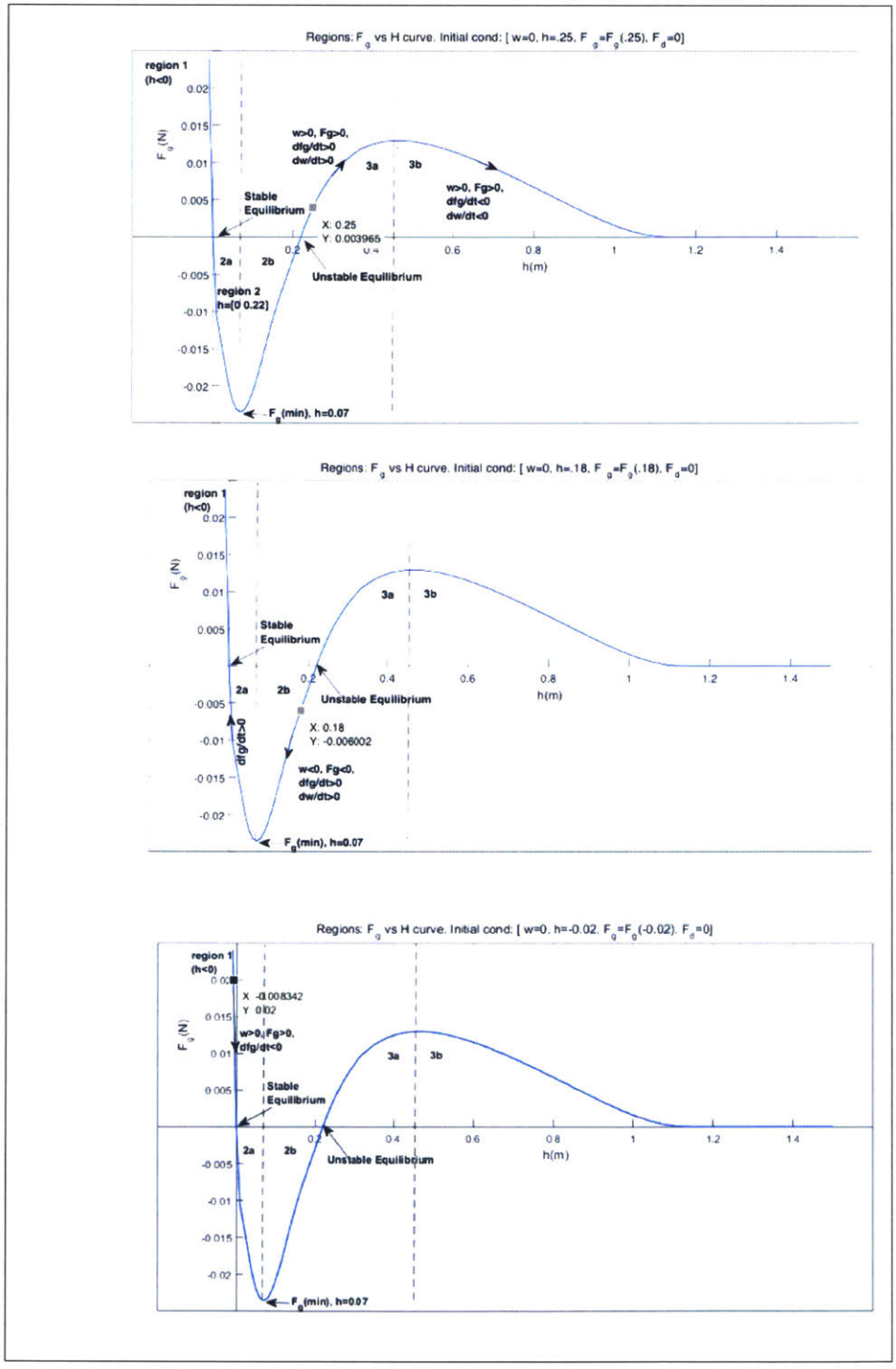

Figure 7-16: Observed Correlations in the different regions of the "Fg vs. H" curve of an unforced system

The figure shows the signs of different variables when starts at 3 different initial points. Top: Initial $[h = 0.25, w = 0]$ - body experiences positive F_g, positive w and positive $\dot{F}_g$ along this trajectory. Middle: [h=0.1, w=0], F_g, w both remain negative here till $h = 0$ though $\dot{F}_g$ changes signs. Bottom, [h=-0.03, w=0], F_g, w positive, $\dot{F}_g$ is negative.

there is a correlation in the time evolved data.

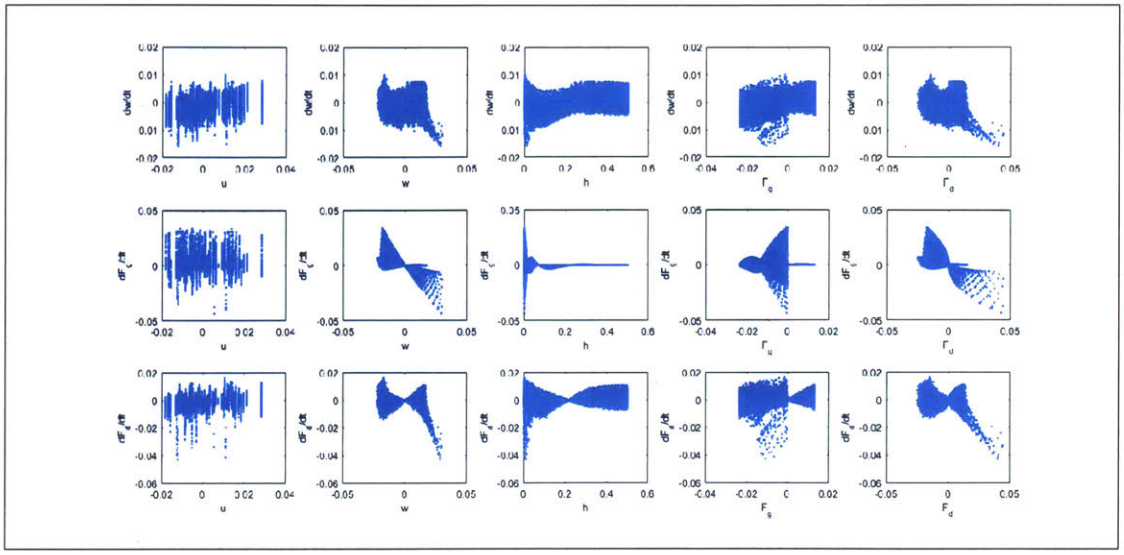

Figure 7-17: Example of Correlation plots for time-evolved data using $0 < h < 1$m and $|w| < 0.03$m/s

It can be said, more data is does not always mean better prediction. Or, exciting the entire entire operational region equally and sufficiently may not always be ideal. Biasing region or tweaking the excitation input may be necessary depending on the estimation goal. In our case, that was to ensure we capture the non linear effect prominently. Two kinds of phase space plot for biased and high density sample space are shown in Figure (7-18).

7.6 Unforced System Response

Example 1

In our first example, we use grid training data with $\sim 500,000$ entries uniformly populating $-0.03 < h < 1.3$m and $|w| < 0.3$. For this example, the generated data used excitation

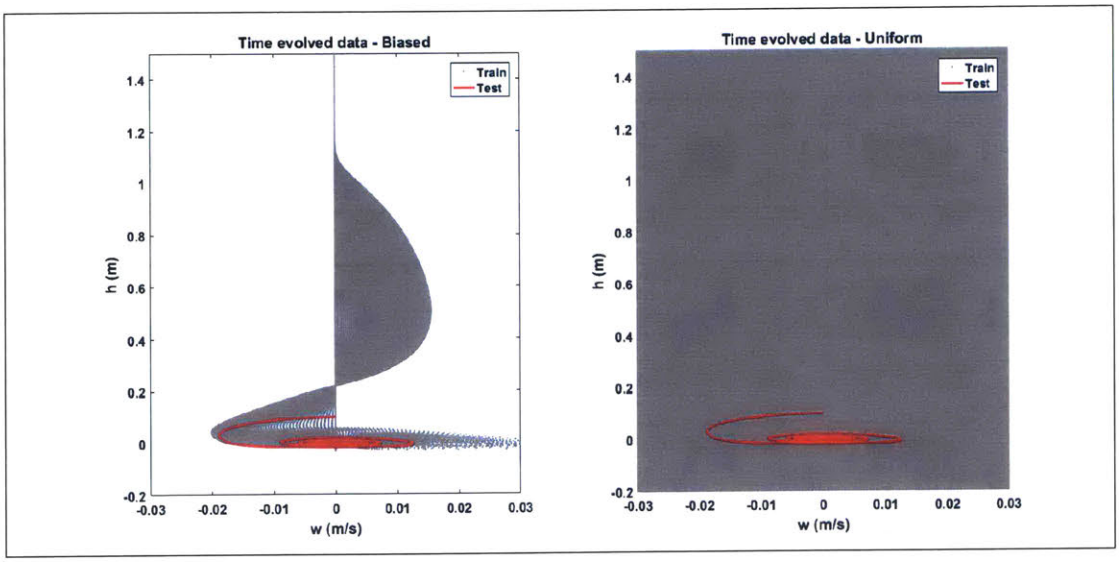

Figure 7-18: Left: Biased Data exciting only in the non linear ground effect region Right: High Density Data that has equally filled the entire operational space. Performance of the biased data space for non linear auxiliary state derivative estimation was found to be better than the high density sample space for the given initial conditions of the unforced system. The system trajectory is shown in red

input u as a Gaussian pink noise with width . Mean values were subtracted in the PCA, i.e. the PCA used mean-centered data. For two non linear elements we use a 6th order truncation as explained previously. For the test, we start in region 2b: initial point $[h = 0.1\text{m}, w = 0\text{m/sec}]$ and no external force. The slope df_g/dh is positive but the body experiences a negative ground force and, in the absence of external forces, is drawn to the negative slope region (2a) where it is hydrodynamically stable and settles into the equilibrium due to hydrodynamic damping. The damped oscillation is well reproduced.

However, (**??**d) shows an offset in $\dot{F}_d$. The standard $\dot{x} = Ax + Bu$ assures $\dot{x} \to 0$ for $u = 0, x \to 0$. But mean-centering in the PCA changes this to

$$\dot{x} - \bar{\dot{x}} = A(x - \bar{x}) + B(u - \bar{u}) \tag{7.50}$$

Thus the estimation of $\dot{F}_d$ can – and in this case, does – have an offset. The offset is due to approximation or modeling error or introduction of spurious elements due to computational error. We talk about it elaborately in Chapter 7. Such errors are more readily identified in the models generated using the grid method than the time evolved model due to its black box nature.

Positive Slope Region

Our primary focus is the equilibrium at $h = 0$, i.e. region 2a of figure (7-16). However, we need to be able to return to this region if perturbed. In region 2b, natural hydrodynamic suction will return the body to region 2a, but we would like to make that as rapid and smooth as possible. From region 3, the body must be actively forced back to region 2b.

7.7 Limitations and Variations of the model

This chapter described and tested a method of creating a linearized state transition matrix for a highly complex non linear dynamical system. The key limitations and observations to keep in mind are as follows

1. The process for gathering amd using data samples may have large impact on the results

    - Correlations which develop over time can contribute important information, i.e. the length of each data sample(or simulation run) is relevant.
    - The range of data used for training may need to be limited to the most critical region of operation

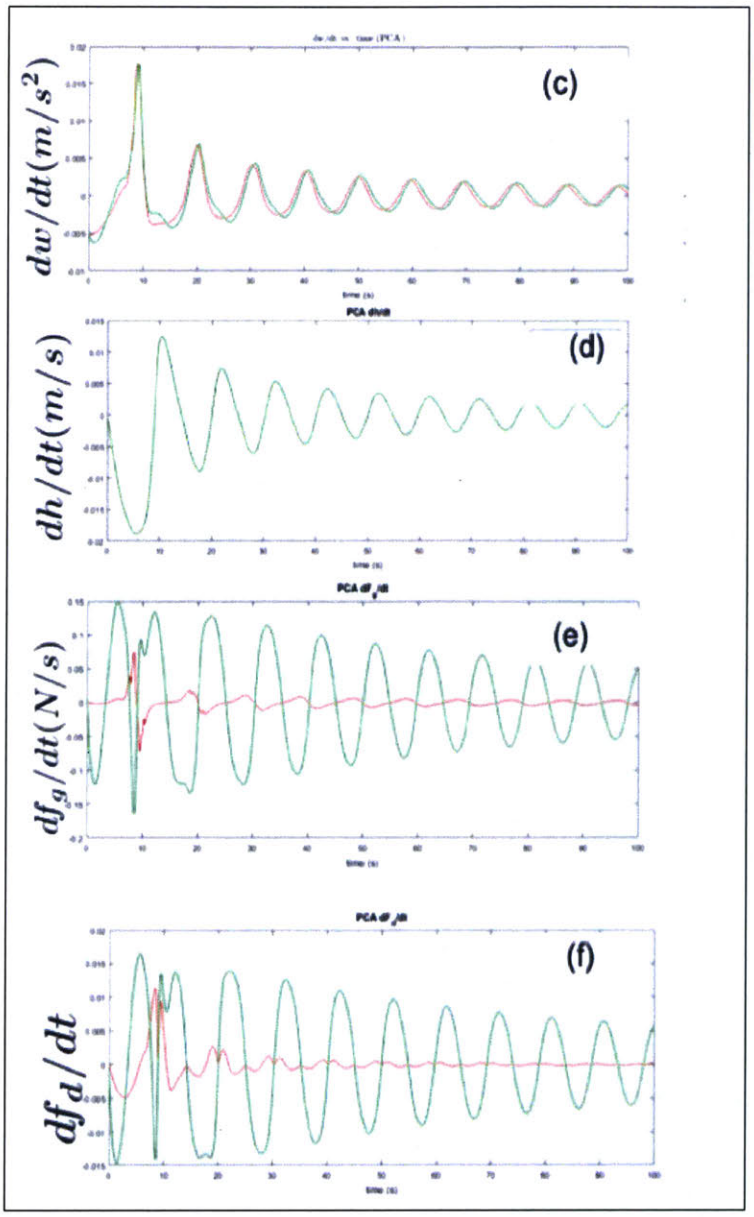

Figure 7-19: Example 1: Body starting at h=0.1m, with no external force. We plot the first 100 seconds time derivative

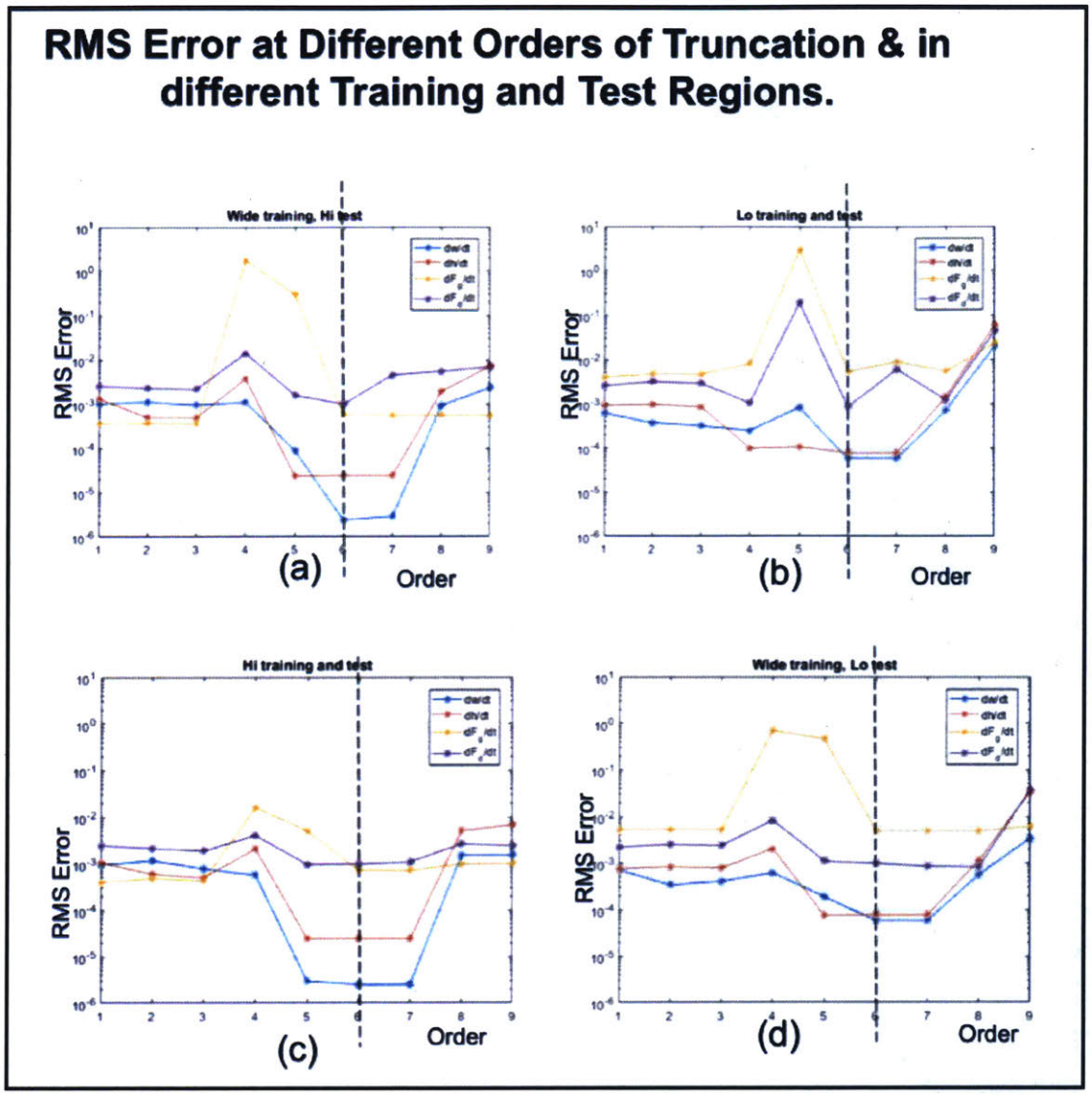

Figure 7-20: RMS Error of state derivatives at Different Orders of Truncation for a system with 2 non linear elements: From theory, we calculated the required order to be 7. Note 6th and 7th order seems to be optimal truncation order for minimizing the net RMS error of the augmented state vector and from computation, 6th was sufficient for the system.

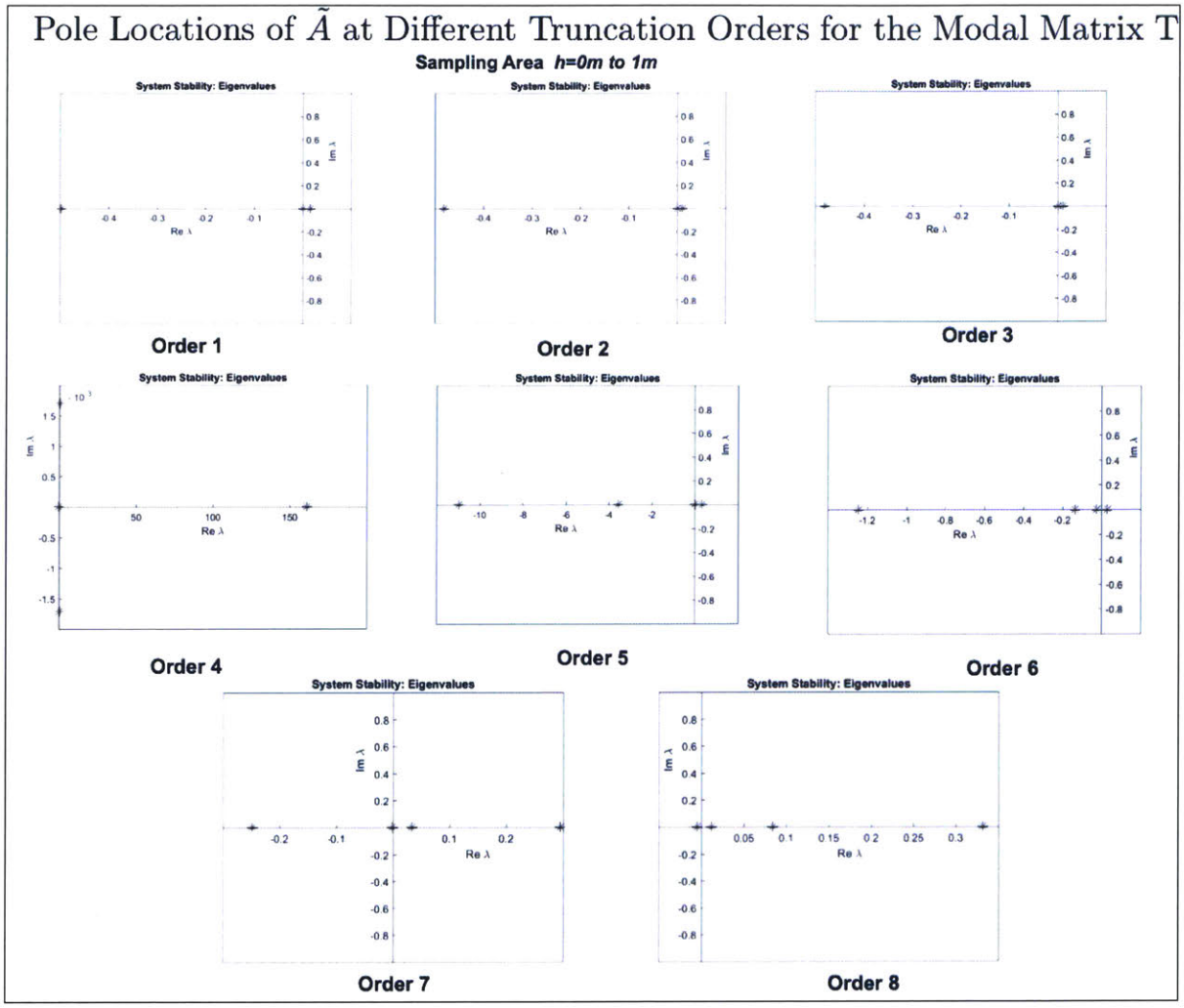

Figure 7-21: Pole location at different order of truncation of T. Note, higher order capture instability of the unstable region of force fields and the poles shift to the right plane. Also note, the anomaly at 4th and 5th order where W and S becomes a square matrix

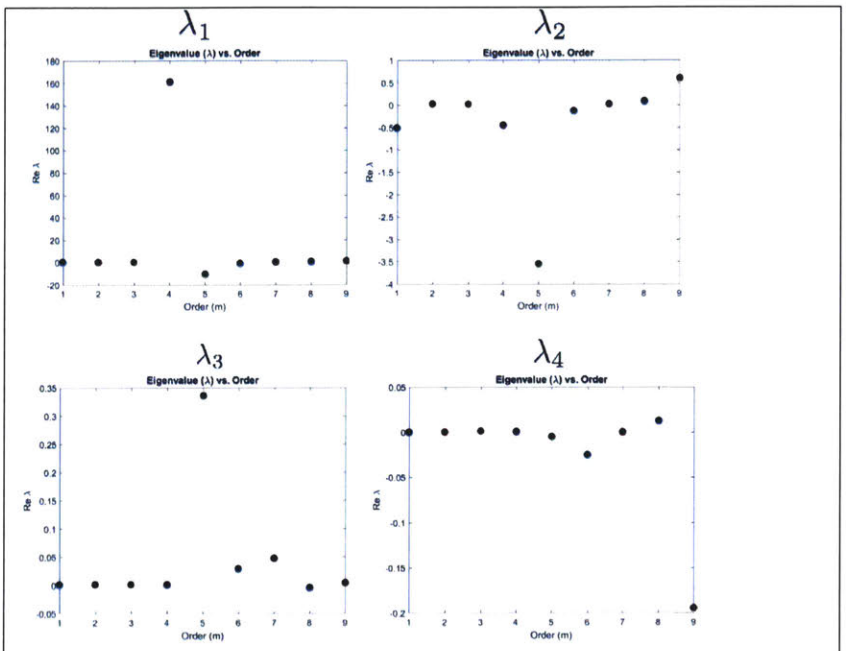

Eigen Values of $\tilde{A}$ vs truncation order of T for wide region training

Figure 7-22: How individual eigen values of the $\bar{\tilde{A}}$ matrix varies with order- notice anomaly at 5th

2. Though an exact linearization method is proposed, it suffers limitations from and rank deficiency and the need for a pseudo inverse. A correct truncation order and an optimal correction must be determined to minimize this problem.

3. Increasing the number of auxiliary variables can improve modeling. We illustrated this below using dF_g/dh as a potential additional auxiliary variable to better estimate $\dot{F}_g$.

4. A-priori knowledge of the system – in our case, for example, that F_g is a function only of h – can be used to estimate and correct for biases.

5. Multiple complex non linear forces make the problem much more challenging. For many practical purpose of control, we only need total force, which greatly simplifies the problem.

Point 3 above is illustrated here. The foremost challenge in obtaining F_g is that the dependence of $\dot{F}_g$ on h is not well represented in the resultant $\bar{\bar{A}}$ matrix. This is somewhat improved by using time evolved data, but the relationship as captured by the covariance remains weak.

The problem here is that $\dot{F}_g = \frac{dF_g}{dh}w$, i.e. is the product of a function of only h with a function of onlyu w. Thus it does not have a strong corrolation with either, and particularly not with h. One solution to this would be to estimate dF_g/dh instead of $\dot{F}_g$, and similarly dF_d/dw instead of $\dot{F}_d$

$$\begin{pmatrix} \frac{dF_g}{dh} \\ \frac{dF_d}{dw} \end{pmatrix} = \begin{pmatrix} G \end{pmatrix} \begin{pmatrix} w \\ h \\ F_g \\ F_d \end{pmatrix} \tag{7.51}$$

$$\begin{pmatrix} \dot{w} \\ \dot{h} \end{pmatrix} = \begin{pmatrix} F \end{pmatrix} \begin{pmatrix} w \\ h \\ F_g \\ F_d \end{pmatrix} + \begin{pmatrix} B \end{pmatrix} \tag{7.52}$$

We can get F and G using the same data driven PCA method described. Then we can construct a linear model with the state transition matrix.

$$\begin{bmatrix} \dot{w} \\ \dot{h} \\ \dot{F}_g \\ \dot{F}_d \end{bmatrix} = \begin{bmatrix} \cdots & F(1,:) & \cdots & \cdots \\ \cdots & F(2,:) & \cdots & \cdots \\ \frac{dF_g}{dh} & 0 & 0 & 0 \\ 0 & 0 & \frac{1}{S_z}\frac{dF_d}{dw} & \frac{1}{S_z}\frac{dF_d}{dw} \end{bmatrix} \begin{bmatrix} w \\ h \\ F_g \\ F_d \end{bmatrix} + \begin{bmatrix} B \end{bmatrix} u \tag{7.53}$$

We find this performs somewhat better than the previous method. As written, we end up with an A matrix dependent on $dF_g/dh, dF_d/dw$, which changes with time as the body moves – that is, with a time-dependent system. Instead, we would need to be incorporate $dF_g/dh, dF_d/dw$ as additional auxiliary variables. Alternatively, we can add higher order polynomials, e.g. implement F_g as in eq (7.6)

$$F_g(h) = u_j[\alpha h^2 + \beta h + \gamma] + Z_{ww} w|w| + u_j]$$

7.8 Conclusion

This chapter described a novel method of data driven formulation of a linear model for non linear systems. We used simulation data for our tests, but the methodology is well suited to use with experimental data. We applied the method to a body under the influence of ground effect forces resulting in a multi equilibria dynamical system. We have extensively

discussed how the performance depends on sampling method, definition of the covariance matrix, and truncation of latent variables. We encountered and explored limitations in forming a pseudo inverse. Despite these limitations we demonstrated results superiot to traditional TS, especially in cases where no analytic representation of the system is available.

In the next chapter we will start with this model as a nominal system, augment it with a state observer, and develop a robust control technique with online estimation and correction of the nonlinear forces. In this chapter, to study the capabilities of the algorithm, we retained two non linear forces. However, the controller cares only about the total force compensation. Non linear forces can be summed and estimated as a single non linear force, greatly simplifying the observer and controller.

Chapter 8

Estimator Design and Analysis

8.1 Introduction

In Chapter 6 we proposed a new method of forming a data driven linear state space model and showed its application in our multi equilibria, non linear dynamical system. However the true effectiveness of this model is demonstrated only when integrated with a state estimator. For non linear auxiliary state variables, the linear model has limitations in making long term predictions due to accumulation of errors in derivative estimates. Previous research has been done on estimation of a single, lumped non linearity. Some work has been done in estimating independent perturbations; such problem formulations are seen in disturbance rejections and systems suffering sudden dynamical changes. Different fields deal with the problem with their own approach – e.g. using Model Predictive Control (MPC), Fault Tolerant Control (FTC), or Adaptive Control [73], [74],[75].

Our problem is unique in a few ways. The non linearities are state dependent and an *a priori* accurate model of the physical system is unknown. So the nominal linearized model is developed using a data driven method. Unlike some of the other methods, we

establish the dynamics between these non linear elements and the state variables. The original linearized model (i.e., the state transition matrix) is constant: it does not change during the operation. We estimate the non linearity and compensate for it at every step via our control input.

The work presented here demonstrates an appropriate state observer for a data driven linearized model which gives us a precise estimate of *multiple* non linear forces. Essentially, we develop a much more unique and powerful tool than is currently available to separately estimate multiple non linear elements acting on a dynamical system. The simplified linear model from Chapter 6 is used as the starting point to design an estimator for non linear forces. Assuming we can measure the original state variables (with negligible error), we focus on the estimation of individual auxiliary variables with no direct measurement. The nominal state transition matrix derived from our data driven method, if chosen appropriately, provides the relationship of non linear forces with each other as well with state variables. Inaccuracies are corrected by a state estimator using deviation between predicted and measured state variables.

We will use the covariance and PCA method described earlier. This cannot fully represent the non linearities. The nature of the errors depends on the choice of auxiliary variables, the offset around which the covariance is measured, and the choice of training data. There is further the choice of how to propagate errors: (1) using estimated state and auxiliary variables from the linear model; or (2) using measured state variables and estimated non linear forces for state update and the estimated state variables from the linear model for error propagation. We will use the method (2) .The choice does not substantively modify the observer, the formulation of which is similar to that of a reduced order observer, except that the non linear forces are not fully independent states.

We show the design of the estimator both in the original augmented space as well as in the the latent variable (LV) or z space. The original and auxiliary states are rotated to form

LV space; linear combination of the original and auxiliary states occur in each element of LV space, and a reduced number of variables in LV space can fully capture the behavior of the system. LV space is particularly useful when a large amount of data and multiple non linearities necessitate dimensionality reduction. For the simple second order system, that is not the case. None the less, the general procedure for designing an observer in LV space is covered, both to assist in future generalization of this work, and as an alternative perspective on error propagation and convergence of the original and auxiliary states.

Convergence criterion for the observer is discussed. Online estimation of auxiliary variables are then used in an adaptive controller to compensate for non linearities and ensure the system can be controlled against external perturbations. We note rotation does not alter the norm of vectors, therefor stability in z space assures stability in original augmented space, and similarly for convergence. The entire closed loop system with an estimator based on the data driven model is shown in the Figure (8-1).

The novelty of the method lies in the fact that even an inaccurate or uncertain state matrix derived from data, with little knowledge of the true physical model, is sufficient for intrinsic robustness in terms of stability and performance. Though the method will been explained for a simple system with two non linear forces, its true effectiveness is demonstrated when considering large amounts of data and a system with multiple non linearities. This is where dimensionality reduction capability of PCA surpasses other data fitting techniques.

Though PCA or other methods may give us a state transition matrix which when augmented with a state estimator can give us satisfactory estimations of the unknown non linearities, an important requirement is to have some means of evaluating the goodness of the model. Since our intent is a model which can cover a wide range of conditions with multiple non linearities, traditional robustness analysis with a well defined nominal or reference requires modification. One approach is that the true non linear model is taken as

the nominal which is represented as a state dependent varying matrix; a second approach is to consider an already derived data driven matrix as the nominal and analyze sensitivity to uncertainties in its elements. The last part of the chapter lays down some observation based hypotheses and metrics for evaluation of a data driven model to ensure asymptotic stability and convergence when used along with an estimator.

The mathematical tools used in the chapter for developing the estimator are along the lines of traditional state observer model [76] with a slight deviation in the approach of error propagation and state updates. This data driven linearization approach, integrated with a state observer in the latent variable space, is a simplified yet powerful approach to dealing with a dynamical system with multiple non linearities and modeling uncertainties. This chapter is the culmination of this doctoral research thesis which revolves around control of a micro UUV subject to complex, poorly understood, non linear hydrodynamic force.

8.2 Auxiliary State Estimator Theory

In Chapter 6 we saw an augmented state space model in a higher dimensional space is given by

$$\tilde{x} = \begin{pmatrix} \dot{x} \\ \dot{\zeta} \end{pmatrix} = \begin{pmatrix} A_x & A_\zeta \\ J_x & J_\zeta \end{pmatrix} \begin{pmatrix} x \\ \zeta \end{pmatrix} + \begin{pmatrix} B_u \\ J_u \end{pmatrix} u \tag{8.1}$$
$$y = C_x x$$

where $x \in \Re^{n_l}$ is the original state variables, $\zeta \in \Re^{n_{nl}}$ is the auxiliary state variables containing the non linear elements, $u \in \Re^r$ is the input vector, $y \in \Re^p$ is the output vector, and $\tilde{x} \in \Re^l$ where $n = n_l + n_{nl}$.

The analytic form is a parametrically varying non linear matrix in $\phi(h,w)$ since the

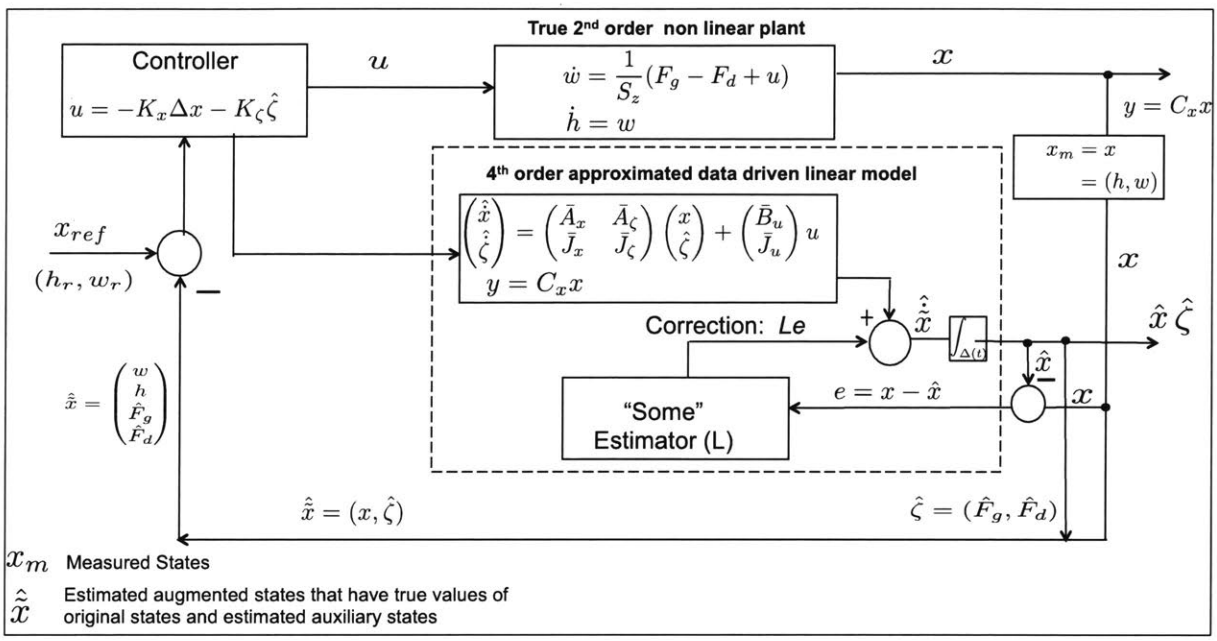

Figure 8-1: Data driven closed loop model of a 2nd order non linear plant with an estimator for non linear forces

non linear derivatives are state dependent. In a practical application, the original state variables, x, are measured. So we assume we know the true value of x but have no direct measurement of auxiliary state variables (the non linear forces in our case). Thus x is called the available signal, ζ the unavailable signal, and the output matrix C_x is not full rank. In our particular application, the augmented state space system has 4 state variables of which only two – height (h) and velocity (w) – can be measured and are thus available; while the ground effect force F_g and drag force F_d cannot be measured and are unavailable. Our goal is to estimate the unavailable signals from the available ones using a robust estimation technique. We see that $\begin{pmatrix} A_x \\ J_x \end{pmatrix} x$ is associated with available signal x and $\begin{pmatrix} A_\zeta \\ J_\zeta \end{pmatrix} \zeta$ with the unavailable signal ζ. In case of the micro UUV, we have

$$x = \begin{pmatrix} w \\ h \end{pmatrix} \quad \zeta = \begin{pmatrix} F_g \\ F_d \end{pmatrix} \tag{8.2}$$

$$\tilde{x} = \begin{pmatrix} w \\ h \\ F_g \\ F_d \end{pmatrix} \tag{8.3}$$

The analytical constant part of the system model (the corresponding states are measured or known) is

$$\begin{pmatrix} \dot{w} \\ \dot{h} \end{pmatrix} = \begin{pmatrix} 0 & 0 \\ 1 & 0 \end{pmatrix} x + \begin{pmatrix} \frac{1}{S_z} & -\frac{1}{S_z} \\ 0 & 0 \end{pmatrix} \zeta + \begin{pmatrix} \frac{1}{S_z} \\ 0 \end{pmatrix} u \tag{8.4}$$

The analytical parameter varying part of the system model is

$$\begin{pmatrix} \dot{F}_g \\ \dot{F}_d \end{pmatrix} = \begin{pmatrix} \frac{dF_g}{dh} & 0 \\ 0 & 0 \end{pmatrix} x + \begin{pmatrix} 0 & 0 \\ \frac{1}{S_z}\frac{dF_d}{dw} & -\frac{1}{S_z}\frac{dF_d}{dw} \end{pmatrix} \zeta + \begin{pmatrix} 0 \\ \frac{dF_d}{dw} \end{pmatrix} u \tag{8.5}$$

which can be written as

$$\dot{x} = A_x x + A_\zeta \zeta + B_x u \tag{8.6}$$

$$\dot{\zeta} = J_x x + J_x \zeta + J_u u \tag{8.7}$$

A full state estimator model can be constructed as follows

$$\dot{\hat{\bar{x}}} = \bar{\bar{A}}\hat{\bar{x}}(t) + \bar{\bar{B}}u(t) + Le \tag{8.8}$$

$$e(t) = x_m(t) - \hat{x}(t) = x(t) - \hat{x}(t) \tag{8.9}$$

$$\hat{\zeta}(t) = \hat{\zeta}(t-1) + \Delta\hat{\zeta}(t) \tag{8.10}$$

where

$$\bar{\bar{A}} = \begin{bmatrix} 0 & 0 & \frac{1}{S_z} & -\frac{1}{S_z} \\ 1 & 0 & 0 & 0 \\ J_{x_{11}} & J_{x_{12}} & J_{\zeta_{11}} & J_{\zeta_{12}} \\ J_{x_{21}} & J_{x_{22}} & J_{\zeta_{21}} & J_{\zeta_{22}} \end{bmatrix} \tag{8.11}$$

$$\hat{\bar{x}} = \begin{bmatrix} w_m \\ h_m \\ \hat{F}_g \\ \hat{F}_d \end{bmatrix} \tag{8.12}$$

where $x_m = (w_m, h_m)$ are the measured values of the states such that $w_m(t) = w(t)$

and $h_m(t) = h(t)$. Therefore the error propagation through $\hat{\bar{x}}$ is the contribution of the approximated J_x and J_ζ.

Note $\hat{}$ denotes estimated variables, and $\bar{}$ denotes the linearized approximated matrix (or matrix sub blocks) from the data driven method. $L \in \Re^{l \times n_l}$ is the estimator gain and $e(t) \in \Re^{n_l}$ is the error.

Estimator convergence is guaranteed if $(\bar{\bar{A}}, C_x)$ is observable. The approximated data driven matrix derived at the appropriate truncation order is observable, enabling individual estimation of the non linear forces.

For an overall understanding and simple implementation, the full state estimator described is suffice. However, given we measure the actual states, we do not need a 4th order system for estimation. The following equations illustrate a reduced form of the estimator or auxiliary state observer.

From the original equations defined in (8.6) we get

$$\dot{x} - A_x x - B_u u = A_\zeta \zeta \tag{8.13}$$

where, A_x and A_ζ are known. The left hand side represents the available signal; the right hand side is associated with the signal to be estimated.

The equation for the derivatives of the non linear forces is given by (8.7) which can be therefore be represented as

$$\dot{\zeta} = \bar{J}_x x + \bar{J}_\zeta \hat{\zeta} + \bar{J}_u u + \text{Error Driver} \tag{8.14}$$

i.e. a sum of the approximated derivative and the error driver.

The error driver is given as,

$$\text{Error Driver} = L_\zeta(A_\zeta\zeta - A_\zeta\hat{\zeta}) = (\dot{x} - A_x x - B_u u - A_\zeta\hat{\zeta}) \tag{8.15}$$

Here, $(\dot{x} - A_x x - B_u u)$ represents the available part and $\hat{\zeta}$ is estimated using this from the data driven model.

From (8.14) the derivative of the estimated signal can be written as

$$\dot{\hat{\zeta}} = (\bar{J}_x - L_\zeta A_\zeta)\hat{\zeta} + (\bar{J}_x - L_\zeta A_x)x + L_\zeta\dot{x} + (\bar{B}_u u - L_\zeta J_u)u \tag{8.16}$$

The error in the non linear element estimation is given by

$$e_\zeta(t) = \zeta(t) - \hat{\zeta}(t) \tag{8.17}$$

and the estimated derivative of x by

$$\dot{\hat{x}} = A_x x + A_\zeta\hat{\zeta} \tag{8.18}$$

This error is propagated through the error in the "estimated" x given by $\hat{x}$ and is solely due to the error in estimation of ζ given by $\hat{\zeta}$

$$\begin{aligned} e_x(t) &= (x(t) - \hat{x}(t)) \\ \dot{e}_x(t) &= (\dot{x}(t) - \dot{\hat{x}}(t)) \end{aligned} \tag{8.19}$$

The error derivative can be represented as:

$$\begin{aligned}\dot{e}_x(t) &= (\dot{x}(t) - \hat{\dot{x}}(t)) \\ &= (A_x x(t) + A_\zeta \zeta(t)) - (A_x x(t) + A_\zeta \hat{\zeta}(t)) \\ &= A_\zeta (\zeta(t) - \hat{\zeta}(t)) \\ &= A_\zeta e_\zeta(t)\end{aligned} \tag{8.20}$$

For each time step of Δt, the error relationship can therefore be given as

$$\begin{aligned}e_x(t) &= \int_{\Delta t} \dot{e}_x dt \\ &= A_\zeta \Delta e_\zeta\end{aligned} \tag{8.21}$$

The error dynamics is given by

$$\dot{e}_\zeta(t) = (J_\zeta - L_\zeta A_\zeta) e_\zeta(t) \tag{8.22}$$

The estimator converges if $(J_\zeta - L_\zeta A_\zeta)$ has negative eigen values (i.e. is asymptotically stable). Note, if we lack accurate *a priori* A_x or A_ζ, we would use the approximated values $\bar{A}_x$ and $\bar{A}_\zeta$ derived from the data driven method.

Now input u is introduced and the closed loop controller is defined as

$$\boxed{u = -K_x x - K_\zeta \hat{\zeta}} \tag{8.23}$$

where the gain K_x is chosen such that $\mathbb{R}\mathrm{e}(\lambda(A_x - B_x K_x)) < 0$ and K_ζ is a scaling factor, usually chosen as 1.

8.3 Estimator Design in Latent Variable Space

We now describe the estimator design in latent space which is useful for large amount of data and multiple non linearities. Assuming we now have a linear model, to estimate ζ we transform the augmented state space model to latent variable space

$$\boxed{\begin{aligned} z &= T^T \tilde{x} \\ z &= V^T x + W^T \zeta \end{aligned}} \tag{8.24}$$

where T is the orthonormal (modal) matrix which comes from the sample space X_z given by

$$X_z = \begin{bmatrix} x^1 & --- & --- & x^N \\ \zeta^1 & --- & --- & \zeta^N \end{bmatrix} \tag{8.25}$$

(superscript denotes sample number) via the covariance matrix C_z

$$C_z = X_z X_z^T = \begin{bmatrix} T \end{bmatrix} \Lambda_z \begin{bmatrix} T' \end{bmatrix} = \begin{bmatrix} V \\ W \end{bmatrix} \Lambda_z \begin{bmatrix} V^T & W^T \end{bmatrix} \tag{8.26}$$

V and W are the blocks of T associated with x and ζ, respectively; and Λ_z is a diagonal matrix of eigenvalues of the covariance matrix. We have $T^T = I = TT^T$. The reverse transformation gives

$$x = Vz \tag{8.27}$$

$$\zeta = Wz \tag{8.28}$$

Using (8.6), (8.7), (8.27) and (8.28) we obtain the state equation (of the general form $\dot{x} = Ax + Bu$) in the z-space which is derived as follows:

$$\begin{aligned}\dot{z} &= V^T\dot{x} + W^T\dot{\zeta} \\ &= V^T(A_x x + A_\zeta \zeta + B_x u) + W^T(J_x x + J_\zeta \zeta + B_\zeta u) \\ &= (V^T A_x + W^T J_x)Vz + (V^T A_\zeta + W^T J_\zeta)Wz + (V^T B_x + W^T B_\zeta)u\end{aligned} \tag{8.29}$$

- where the sub-blocks $(A_x, A_\zeta, B_u, J_x, J_\zeta, B_\zeta)$ may be derived from data driven method, or could be state dependent matrices. In our problem, assume we are using the blocks from the approximated data driven linear model.

Equation (8.29) can be written in compact form as

$$\boxed{\begin{aligned}\dot{z} &= A_z z + B_z u \\ y_z &= C_z z\end{aligned}} \tag{8.30}$$

where y_z is the output vector corresponding to the latent space state transition model, C_z is the output matrix, and

$$\begin{aligned}A_z &= (V^T A_x + W^T J_x)V + (V^T A_\zeta + J_\zeta \zeta)W \\ B_z &= V^T B_x + W^T B_\zeta\end{aligned} \tag{8.31}$$

We form an observer from (8.30) using an estimator gain given by L_z and with $e = (y_z - \hat{y}_z)$ as the estimation error in z space

$$\boxed{\dot{\hat{z}} = A_z\hat{z} + Bu + L_z e = A_z\hat{z} + Bu + L_z(y_z - \hat{y}_z)} \tag{8.32}$$

This can be further written as -

$$\dot{\hat{z}} = A_z\hat{z} + B_z u + L_z e_z = A_z\hat{z} + B_z u + L_z C_z(z - \hat{z}) \tag{8.33}$$

But we do not have a direct measure of error in the z space. The available error measurement is $e_x = x - \hat{x}$ which must then be made equal to $C_z(z - \hat{z}) = C_z e_z$. Therefore, from (8.27), we can write $C_z = V$. Representing the estimator in (8.32) in a mixed space of x and z we have

$$\begin{aligned}
\hat{x} &= V\hat{z} \\
\dot{\hat{z}} &= A_z\hat{z} + B_z u + L_z(x - \hat{x}) \\
&= A_z\hat{z} + B_z u + L_z V(z - \hat{z}) \\
&= (A_z - L_z V)\hat{z} + B_z u + L_z x
\end{aligned} \tag{8.34}$$

From this, the non linear elements can be predicted individually as follows:

$$\boxed{\hat{\zeta} = \begin{bmatrix} \hat{F}_g \\ \hat{F}_d \end{bmatrix} = W\hat{z}} \tag{8.35}$$

Note the x that multiplies the observer gain L in equation (8.37) is the true measurement from the non linear model. For convergence of the observer estimates we need to find a gain L such that $\mathbb{R}\mathrm{e}(\lambda(A_z - L_z V)) < 0$ – i.e., eigenvalues of $(A_z - L_z C_z)$ must be negative – and $B_z u + Lx$ is bounded, i.e. $||(B_z u + L_z x)|| \leq \alpha$ for $\forall\ \alpha$ and $||.||$ is a Euclidean norm. This is done by ensuring (A_z, V) is observable and (A_x, B_x) is controllable.

Starting with equation for the estimated latent variable given by,

$$\hat{z} = V^T x + W^T \hat{\zeta} \tag{8.36}$$

- and the estimated auxiliary variables as

$$\begin{aligned} \hat{\zeta} &= \zeta + e_\zeta \\ &= Wz + We_\zeta \end{aligned} \tag{8.37}$$

where e_ζ is the estimation error in ζ, we can rewrite (8.36) as

$$\begin{aligned} \hat{z} &= V^T x + W^T \hat{\zeta} \\ \hat{z} &= V^T x + W^T \zeta + W^T e_\zeta \end{aligned} \tag{8.38}$$

We can write $\hat{z}$ as solely dependent on z and error in ζ

$$\boxed{\hat{z} = z + W^T e_\zeta} \tag{8.39}$$

and the derivative -

$$\boxed{\dot{\hat{z}} = \dot{z} + W^T \dot{e}_\zeta} \tag{8.40}$$

Multiplying by V from the left on both sides of (8.39) and using (8.27) and (8.28)

$$\begin{aligned} V\hat{z} &= VV^T z + VW^T e_\zeta \\ \hat{x} &= x + VW^T e_\zeta \\ x - \hat{x} &= -VW^T e_\zeta \\ e_x &= -VW^T e_\zeta \\ e_z &= -W^T e_\zeta \end{aligned} \tag{8.41}$$

The equation (8.41) shows the error relationships in latent space. Error in estimation of original states comes entirely from the error in the the auxiliary variable estimates. Therefore we need to form the error dynamics equation in the auxiliary variable space which in turn will be derived from the latent variables. Assuming input is unaffected or zero, we have $\dot{z} = A_z z$ and using (8.40) and (8.41), we have

$$\begin{aligned} \dot{\hat{z}} &= A_z\hat{z} + L_z(x - \hat{x}) \\ \dot{\hat{z}} &= A_z\hat{z} - L_z VW^T e_\zeta \\ \dot{z} + W^T\dot{e}_\zeta &= A_z z + A_z W^T e_\zeta - L_z VW^T e_\zeta \\ W^T\dot{e}_\zeta &= (A_z - L_z V)W^T e_\zeta \\ WW^T\dot{e}_\zeta &= W(A_z - L_z V)W^T e_\zeta \\ \dot{e}_\zeta &= W(A_z - L_z V)W^T e_\zeta \end{aligned} \tag{8.42}$$

The equation for error dynamics of ζ in the mixed space is given by

$$\boxed{\dot{e}_\zeta = W(A_z - L_z V)W^T e_\zeta} \tag{8.43}$$

For asymptotic stability, we solve for $\dot{e}_\zeta = 0$ i.e.

$$e_\zeta \xrightarrow[t\to\infty]{} 0$$

Using (8.34) and (8.43), the observer dynamics purely in latent space can be given as follows:

$$\begin{bmatrix} \dot{e}_z \\ \dot{\hat{z}} \end{bmatrix} = \begin{bmatrix} (A_z - LV)W^T & 0 \\ LV & A_z \end{bmatrix} \begin{bmatrix} e_z \\ \hat{z} \end{bmatrix} \tag{8.44}$$

where $e_z = z - \hat{z}$ is the estimation error in the latent space.The estimated auxiliary variables are now given by $\hat{\zeta} = \mathbf{W}\hat{\mathbf{z}}$ as in (8.28).

Though our goal is to apply the control input in the original second order non linear system, for complete understanding of the closed loop output feedback compensation in the latent space, we have the controller in z space derived as

$$\begin{aligned} u &= -K_x x - K_\zeta \hat{\zeta} \\ u &= -K_x(Vz) - K_\zeta(W\hat{z}) \\ u &= -K_x V(\hat{z} + e_z) - K_\zeta(W\hat{z}) \\ u &= -(K_x V + K_\zeta W)\hat{z} - K_x V e_z \end{aligned} \tag{8.45}$$

The control gain in z space can be given as $u = -K_z z = -K_z(\hat{z} + e_z)$. If the controller gains K_z are chosen such that the matrix $(A_z - B_z K_z)$ is Hurwitz, then $\hat{z}$ will also be bounded in the region of operation. Since both $(A_z - B_z K_z)$ and $(A_z - L_z C_z)$ are designed to have eigenvalues with negative real parts the closed loop system is both asymptotically and BIBO stable.

8.4 Error Analysis

There are broadly two error sources: one due to modeling, the other due to prediction or estimation. The error associated with the linearized data driven model alone and not contributed due to prediction method, are called modeling error. In other words it is the error in linearization of the original non linear equations and approximation of the state matrices $\tilde{A}$ and $\tilde{B}$ from the system's data. Modeling error therefore can be contributed by:

1. Truncation order and neglected non linearities
2. Sampling method using the grid type platform versus time evolving simulation
3. Region $\phi(h,w)$ used for modeling
4. Density of the data
5. Numerical computation errors
6. Unmodeled dynamics

To illustrate the error and how model improvement reduces such error, for simplicity, let us use an undriven system. That is, u=0. If the analytical augmented state transition matrix is $\tilde{A}(h,w)$ and the approximated data driven constant linear model is given by $\bar{\tilde{A}}$, then the modeling error (as expressed through state derivatives) at any time t can be expressed as follows:

$$\Delta\dot{\tilde{x}}(t) = \tilde{A}\tilde{x}(t) - \bar{\tilde{A}}\tilde{x}(t) = \Delta\tilde{A}\tilde{x}(t) \tag{8.46}$$

Since the actual $\tilde{A}(h,w)$ is state dependent and therefore varies with h and w, the error is also state dependent and varies in $\phi(h,w)$. It is not entirely clear how to compare the

analytic non linear model with the approximated data driven model. Elemental comparison may not make sense here since the J_x and J_ζ are trying to approximate the non linear state dependent variables like $\frac{dF_g}{dh}$ and $\frac{dF_d}{dw}$ and that is hard using a single number. So, the occurrence of non zero elements in the matrix elements which are zero in the analytic non linear matrix model to somehow bring in the effects of non linearities might not be surprising. It is therefore not trivial to infer that the non zero elements in the data driven model are errors because of the corresponding zero elements in the analytic model. The matrices obtained from grid based method gives a form which is however easier to compare with the analytic version where as time based simulation looks more like a blackbox model. We will demonstrate this with our examples application in the next section.

8.5 Results: Micro UUV application

Let us apply the estimator on our model of the micro UUV derived in Chapter 6 in (7.5). Assume only the original state variables – h, w – are being measured. We use the linear model obtained from the grid method. Data driven models obtained from a grid often underperform in long term derivative prediction, as shown in Chapter 6. However, as far as the constant part of the model goes, it bears closer resemblance to the analytic model. We will show that even with a relatively inaccurate or sub optimal model, estimations of non linear forces can be done using the state observer. We choose therefore to emphasize ease of interpretation.

In Figure (8-2), we start with an initial condition of $h = 0, w = 0$ and the matrix is given by 7.5, and no external force is applied, i.e. $u = 0$. The body is in the positive F_g region, therefore experiences a positive force. The estimator tracks the position as shown and the estimation converges in the original state variables as well as the non linear forces, and the the latent variable space.

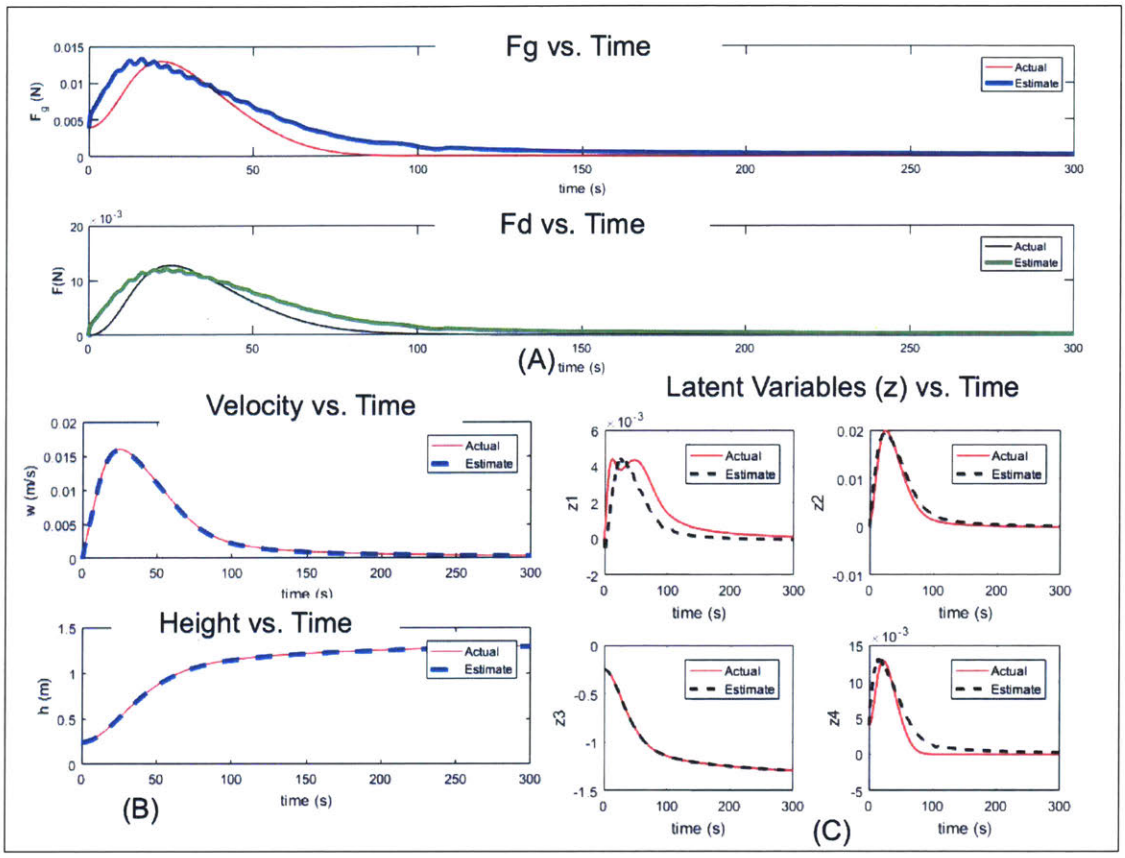

Figure 8-2: Results shows convergence in estimation of (A) non linear forces F_g and F_d (B) state variables h and w (C) in the latent variables space, that is convergence of z_1, z_2, z_3 and z_4. Note the latent variables are linear combinations of the auxiliary and state variables since $z = T'\tilde{x}$

In Figure (8-3), we show the error convergence in the original state variables, the non linear forces F_g and F_d, and the long term error convergence in latent variable space. Note in the equation the total force is $F_g - F_d$; as a result, the error being equal, they cancel perfectly ensuring faster convergence in the total force than that of the individual forces.

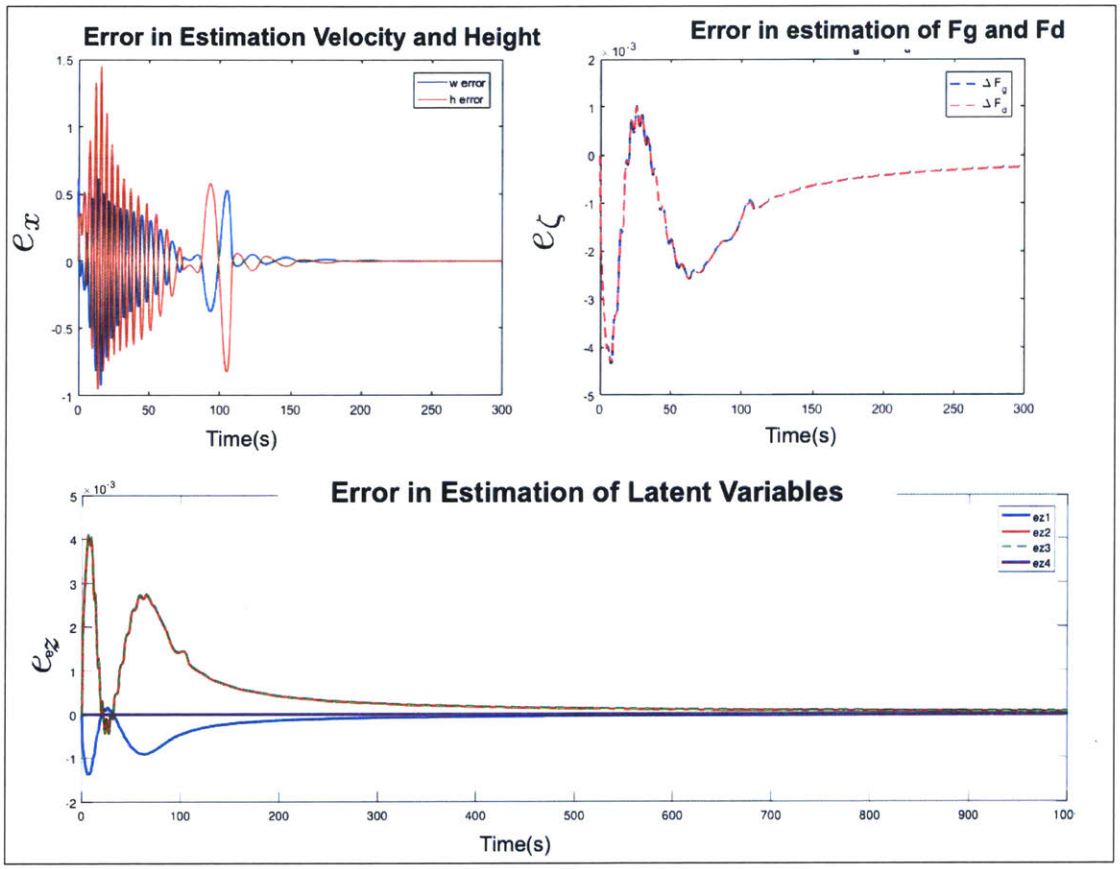

Figure 8-3: Results showing error convergence in (A) estimation of non linear forces F_g and F_d. Note, $F_T = F_g - F_d$ (B) the estimated state variables estimation h and w (C) the latent variables z_1, z_2, z_3 and z_4.

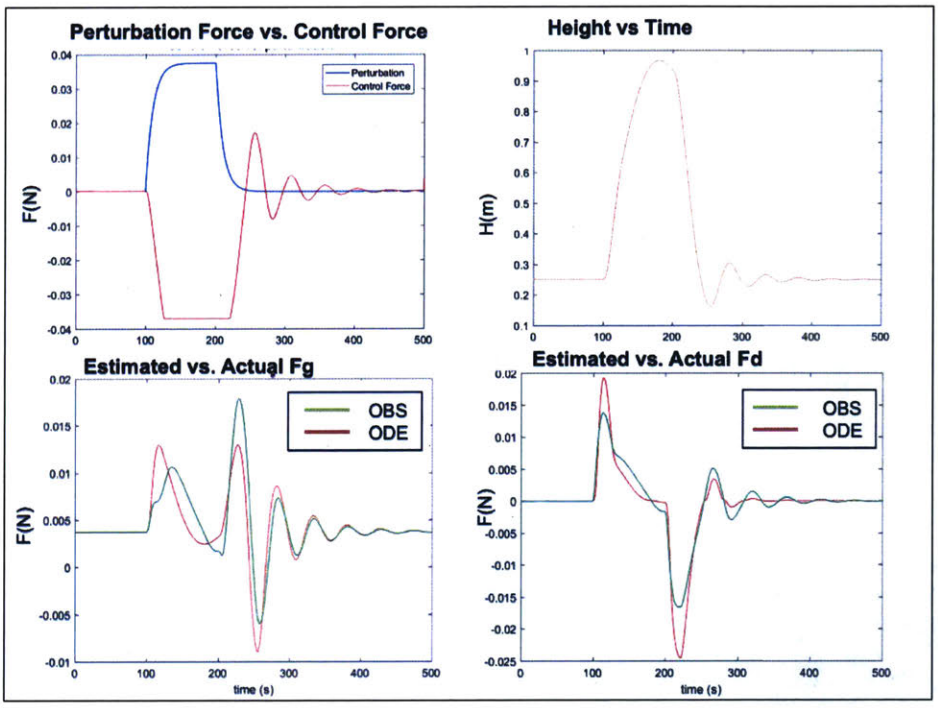

Figure 8-4: Feedback Compensation using both estimator and closed loop control, with $u(t) = -Kx(t) - \hat{F}_d - \hat{F}_g$

8.5.1 Error Analysis

Let us now discuss the various kinds of modeling and prediction error as applies to our problem. We saw in Chapter 6, based on the net RMS error of the state derivatives one could choose the truncation order. Here we revisit the concept, and see how truncation order affects the prediction and estimation of the auxiliary state variables. We next compare the data driven model against the analytical model and apply various numerical corrections to the elements. We also explore how sampling region affects the modeling of the state transition matrix, and thereby the estimation of the non linear elements. Finally, we also show that convergence in the estimation of non linear elements is faster if true value of the original states are used, instead of estimated values.

8.5.2 Truncation Error

As shown in Chapter 6, the ideal order of truncation for two non linear elements was found to be 7, though 6 seemed to work fine as well. We find in Figure (8-5), that estimation error is slightly higher at 7 than in 6. At order 4, and 5 as we already have seen, the model faces problem due to pseudo-inversion. In Figure (8-6),we use linear drag, and therefore there is only one non linear element and as discussed in Chapter 6, it has least modeling error for 5th order truncation. The prediction error is also found to be the least for this order.

The matrix model at with two non linear elements at 6th order (optimizing between modeling and truncation error) is given as:

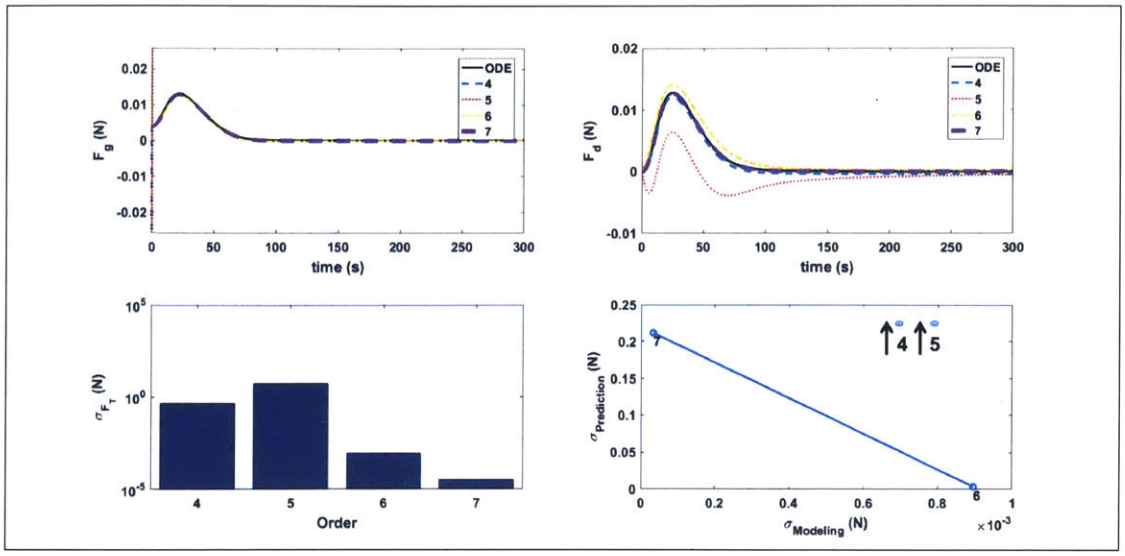

Figure 8-5: Error due to Truncation Order with non linear drag and non linear ground force

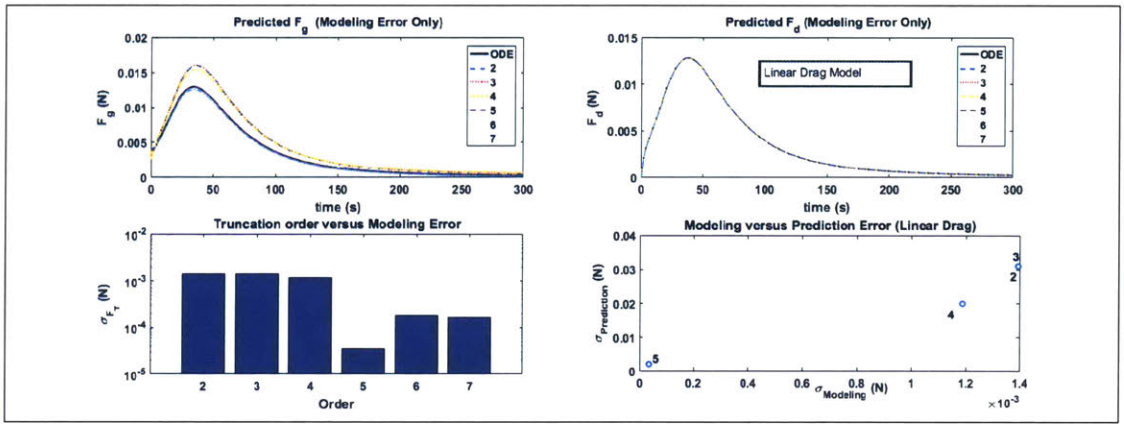

Figure 8-6: Error due to Truncation Order with linear drag and non linear ground force. Bottom Right: Modeling Versus Prediction Error shows very high error for 4th and 5th order.

$$\begin{bmatrix} \dot{w} \\ \dot{h} \\ \dot{F}_g \\ \dot{F}_d \end{bmatrix} = \begin{bmatrix} -0.004919 & -0.007430 & 0.252801 & -0.252492 \\ 0.999996 & -0.002997 & 0.000005 & -0.000302 \\ -0.000086 & -0.00002 & 0.000050 & -0.001507 \\ 0.833822 & 0.000023 & 0.3769891 & -1.340565 \end{bmatrix} \begin{bmatrix} w \\ h \\ F_g \\ F_d \end{bmatrix} + \begin{bmatrix} 0.252803 \\ 0.000031 \\ -0.000050 \\ 0.378132 \end{bmatrix} u$$

$$y = \begin{bmatrix} 1 & 0 & 0 & 0 \\ 0 & 1 & 0 & 0 \end{bmatrix} \begin{bmatrix} w \\ h \\ F_g \\ F_d \end{bmatrix} \tag{8.47}$$

The subparts are

$$\bar{A}_x = \begin{bmatrix} -0.00491 & -0.007430 \\ 0.9996 & -0.002997 \end{bmatrix} \quad \bar{A}_\zeta = \begin{bmatrix} 0.252801 & -0.252492 \\ 0.000005 & -0.000302 \end{bmatrix} \quad \bar{B}_u = \begin{bmatrix} 0.252803 \\ 0.000031 \end{bmatrix} \tag{8.48}$$

$$\bar{J}_x = \begin{bmatrix} -0.000086 & -0.00002 \\ 0.833822 & 0.000023 \end{bmatrix} \quad \bar{J}_\zeta = \begin{bmatrix} 0.000050 & -0.001507 \\ 0.3769891 & -1.340565 \end{bmatrix} \quad J_u = \begin{bmatrix} -0.000050 \\ 0.378132 \end{bmatrix} \tag{8.49}$$

Corresponding blocks from the analytical model ($\tilde{A}$) would be

$$A_x = \begin{bmatrix} 0 & 0 \\ 1 & 0 \end{bmatrix} \quad A_\zeta = \begin{bmatrix} 1/S_z & -1/Sz \\ 0 & 0 \end{bmatrix} \quad B_u = \begin{bmatrix} 1/Sz \\ 0 \end{bmatrix} \tag{8.50}$$

$$J_x = \begin{bmatrix} \frac{dF_g}{dh} & 0 \\ 0 & 0 \end{bmatrix} \quad J_\zeta = \begin{bmatrix} 0 & 0 \\ \frac{1}{S_z}\frac{dF_d}{dw} & -\frac{1}{S_z}\frac{dF_d}{dw} \end{bmatrix} \zeta \quad J_u = \begin{bmatrix} 0 \\ \frac{1}{S_z}\frac{dF_d}{dw} \end{bmatrix} \tag{8.51}$$

8.5.3 Linearization Error

Having chosen the model, let us now compare the data driven one with the actual one in Figure (8-7). The bold number in the approximated matrix indicate the positions where the corresponding elements are zero in analytic version. We already corrected for the first two rows i.e. A_x and A_ζ in the previous results in matrix (2) . But the elements in J_x that has coefficients for h would give rise to fictitious forces as shown in Figure (**??**). Cause, here the h is going to a steady state of 1.5m instead of 0. So a coefficient corresponding to this would yield a non zero value in force derivatives- therefore giving a contribution to the net force. The correction (P3), i.e. zeroing out all the elements corresponding to h helped to remove the fictitious force due to it's contribution and ensure convergence.

In the picture below we show the various steps of corrections.

Note the correct way of correction -if we already know that the state variables are measured- is to take that in account during the formation of the linear model either by placing constraints or only by fitting J_x and J_ζ using the common regressor method.

As we corrected all the h coefficients, the bias got removed and convergence in total force is seen pretty fast since the errors of the two non linear forces cancel out each other quite early. There is an overshoot in estimation of individual non linear forces which can be corrected by tuning the gain L. When all the positions that have zero in the nominal were corrected to match the nominal (theoretical) as in matrix (4)- while a faster dead on convergence was observed, the non linear forces underperformed. Trying to increase the L leads to some improvement - but high gain leads to lot of ringing. Complex conjugates poles can be used to smoothen that. One cannot indefinitely increase the gain,

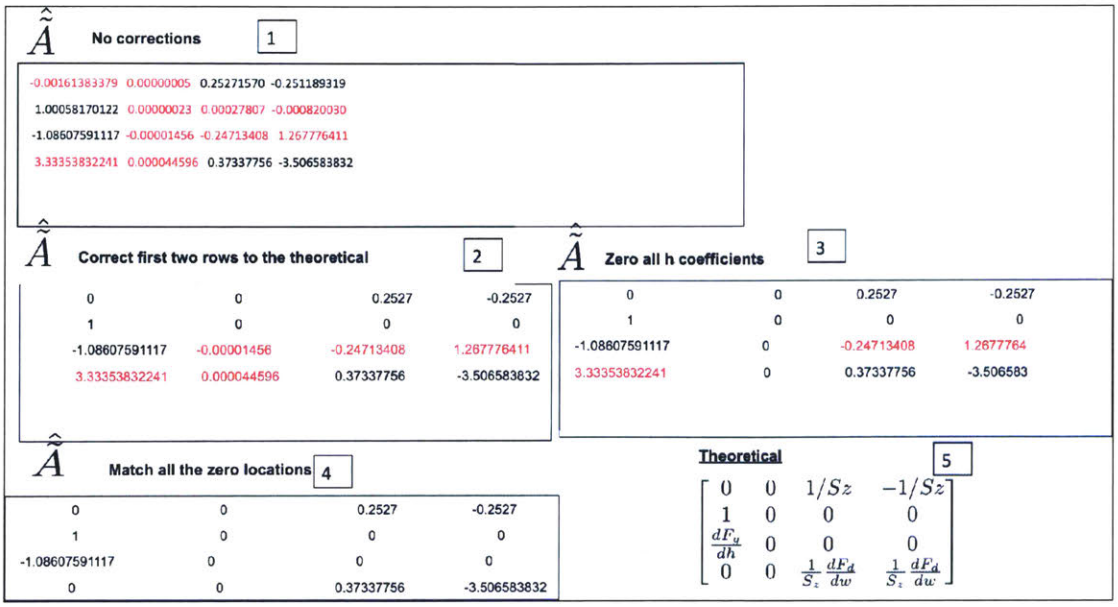

Figure 8-7: Comparison with theoretical matrix structure (1) is the original data driven matrix, as is (2) is the matrix with first and second row - A_x and A_ζ corrected. (3) is the matrix with all the coefficients of h replaced by 0. (4) Zeroes are placed in location following the theoretical model

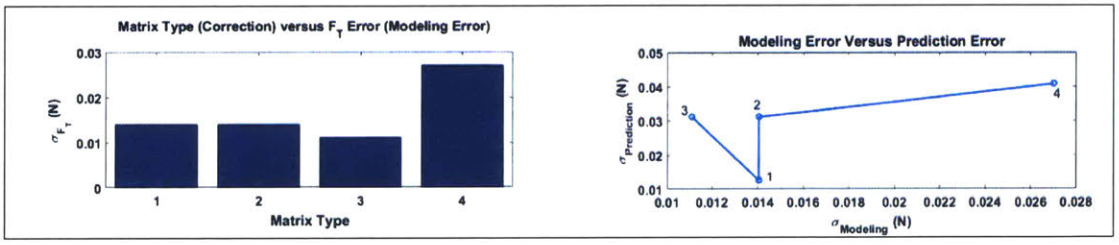

Figure 8-8: Left: RMS error in net F_T prediction due to modeling. X axis denotes the matrix index. Right: Modeling versus Prediction error

the bounds of L_x are availed SVD analysis. This is shown in the figure below- (a) showing h coefficients corrected, (b) Substitute all locations that are zero in the theoretical matrix as zero (c) With maximum gain L before system becomes unstable.

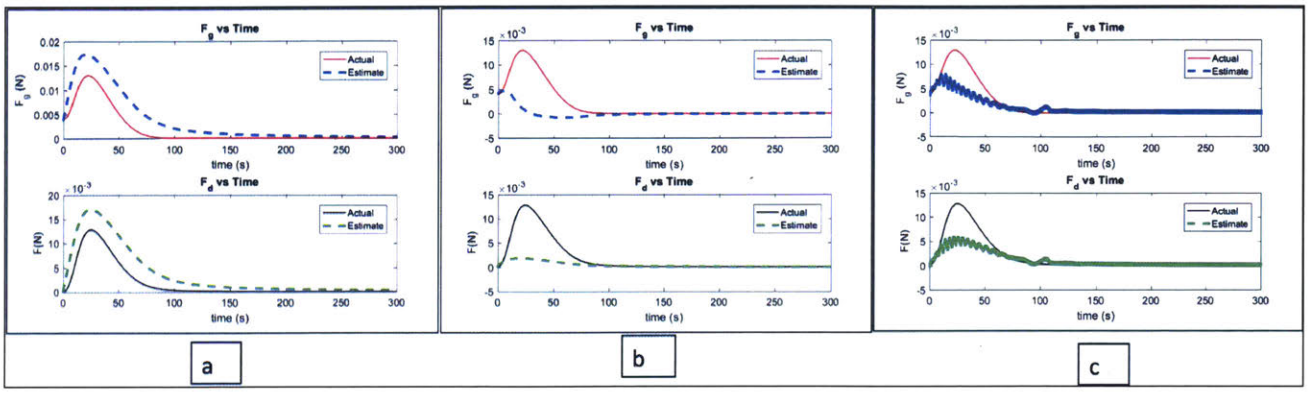

Figure 8-9: Implementations of corrections and system response (a) h values set to zero (b) All positions zero in nominal are made zero in the data model as in (4) (c)High estimator gain using matrix (4). Contour tracking is poor even at high complex gains

8.5.4 Error based on Sampling Region

Next we show how the error varies with sampling region chosen.

This is shown in the Figure (8-10) and Figure(**??**). It is seen that grid method generates models which are very robust across most of the operational region $\phi(h,w)$. This is also because the corrections are applied easily to the grid method. The error increases for including the negative values of h. We see that $h = 0$ to $h = 1.2$ is an appropriate choice for sampling region and enables a large area for operation of the linear model.

In contrast however, time evolving simulation method is very sensitive to regional changes as we can see in the Figure (**??**) if no correction is applied. As we mentioned before, the matrix obtained from this method can often be a blackbox and therefore comparison

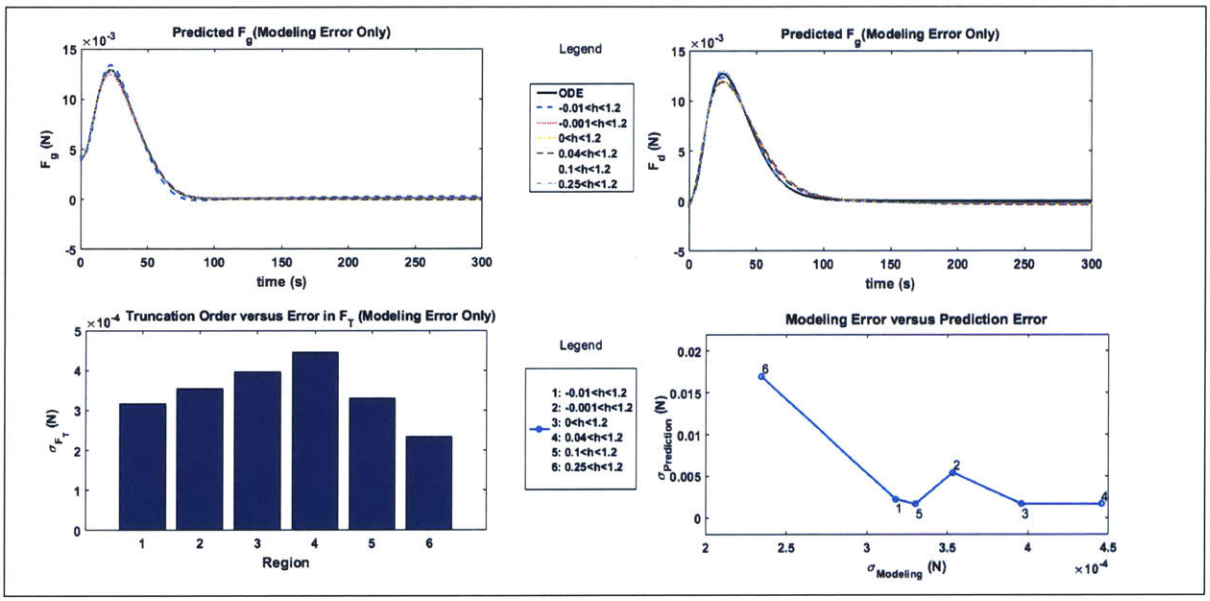

Figure 8-10: Error analysis based on sampling region for the (P3) matrix, i.e. with applied corrections

may not be easy.

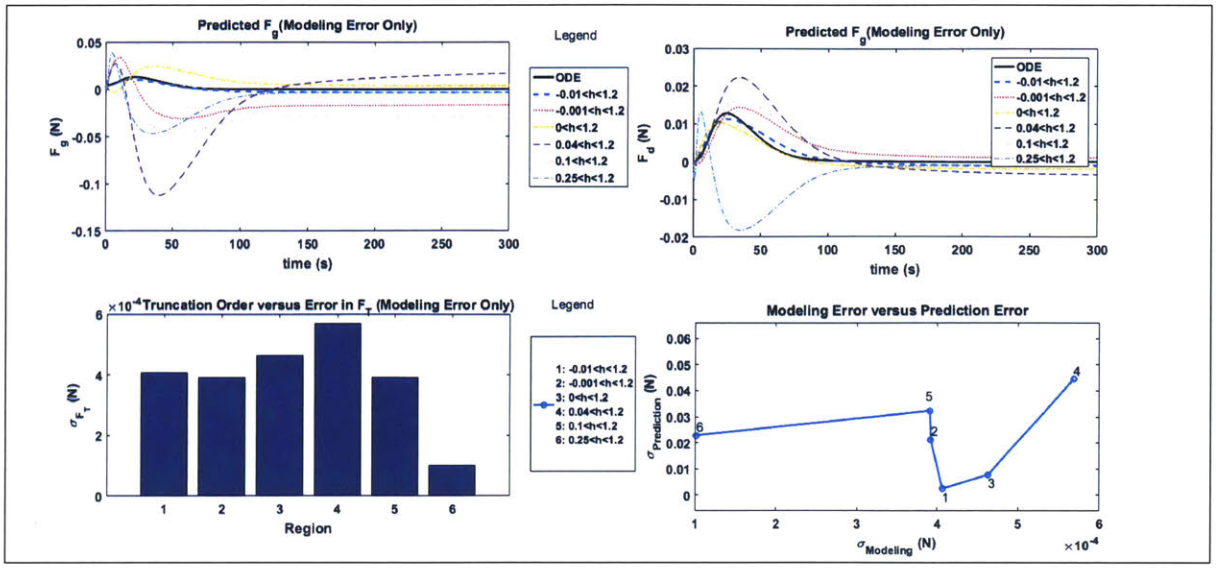

Figure 8-11: Error analysis based on sampling region using time evolved simulation method when no correction to the data driven matrix is applied

8.5.5 Prediction Model Error

In Figure (8-12) we show the difference of results when using the estimated states (if A_x and A_ζ were not known and were estimated) for both state update and error propagation, versus using true state for state updates and estimated states for error propagation. Note the Method (2) has a faster convergence since it is not propagating errors in estimated states, whose values are measured in any case.

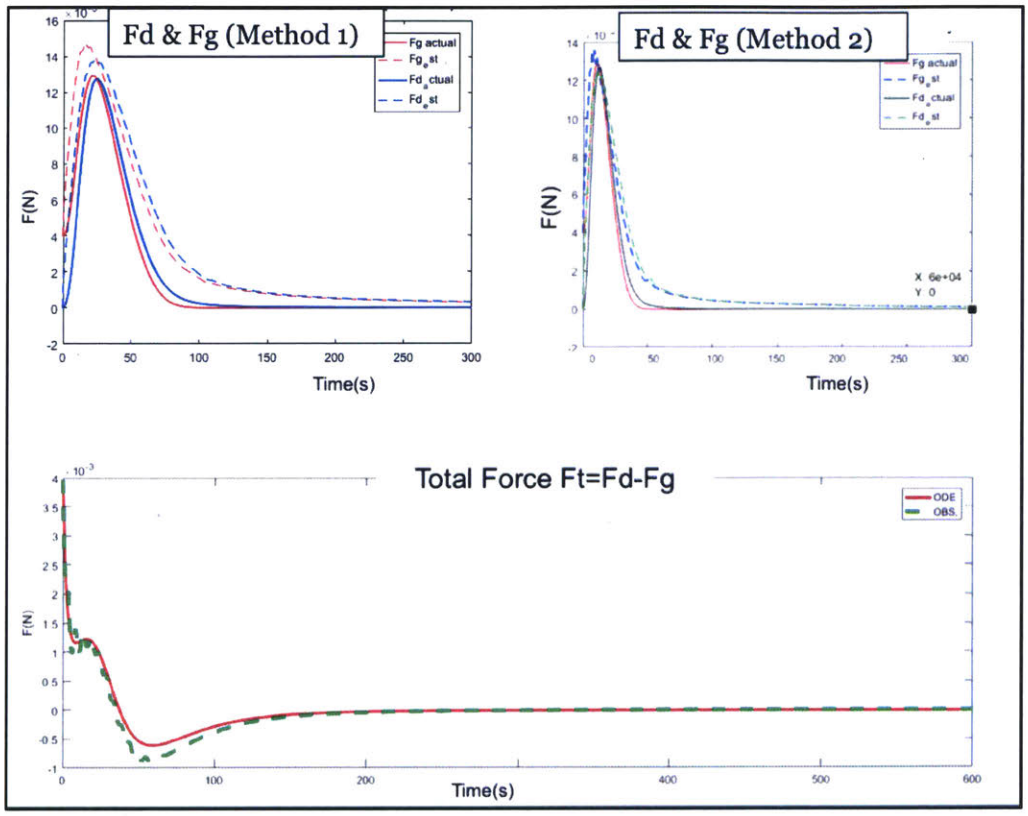

Figure 8-12: Results from method 1 where estimated states are used as next state, and from 2 where true values of the states are used for state update, and estimated values for error propagation

8.6 Robustness, Performance and Convergence Analysis

Given any nominal stable (in terms of estimator dynamics) state transition matrix, we can define a numerical perturbation bound. Let $\tilde{A}_0$ denote the data driven nominal matrix in the augmented space- i.e. that is, $A_0 = (\tilde{A} - L_x C_x)$ has negative eigen values (or estimator dynamics is closed loop stable). The most basic approach of robustness is asking: How much perturbation $f(\tilde{x},t)$ can this nominal matrix withstand and still be stable? That is, for an observer equation - we ask if-

$$\dot{\hat{\tilde{x}}} = \tilde{A}_0 \hat{\tilde{x}}(t) + f(\tilde{x},t) \tag{8.52}$$

-what are the bounds on the uncertainty $||f(\tilde{x},t)||$ such that the system $(A_0 + f)\hat{\tilde{x}}$ still converges asymptotically? Here $\hat{\tilde{x}}$ is the estimated value of $\tilde{x}$ and L is the observer gain. The above equation comes represents a general nominal matrix with uncertainty. We can approach this in two ways. We can use the parametrically varying matrix $\tilde{A}$ as nominal or we can use the stable form of a certain matrix obtained from data driven method $A_0 = (\bar{\tilde{A}} - L_x C_x)$ to be the nominal. In the second case, this matrix is the one derived in previous section based on error analysis. We then show much uncertainty can be associated with this particular $\bar{\tilde{A}}$ matrix and the designed estimator dynamics still converges. One way to look at it, if the elements could change based on modeling errors, how much variation could the closed loop model take and still be stable?

The simplest bound μ we can define using a Lyapunov function is given by:

$$\frac{||f||}{||x||} < \frac{\sigma_{min}(Q)}{\sigma_{max}(P)} = \mu \tag{8.53}$$

where P is the solution of the Lyapunov equation $P\bar{\tilde{A}}_0 + \bar{\tilde{A}}_0^T P + 2Q = 0$. For a norm

bounded unstructured perturbation, where the element distribution are not known, the norm is given by the spectral norm of the perturbation matrix and the bound is called the Patel-Toda bound. In this case, the maximum value of the bound is for $Q = I$

$$\frac{||f||}{||x||} < \frac{1}{\sigma_{max}(P)} = \mu_p \tag{8.54}$$

For the matrix we obtained using grid type simulation method, (7.5), we have $\mu_p = 0.005$ Note, $\sigma_{max(P)}$ is the maximum singular value of P. We see that our bound also satisfies Patel Toda requirement that μ_p is in turn bounded by the stability degree, α_s of the stable system A_0. That is,

$$\mu_p = \frac{1}{\sigma_{max}P} < -Max\ \Re[\lambda_i(A_{x0})] = -\alpha_s = -(-1) = 1 \tag{8.55}$$

-where $-\alpha_s$ is a positive scalar and $Max\ \Re[\lambda_i(A_{x0})] = -1$

Now, let us utilize more information about the matrix we have. One could assume uncertainty is restricted only to rows for estimating the non linear elements since the true state variables are measured. Then, using concepts from structured perturbation, one could define elemental bounds. This is formulated as following:

Let U_n be the matrix to denote the perturbation or uncertainty structure. That is, the elements with $u_{ij} = 1$ denote the elements of $\bar{\bar{A}}$ with perturbation.

$$U_n = \begin{pmatrix} 0 & 0 & 0 & 0 \\ 0 & 0 & 0 & 0 \\ 1 & 1 & 1 & 1 \\ 1 & 1 & 1 & 1 \end{pmatrix} \tag{8.56}$$

The Patel Toda elemental bound is given by $\mu_{\varepsilon p} = \frac{\mu_p}{n} = 0.0008$. Using the structural

information, we can define the Yedavalli bound $\mu_{\varepsilon Y} = \frac{1}{\sigma_{max}[[P][U_n]_s}$ which has a higher value and is given by $\mu_{\varepsilon Y} = .0013$.

Concept of what robustness bounds for a data driven linearized matrix stands for is still fairlyunexplored, but one can say that given the data driven matrix $\bar{\bar{A}}$ we can establish bounds to get an estimate of numerical variations in the elements that our close loop estimator dynamics will be able to tolerate and ensure convergence.

8.7 Convergence at Steady State

We already showed the criterion for convergence based on the estimator dynamics. However, since even the concept of observability matrix for a data driven system model is yet to get a more meaningful perspective, it is worthwhile to explore other convergence criterions. Comparing non linear observability metrics with a linear model is not beneficial. However, if one must follow the numeric bounds to guarantee asymptotic convergence as described in previous section, it may rule out a large number of our results where we observe convergence. The bounds are highly conservative for our purpose.

The idea of reference nominal is somewhat ambiguous when the nominal matrix is derived from a different training regions and has little resemblance with the theoretical matrix. Secondly, though fast convergence was noticed, the undershoot was severe in using matrix (P4) in Figure (8-7). Here, we define a simple but sufficient steady state convergence criterion using a bit more of system information, i.e. a situation where state variables are measured and known and the convergence is only needed for the non linear forces.

$$\dot{\tilde{x}}_{ss} = 0 \tag{8.57}$$

$$\tilde{x}_{ss} = \begin{bmatrix} w_{ss} \\ h_{ss} \\ F_{g_{ss}} \\ F_{g_{ss}} \end{bmatrix} = \begin{bmatrix} 0 \\ h_{ss} \\ 0 \\ 0 \end{bmatrix} \tag{8.58}$$

The reason of showing steady state convergence is simple. We know the variable values at these points. In Figure (8-13) if the system is perturbed and results at (1), (2), (3) or (4), without feedback control, it will either go to a steady state at $h = 1.2m$ or at $h = 0$ and at either of these two heights, w, F_g, F_d goes to zero.

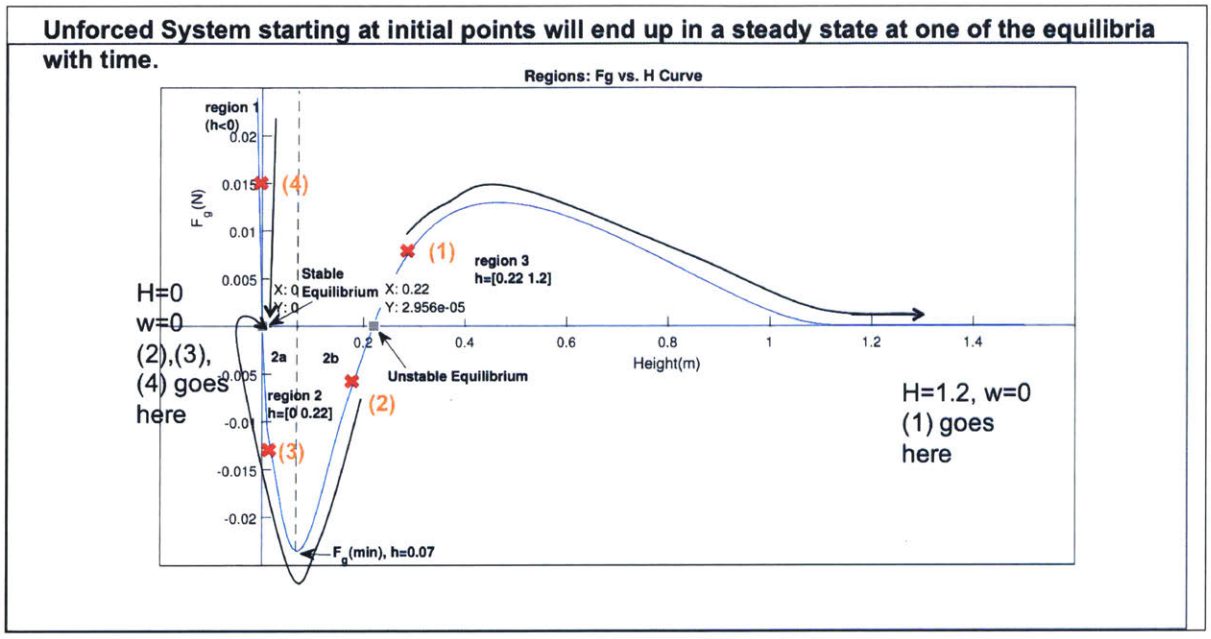

Figure 8-13: EE

Let us again start with the matrix model as in (P3).

$$\begin{pmatrix} \dot{\hat{x}} \\ \dot{\hat{\zeta}} \end{pmatrix} = \begin{pmatrix} A_x & A_\zeta \\ \bar{J}_x & \bar{J}_\zeta \end{pmatrix} \begin{pmatrix} x \\ \hat{\zeta} \end{pmatrix} + \begin{pmatrix} B_u \\ \bar{J}_u \end{pmatrix} u \tag{8.59}$$

Since x is measured, convergence of x is not an issue. We therefore focus on the behavior of ζ. Based on our estimator formula, for state update we use the true value of x.

$$\dot{\hat{\zeta}} = \bar{J}_x x + \bar{J}_\zeta \hat{\zeta} \tag{8.60}$$

Since x in (8.60) is measured, we can take it to be correct. Therefore, at steady state $\dot{h} = w = 0$; and in an unforced system $u = 0$. We assume one correction explicit correction to account for physical knowledge of the system: all elements multiplying h are zero, i.e.

$$\bar{\bar{A}}_{ih} = 0 \qquad \forall i \tag{8.61}$$

Therefore,

$$\bar{J}_x = \begin{pmatrix} \bar{J}_{x_{11}} & 0 \\ \bar{J}_{x_{21}} & 0 \end{pmatrix} \tag{8.62}$$

That is, we use the matrix (P3) in Figure (8-7): the reasons being already explained in previous section (remove fictitious forces). At steady state of the true system, we can then simplify (8.59)

$$\begin{aligned} \dot{\hat{\zeta}} &= \bar{J}_x x_{ss} + \bar{J}_\zeta \hat{\zeta} \\ &= \begin{pmatrix} \bar{J}_{x_{11}} & 0 \\ \bar{J}_{x_{21}} & 0 \end{pmatrix} \begin{pmatrix} w = 0 \\ h_{ss} \end{pmatrix} + \bar{J}_\zeta \hat{\zeta} \\ \dot{\hat{\zeta}} &= \bar{J}_\zeta \hat{\zeta} \end{aligned} \tag{8.63}$$

This is in the general form of the equation $\dot{X} = MX$.Therefore a sufficient condition for (8.59) to converge is that $\bar{J}_\zeta$ has negative eigenvalues *and* the h terms in $\bar{J}_x$ are zero. Let us look again at equation (8.60) without any corrections to $\bar{J}_x$ i.e. now we go back to matrix (P2). We still assume unforced system ($u = 0$) and steady state, i.e. $x = \text{constant} \equiv x_\infty$. At

this point of operation, we want:

$$\begin{aligned} \hat{\dot{\zeta}} &= 0 \\ \bar{J}_x x_{ss} + \bar{J}_\zeta \hat{\zeta} &= 0 \end{aligned} \tag{8.64}$$

If there exists a ζ_∞ such that

$$\bar{J}_\zeta \zeta_\infty = -\bar{J}_x x_{ss} \tag{8.65}$$

then (8.60) can be rewritten as

$$\hat{\dot{\zeta}} = \bar{J}_\zeta (\zeta - \zeta_\infty) \tag{8.66}$$

which will converge if $\bar{J}_\zeta$ has negative eigenvalues – but to ζ_∞ rather than to zero.

Given a data driven matrix asymptotic convergence is guaranteed if $\bar{J}_\zeta$ is asymptotically stable, and elements of h is 0. If elements of h are not zero, model may converge to some fictitious force contributed by h which is not otherwise being compensated. In either case, convergence of total force is guaranteed.

8.7.1 Closed Loop Convergence

Closed Loop Estimator Convergence follows directly from the reduced order observer rule for asymptotic stability. However, for the steady state criterion discussed, which is another way of looking for a goodness factor, there is no change when using with closed loop. The system is easier to represent with a full state feedback but with error propagation and state update procedure as described before. This is because, the error is passed only to correct

Jx, and therefore has no effect on J_ζ directly. However, the column of h is no longer zero in the closed loop system. So, convergence occur according to (8.65)

8.7.2 Bounds

Given J_ζ has negative eigenvalues, then how much uncertainty can J_ζ have and still be stable? The robustness measure is therefore directly on the J_ζ. For a stable open or a stable closed loop system, we can now use the different bounds and use the one with the best upper bound.

For open loop or full state observer, the Patel Toda bound, we have in this case, $\mu_p = \frac{1}{\sigma_max(P_\zeta)} = 0.1$ as the elemental bound on J_ζ. Note this is a much higher bound than obtained previously for the entire matrix.

For Yedavalli bound, uncertainty is considered in each element of J_ζ. The bound is given by $\mu_{\varepsilon Y} = \frac{1}{\sigma_{max}[|P|U_n]_s} = 0.13$ which is somewhat higher that Patel Toda bound.

8.8 Other Observervations

1)Improved Robustness— It was observed that J_ζ being uniformly negative definite (UND) makes the system more robust in terms of uncertainty bounds. For UND, the following holds true.

$$\frac{J_\zeta + J_\zeta}{2} \leq -\beta_1 I < 0 \tag{8.67}$$

2)Performance ratio ψ: We found the ratio of J_ζ and J_x gave an insight to the system performance. Increasing cause damping or undershoot with faster convergence and decreasing it cause overshoot. J_x showed opposite behaviors.

$$\psi = \frac{||J_\zeta||}{||J_x||} \tag{8.68}$$

We vary ψ by varying J_ζ and results are shown in Figure (??), Figure (??), Figure(??).

3) Bounds for Control: For closed loop control, let us assume the total uncertainty associated with non linear forces is bounded by $||\Delta||$. For perfect cancellation of the non linear forces ζ in the dynamical equations, we must have therefore

$$\zeta - K_\zeta(\zeta + ||\Delta||) = 0 \tag{8.69}$$

$$\boxed{||\Delta|| = 1/K_\zeta(K_\zeta - 1)||\zeta||} \tag{8.70}$$

8.9 Control

8.10 Conclusion

In this chapter we concluded our thesis by demonstrating a novel method of accurately estimating multiple non linear forces acting on a system. The methodology started with a data driven PCA with an augmented state space. This yielded an approximate linear model. The result of the PCA was used to build a reduced order estimator to create a data driven augmented state model. Stability and convergence was established and validated in latent variable space, and we showed this translates to the original space. Further, metrics for understanding the robustness and global convergence of the data model was established.

At each step, this powerful new approach was validated using a simulation of our micro UUV. Simulation has the ever present advantage over real data that the "true" results are known precisely, and we can quickly change model parameters for more extensive testing: varying drag models, ground force functions, and so on – only a subset of which have been presented here.

Our testing on simulated data should not be taken as a limitation of the method. The

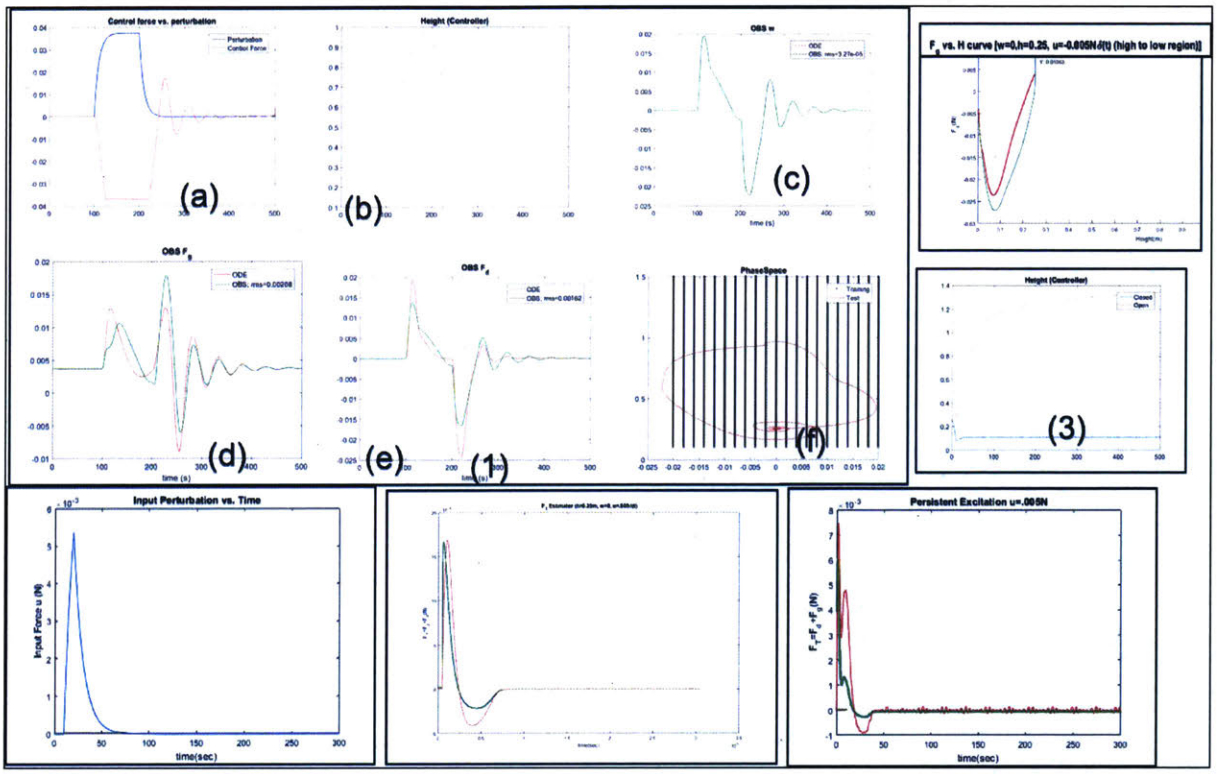

Figure 8-14: Initial h=0.25m, w=0m/sec (a) Control Force(red) and External Perturbation (blue) (b) Height (c) Velocity (d) Fg est (green) (e) Fd estimation (green) (f) Phase Space region (robust) (2) Total Force Estimation for the input to the right. (3) Corresponding height and Fg vs. h curve ? (height with open and closed loop.) (4) Total Force with persistent excitation. If you use a linear estimator, add another second disturbance estimator.

data driven PCA approach is designed for, and ideally suited to, real-world issues as combining data from a large number of sensors. The PCA naturally sorts and condenses this information. We look broadening the application of this method to more complex non linear dynamical systems where understanding of poorly modeled individual non linearities is a subject of interest.

Chapter 9

Conclusion

This doctoral thesis presented tools for design and development of a novel micro UUV for submerged infrastructures. It encompasses three rigorous contributions: (1) design; (2) utilization of fundamental science in robotic application; and (3) development of new mathematical approach which are the foundations for the development of a fully functional underwater robotic system.

The novelty in the design is the introduction of a flattened bottom on an otherwise fully ellipsoidal shape. To the classic free stream behavior we added forces arising from motion in contact with a surface: normal force and friction. We adapted the robot design to be controllable in the presense of these highly non linear forces.

The flat bottom, initially introduced for improved contact with a target surface, also has unusual hydrodynamics. Motion along the surface results in a fluid bed between the robot and the surface, and low friction – lubricated – motion. An additional jet on the bottom surface to explicitly control this fluid layer allows precise control of the gap between the robot and the target surface. Utilization of near surface hydrodynamics is entirely new for UUVs. We investigated via experiment and simulation how passive and actively induced

hydrodynamic ground effect gives rise to a stable equilibrium; and we demonstrated how this phenomenon can be exploited for smooth scanning of rough surfaces.

Finally, to deal with the complexity of forces arising from on contact or near contact motion, a powerful new modeling method was proposed. The method is data driven and requires little or no *a priori* analytic understanding of the system. It is well suited for a wide range of complex dynamical systems, including the UUV which is the focus of the thesis. The result is a linearized model in a higher dimensional space where non linearities are represented as auxiliary variables. An observer is used for estimation of these state dependent auxiliary variables. The method is ideally suited for processing the output from a large numbers of sensors and the correspondingly large data volume. This contribution is extremely important in the current age where with low cost sensors and computing permits high fidelity modeling of complex or poorly understood systems. We show even in the absence of accurate modeling, large amount of data and embedded correlations can be utilized to establish dynamics between various states of the system and estimate unknown variables which have no direct measurements.

9.1 Impact

Robot

With the growth of sub sea technologies and other water based industries, small low cost underwater UUVs will play a significant and expanding role in inspection and monitoring, whether for security, maintenance, or exploration. The work in this doctoral thesis lays the fundamental building blocks towards a future where these underwater drones play a role similar to UAVs (aerial drones) do today.

Monitoring crowded sea ports with large and small ships would require methods that

do not interfere with vehicle traffic. Large UUVs or tethered ROVs are not practical options, whereas low cost micro UUVs as describes here can operate in large number to scan ship hulls and monitor the port area. Hull surfaces are not smooth; but utilizing the hydrodynamic ground effect investigated in this research, fast smooth scanning would be possible.

Appendage free robots such as described here are essential to fast and efficient inspection in a cluttered environment, of which BWR inspection is a classic case. There are similar needs are in other enclosed facilities, water pipelines and such.

For sea bed mapping missions, taking advantage of upwash from impinging jets – as described in this thesis – can result in reduced thrust and enable longer mission times.

We note the hydrodynamic ground effect is really not limited to application underwater. The underlying features can be exploited in any fluid where such relative motion of surfaces is involved. The methods applied here for fluid bed development and gap control could be generalized further. Such application range from precision positioning in biological system to hydraulic systems and oil pipelines.

Modeling

From the perspective of quantitative modeling we live in the age of "big data": cheap sensors which can be used in large numbers; fast, high density computing capable of generating high fidelity simulation, and of processing these large volumes of data. What is lacking is human resources to develop in depth, analytic understanding. What is needed is algorithms to model of complex systems without human intervention.

The method outlined here for unknown variable estimation is a novel and extremely powerful approach to deducing a simple linear model with convergence in estimation guaranteed over the entire operational non linear region. We demonstrated how complex

non linear systems can be recast as high dimensional linear models. Establishing dynamical relationships between state variables, and using appropriate state estimators, one can estimate the unknown and unmeasured state dependent variables.

Though statistical estimation methods such as PCA are widely being exploited in different fields, in control theory using analytical models and performing traditional linearization approach has so far been the norm. We demonstrate a new way of representing the state space model and define an estimator analogous to a traditional state observer for estimation of unknown non linearities. We also investigate and try to analyze concepts of stability and goodness metrics for models derived using system data where traditional concepts of observability and controllability might not be very ideal fit. Convergence, robustness and error analysis are shown along with how uncertainties occur in s

9.2 Future Work

The work presented here does separately studied passive (from lateral motion) and active (from jet) ground effect; in reality, of course, both would occur simultaneously. The two phenomenon need to be merged into a single model.

Turbulence modeling in our simulation is rudimentary. In particular, upwash stability needs to be studied. A more extensive research effort is required to make this aspect realistic.

There are multiple ways of generating the data driven matrix, each with advantages and disadvantages. Means of selection an optimal training window and sample needs to be defined. Other means of including non linearities – such as varying (state dependent) matrices should also be explored.

The robot design is, of course, a research prototype. Its geometry, in particular size, for various potential missions and corresponding payloads needs to be explored.

Appendix A: Nomenclature

Variables	Description	Units
X, Y, Z	Inertial Frame (World)	m
x, y, z	body centric reference frame	m
u, v, w	surge, sway, heave, i.e. body centric x, y, z velocities	m/s
ϕ, θ, ψ	Euler angles (World) - roll, pitch and yaw angle.	radians
p, q, r	body centric roll, pitch and yaw rate	radians/s
α	angles of jets F3, F4 from the z axis	radians
β	angles of jets F1, F2, F5, F6 in the xy plane	radians
γ	angles of jets F1, F2, F5, F6 projected to the xy plane	radians
m	Mass of the vehicle	kg
S_z	Reduced mass	kg
I_{xx}, I_{yy}, I_{zz}	Centroidal moment of inertia about x, y, z	kg m^2
$-X_{\dot{u}}, -Y_{\dot{v}}, -Z_{\dot{w}}$	Added mass in x, y, z	kg
$-K_{\dot{p}}$	Added inertia associated with rotation about x axis	kg
$-M_{\dot{q}}$	Added inertia associated with rotation about y axis	kg
$-N_{\dot{r}}$	Added inertia associated with rotation about z axis	kg
$-X_{uu}, -Y_{vv}, -Z_{ww}$	Drag coefficient associated with u (surge), v (sway), and w (heave)	

$-K_{pp}, -M_{qq}, -N_{rr}$	Drag moment associated with p (rotation about x), q (rotation around y), and r (rotation around z)	
C_{mm}	Munk moment in the xy plane	
C_L	Lift coefficient	
U_c	Free Stream velocity	m/s
F_x, F_y, F_z	Net jet forces in the x, y, z	N
F_T	Thurst force (Ch. 5), total force (Ch. 6)	N
M_x, M_y, M_z	Net moment (torque)in x, y, z	J
F_d	Drag Force	N
F_g	Force due to Hydrodynamic Ground Effect	N
μ_k	Coefficient of dynamic friction	none
N	Normal reaction force (when in contact)	N
F_b	Buoyant Force	N
g	acceleration due to gravity	m/s^2
F_j	Jet Force	N
μ_k	Coefficient of static friction	
N	Normal force	N
h	gap between vehicle and ground	m

Variables specific to Estimation and Control.

$\alpha, \beta\, \gamma$	fit parameters
$\phi(h, w)$	Region of operation (phase space)in h, w
x	State variables
z	Latent Variables
ζ	Auxiliary variables
$\tilde{x}$	Augmented variables (x and ζ combined)

u	Control variable
X	Array of $\tilde{x}$
C	Covariance of $\tilde{x}$
M	Modal matrix, eigenvalues of C
T	Truncated M
U, V, W	subsets of AT corresponding to control, state, and auxiliary variables
A, B	state transition matrices
S	Combined A and B
$A_{()}, J_{()}$	A matrixs, divided into segments corresponding to available (state) and unavailable (latent) variables
z	$\tilde{x}$ transformed to latent variable space
$e_{()}$	Estimation error
u_j	Control variable for a specific jet
	sometimes taken as equivalent to exit velocity
u_{ext}	External perturbation
L	Estimator gain

Bibliography

[1] Maeda, H. "The past, present and future of the ocean engineering activities." Maritime Technology and Engineering (2014): 3.

[2] Rizzo, P. "NDE/SHM of underwater structures: a review." Advances in Science and Technology. Vol. 83. Trans Tech Publications, 2013.

[3] J.A. Ramirez, R. Vasquez, L. Gutierrez, D. Florez, Mechanical/Naval Design of an Underwater Remotely Operated Vehicle (ROV) for Surveillance and Inspection of Port Facilities, Proc. of the 2007 ASME International Mechanical Engineering Congress and Exposition, 2007.

[4] Mcleod, Daniel, John R. Jacobson, and Sekhar Tangirala. "Autonomous inspection of subsea facilities-Gulf of Mexico trials." offshore technology conference. Offshore Technology Conference, 2012.

[5] F. Dirauf, B. Gohlke, and E. Fischer, Innovative Robotics and Ultrasonic Technology at the Examination of Reactor Pressure Vessels in BWR and PWR Nuclear Reactor Power Stations, Insight-Non-Destructive Testing and Condition Monitoring, vol. 42(9), 2000, pp. 590-593

[6] K. Kussmaul, D. Blind, J. Jansky, R. Rintamaa, Formation and growth of cracking in feed water pipes and RPV nozzles, Nuclear Engineering and Design, Volume 81, Issue 1, 2 August 1984, Pages 105-119, ISSN 0029-5493

[7] Vaganay, J.; Elkins, M.; Esposito, D.; O'Halloran, W.; Hover, F.; Kokko, M., "Ship Hull Inspection with the HAUV: US Navy and NATO Demonstrations Results," OCEANS 2006 , vol., no., pp.1,6, 18-21 Sept. 2006

[8] Truver, Scott C. "Mines and underwater IEDs in US ports and waterways." Naval War College Review 61.1 (2008): 106.

[9] Andrew Martin, Underwater Smugglers Watching Ship Come In, Sun Sentinel, May 29, 1990.

[10] J-K. Choi, H. Sakai, T. Tanaka, Autonomous Towed Vehicle for Underwater Inspection in a Port Area, Proc. of the 2005 IEEE International Conference on Robotics and Automation, 2005, 188-193.

[11] Evans, William Eugene. "A Short History of the Navy's Marine Mammal Program." Aquatic Mammals 34.3 (2008): 368.

[12] Schmitz, Volker , Nondestructive Acoustic Imaging Techniques, Imaging of Complex Media with Acoustic and Seismic Waves Topics in Applied Physics Volume 84, 2002, pp 167-190

[13] J.Bruce Nestleroth, Richard J. Davis, Application of eddy currents induced by permanent magnets for pipeline inspection, NDT International, vol, pp 40, 1, 77-84, January 2007, ISSN 0963-8695.

[14] Aindow, A. M., et al. "Laser-based non-destructive testing techniques for the ultrasonic characterization of subsurface flaws." NDT international 17.6 (1984): 329-335.

[15] A. Mazumdar, M. Lozano, A. Fittery and H.H Asada, A compact, maneuverable, underwater robot for direct inspection of nuclear power piping systems, Robotics and Automation (ICRA), 2012 IEEE International Conference on , vol., no., pp.2818,2823, 14-18 May 2012

[16] Zhu, Jie. Optimization of matching layer design for medical ultrasonic transducer. ProQuest, 2008.

[17] H Wong; Chieh and Umehara, Noritsugu and Kato, Koji, "Frictional characteristics of ceramics under water-lubricated conditions",Tribology Letters,November 1998, ISBN:1023-8883

[18] Bhattacharyya, S., H. Harry Asada, and Michael S. Triantafyllou. "A self stabilizing underwater sub-surface inspection robot using hydrodynamic ground effect." Robotics and Automation (ICRA), 2015 IEEE International Conference on. IEEE, 2015.

[19] Robots in the nuclear industry: a review of technologies and applications, Industrial Robot: An International Journal, vol.,no., pp., 38, 2, 113-118, 2011

[20] K. Koji, Underwater inspection robot -AIRIS 21, Nuclear Engineer- ing and Design, Vol., 188, 1999, 367-371.

[21] Ross, Bill, John Bares, and Chris Fromme. "A semi-autonomous robot for stripping paint from large vessels." The international journal of robotics research 22.7-8 (2003): 617-626.

[22] Menegaldo, Luciano Luporini, et al. "Development and navigation of a mobile robot for floating production storage and offloading ship hull inspection." Industrial Electronics, IEEE Transactions on 56.9 (2009): 3717-3722.

[23] Katz, Joseph. "Aerodynamics of race cars." Annu. Rev. Fluid Mech. 38 (2006): 27-63.

[24] Blevins, Erin, and George V. Lauder. "Swimming near the substrate: a simple robotic model of stingray locomotion." Bioinspiration & biomimetics 8.1 (2013): 016005.

[25] Bryan N. Nowroozi, James A. Strother, Jaquan M. Horton, Adam P. Summers, Elizabeth L. Brainerd, Whole-body lift and ground effect during pectoral fin locomotion in the northern spearnose poacher (Agonopsis vulsa), Zoology, Volume 112, Issue 5, September 2009, Pages 393-402, Pages: 303-308, ISSN 0944-2006

[26] Quinn, Daniel B., George V. Lauder, and Alexander J. Smits. "Flexible propulsors in ground effect." Bioinspiration & biomimetics 9.3 (2014): 036008.

[27] S. Bhattacharyya, H.H. Asada, Compact, Tetherless ROV for In-Contact Inspection of Underwater Structures , IEEE/RSJ International Conference on Intelligent Robotics and Systems, September 2014

[28] Jolliffe, Ian. Principal component analysis. John Wiley & Sons, Ltd, 2002.

[29] Triantafyllou, Michael S., and Franz S. Hover. "Maneuvering and control of marine vehicles." Cambridge, Massachusetts, USA: edited by authors (2003).

[30] K. Asakawa, J. Kojima, Y. Ito, S. Takagi, Y. Shirasaki, N. Kato, Autonomous Underwater Vehicle AQUA EXPLORER 1000 for Inspection of Underwater Cables, Proc. of the 1996 IEEE Symposium on Autonomous Underwater Vehicle Technology, 1996, pp 10-17.

[31] Yuh, Junku. "Design and control of autonomous underwater robots: A survey." Autonomous Robots 8.1 (2000): 7-24.

[32] I. Komuraa, T. Hirasawaa, S. Nagaia, J. Takabayashib, K. Narusec, Crack detection and sizing technique by ultrasonic and electromagnetic methods, Nuclear Engineering and Design, vol. 206, issues 2-3, Jun 2001, p351-362

[33] Antonelli, Gianluca, et al. "Adaptive control of an autonomous underwater vehicle: experimental results on ODIN." IEEE Transactions on Control Systems Technology 9.5 (2001): 756-765.

[34] Licht, Stephen, et al. "Design and projected performance of a flapping foil AUV." IEEE Journal of Oceanic Engineering 29.3 (2004): 786-794.

[35] Fallon, J. Barry, et al. "URSULA: Design of an underwater robot for nuclear reactor vessel inspection." Robotics for Challenging Environments. 1994.

[36] Mazumdar, H.H. Asada, A Compact Underwater Vehicle Using High Bandwidth Coanda-Effect Valves for Low Speed Precision Maneuvering in Cluttered Environments, Proc. of the IEEE International Conference on Robotics and Automation, 2011, pp 1544-1550.

[37] Crump, S. Scott. "Apparatus and method for creating three-dimensional objects." U.S. Patent No. 5,121,329. 9 Jun. 1992.

[38] Rust, Ian C., and H. Harry Asada. "The eyeball ROV: Design and control of a spherical underwater vehicle steered by an internal eccentric mass." Robotics and Automation (ICRA), 2011 IEEE International Conference on. IEEE, 2011.

[39] Mazumdar, Anirban, and H. Harry Asada. "Control-configured design of spheroidal, appendage-free, underwater vehicles." IEEE Transactions on Robotics 30.2 (2014): 448-460.

[40] Lozano Jr, Martin. Optical proximity sensor and orientation control of autonomous, underwater robot. Diss. Massachusetts Institute of Technology, 2014.

[41] Bright, Lawrence Lawrence Zack. A sub-millimeter precision distance and orientation sensor for close-proximity in air and water. Diss. Massachusetts Institute of Technology, 2015.

[42] Bhattacharyya, Sampriti, Haruhiko Harry Asada, and Michael S. Triantafyllou. "Underwater vehicle design and control methods." U.S. Patent Application No. 15/060,575.

[43] Wu, Sheng-Ju, Cheng-Hsing Hsu, and Tsung-Te Lin. "Model test of the surface and submerged vehicles with the micro-bubble drag reduction." Ocean engineering 34.1 (2007): 83-93.

[44] Lewis, Edward V. "Principles of naval architecture second revision." Jersey: SNAME (1988).

[45] Swevers, Jan, et al. "An integrated friction model structure with improved presliding behavior for accurate friction compensation." IEEE Transactions on automatic control 45.4 (2000): 675-686.

[46] A.Mazumdar,A.Fittery,M.Lozano,H.Asada,ActiveYawStabilization for Smooth Highly Maneuverable Underwater Vehicles, Proceed- ings of the 2012 ASME Dynamic Systems and Controls Conference.

[47] Thornton, Brian H., and David B. Bogy. "Head-disk interface dynamic instability due to intermolecular forces." Magnetics, IEEE Transactions on 39.5 (2003): 2420-2422.

[48] Vineet Gupta, and David B. Bogy. "Dynamics of sub-5-nm air-bearing sliders in the presence of electrostatic and intermolecular forces at the head-disk interface." Magnetics, IEEE Transactions on 41.2 (2005): 610-615.

[49] Zhang, Xin, Willem Toet, and Jonathan Zerihan. "Ground effect aerodynamics of race cars." Applied Mechanics Reviews 59.1 (2006): 33-49.

[50] Rozhdestvensky, Kirill V. "Wing-in-ground effect vehicles." Progress in Aerospace Sciences 42.3 (2006): 211-283.

[51] Savage, S. B. "Laminar radial flow between parallel plates." Journal of Applied Mechanics 31.4 (1964): 594-596.

[52] Incropera, Frank P., et al. Fundamentals of heat and mass transfer. Wiley, 2007.

[53] JPinkus, Oscar, and Beno Sternlicht. "Theory of hydrodynamic lubrication." McGraw-Hill, 1961.

[54] Manual, ANSYS User?S. "Ansys." Inc. Modeling, CFX 11 (2000).

[55] Jenkins, Mark, and Steven Floyd. "Trajectories in the evolution of technology: A multi-level study of competition in Formula 1 racing." Organization Studies 22.6 (2001): 945-969.

[56] Cherukat, P., and J. B. McLaughlin. "Wall-induced lift on a sphere." International Journal of Multiphase Flow 16.5 (1990): 899-907.

[57] Cherukat, Pradeep, and John B. Mclaughlin. "The inertial lift on a rigid sphere in a linear shear flow field near a flat wall." Journal of Fluid Mechanics 263 (1994): 1-18.

[58] Cooper, Kevin R., J. Syms, and G. Sovran. Selecting automotive diffusers to maximise underbody downforce. No. 2000-01-0354. SAE Technical Paper, 2000.

[59] S Bhattacharyya, HH Asada, M Triantafyllou, Design Analysis of a Self Stabilizing Underwater Sub-Surface Inspection Robot Using Hydrodynamic Ground Effect, presented in OCEANS, May 2015.

[60] Bhattacharyya, S., H. H. Asada, and M. S. Triantafyllou. "A self stabilizing underwater sub-surface inspection robot using hydrodynamic ground effect." Robotics and Automation (ICRA), 2015 IEEE International Conference on. IEEE, 2015

[61] Advanced Aircraft Flight Performance, Antonio Filippone, December 2012FORMAT: HardbackI SBN: 9781107024007

[62] Anjaneyulu Krothapalli, Charles A. Smith "Recent Advances in Aerodynamics: Proceedings of an International Symposium held at Stanford University", August 22-26", 1983

[63] Daniel B. Levin and Douglas A. Wardwell, Single Jet-Induced Effects on Small-Scale Hover Data in Ground Effect

[64] Hange, C. R. A. I. G. E., R. E. Kuhn, and V. R. Stewart. Jet-Induced Ground Effects on a Parametric Flat-Plate Model in Hover. National Aeronautics and Space Administration, Ames Research Center, 1993.

[65] Kotansky, D. R., and W. W. Bower. "A basic study of the VTOL ground effect problem for planar flow." Journal of Aircraft 15.4 (1978): 214-221..

[66] Hilbert, Martin, and Priscila López. "The world?s technological capacity to store, communicate, and compute information." science 332.6025 (2011): 60-65.

[67] Karnopp, Dean C., Donald L. Margolis, and Ronald C. Rosenberg. System dynamics: modeling, simulation, and control of mechatronic systems. John Wiley & Sons, 2012.

[68] Asada, H. Harry, et al. "A data-driven approach to precise linearization of nonlinear dynamical systems in augmented latent space." American Control Conference (ACC), 2016. American Automatic Control Council (AACC), 2016.

[69] Wu, Faye Y., and H. Harry Asada. "Implicit and Intuitive Grasp Posture Control for Wearable Robotic Fingers: A Data-Driven Method Using Partial Least Squares." IEEE Transactions on Robotics 32.1 (2016): 176-186.

[70] Bhattacharyya, S., H. H. Asada, "Precise Linearization of Nonlinear, Non-Autonomous Systems Based on Physical System Modeling Theory", American Control Conference (ACC), 2017. American Automatic Control Council (AACC), 2017.

[71] Van Overschee, Peter, and Bart De Moor. "N4SID: Subspace algorithms for the identification of combined deterministic-stochastic systems." Automatica 30.1 (1994): 75-93.

[72] Van Overschee, Peter, and Bart De Moor. "N4SID: Subspace algorithms for the identification of combined deterministic-stochastic systems." Automatica 30.1 (1994): 75-93.

[73] Lee, Jay H., and N. Lawrence Ricker. "Extended Kalman filter based nonlinear model predictive control." American Control Conference, 1993. IEEE, 1993.

[74] Patton, R. J., and J. Chen. "Observer-based fault detection and isolation: Robustness and applications." Control Engineering Practice 5.5 (1997): 671-682.

[75] Ioannou, Petros A., and Jing Sun. Robust adaptive control. Courier Corporation, 2012.

[76] Luenberger, D. "Observers for multivariable systems." IEEE Transactions on Automatic Control 11.2 (1966): 190-197.

[77] Yedavalli, Rama K. Robust control of uncertain dynamic systems: a linear state space approach. Springer Science & Business Media, 2013.

[78] Patel, R. V., and M. Toda. "Quantitative measures of robustness for multivariable systems." Joint Automatic Control Conference. No. 17. 1980.

[79] Yedavalli, R. K. "Perturbation bounds for robust stability in linear state space models." International Journal of Control 42.6 (1985): 1507-1517.